

STUDY ON $\text{Na}_{2x}[\text{Ni}_x\text{Ti}_{1-x}]\text{O}_2$ AS BI-FUNCTIONAL ELECTRODE MATERIAL FOR
SODIUM-ION BATTERIES

By

Qian Chen

A DISSERTATION

Submitted to
Michigan State University
in partial fulfillment of the requirements
for the degree of

Chemical Engineering—Doctor of Philosophy

2021

ABSTRACT

STUDY ON $\text{Na}_{2x}[\text{Ni}_x\text{Ti}_{1-x}]\text{O}_2$ AS BI-FUNCTIONAL ELECTRODE MATERIAL FOR SODIUM-ION BATTERIES

By

Qian Chen

The rapid development of renewable energy resources in response to growing concerns about fossil fuels dependence and greenhouse gas emissions has raised challenges to developing large-scale energy storage systems for the smooth integration of intermittent energy resources into the grid. Increasing research efforts have been devoted to the study of the sodium-ion battery technology as a promising solution to these challenges, especially in the search for better electrode materials. In this thesis, we focused on the investigation of $\text{Na}_{2x}[\text{Ni}_x\text{Ti}_{1-x}]\text{O}_2$, a promising bi-functional electrode material that can be used as either positive or negative electrode material in sodium-ion batteries. This thesis aims to gain fundamental understandings of this material using a combination of experimental and computational techniques and to provide insights into the exploration and design of electrode materials for sodium-ion batteries.

Firstly, the average and local structural properties and energetics of atomic distribution in $\text{P2-Na}_{2/3}[\text{Ni}_{1/3}\text{Ti}_{2/3}]\text{O}_2$ were investigated using Rietveld refinement on neutron diffraction datasets and atomistic simulations based on the Buckingham and Morse interatomic potential models. Both computational and experimental results showed similar nuclear density maps and higher occupancies of Na at edge-sharing sites than face-share sites. The simulations based on both potential models suggested that it is energetically favorable to have an equal amount of Na and transition metal in each of the two layers.

The atomic and electronic structure changes during cycling were studied based on density functional theory (DFT) calculations. DFT-based molecular dynamics (MD) simulations showed

an expansion of ab plane and contraction of c axis upon Na insertion and a small change of lattice parameters upon Na extraction. DFT calculations revealed that Ni and Ti play a dominant role in the redox reactions upon Na extraction and insertion respectively, along with the participation of O. A higher in-plane electronic conductivity was observed compared to the through-plane one, with both increasing when Na ions were inserted or extracted.

The quasi-elastic neutron scattering (QENS) experiments showed that Na ion diffusion can be well described by the Singwi-Sjölander jump diffusion model, where the obtained mean jump length matched the distances between the neighboring edge-share and face-share Na sites. The MD simulations based on DFT calculations showed a better consistency with experimental results than MD based on interatomic potential (IP) models in terms of diffusivity and activation energy. Faster diffusion was observed for compositions with less sodium, i.e., more vacancies. Both Na-deficient phase $\text{Na}_{5/9}[\text{Ni}_{1/3}\text{Ti}_{2/3}]\text{O}_2$ and Na-rich phase $\text{Na}_{7/9}[\text{Ni}_{1/3}\text{Ti}_{2/3}]\text{O}_2$ showed higher ionic conductivity compared to the pristine phase.

Finally, the diffusion and ionic conduction for P2 and O3 $\text{Na}_{2x}[\text{Ni}_x\text{Ti}_{1-x}]\text{O}_2$ are calculated with machine learning based interatomic potential models. Higher diffusivity and ionic conductivity were observed for the P2 structure.

ACKNOWLEDGEMENTS

First of all, I would like to express my sincere gratitude to my adviser, Dr. Wei Lai, for his support and guidance during my Ph.D. study. He has set the best role model for me for a wonderful mentor and researcher: always kind and patient, incredibly knowledgeable yet still enthusiastic about learning new things, open to new ideas while maintaining a critical perspective, passionate and devoted to research work. I am grateful for the opportunity to work with him and I could not have imagined having a better PhD advisor. I'd like to extend my thanks to other members of my thesis committee, Dr. Scott Calabrese Barton, Dr. Jose Mendoza, and Dr. Pengpeng Zhang for their guidance and advice on this thesis.

I'd like to thank my former and current fellow labmates that I have worked with: Dr. Matt Klenk, Dr. Junchao Li, Jin Dai, Yue Jiang, and Yining He. It was a great pleasure working with them. Being the only chemical engineer in the group, every time I turned to them for insights from material scientists' perspectives, they were always willing to share helpful and valuable ideas in our discussions. I have learned so much from each of them in many ways. Especially Jin, we began our Ph.D. studies and joined the group at the same time and have spent most of our time together in the office. Your friendship and support are priceless.

I'd like to thank my parents for their unconditional love throughout these years and for always supporting every decision I've made. Thank you to my friends who made my life in a foreign country far away from my family fun and colorful. Last but not least, I'd like to thank my incredible husband Xiao for always being there for me and having faith in me through the hard times. I couldn't have made it through the difficulties of my PhD journey without his encouragement and support.

TABLE OF CONTENTS

| | |
|---|------|
| LIST OF TABLES | vii |
| LIST OF FIGURES | viii |
| CHAPTER 1 Introduction | 1 |
| 1.1 Background | 1 |
| 1.2 Sodium-ion batteries vs. lithium-ion batteries | 2 |
| 1.2.1 Sodium vs. lithium | 2 |
| 1.2.2 The working principle of sodium-ion batteries | 5 |
| 1.3 Electrode materials for sodium-ion batteries | 6 |
| 1.3.1 Positive electrode materials | 8 |
| 1.3.2 Negative electrode materials | 14 |
| 1.3.3 Bi-functional electrode materials | 16 |
| 1.4 The $\text{Na}_{2x}[\text{Ni}_x\text{Ti}_{1-x}]\text{O}_2$ group | 16 |
| 1.5 Thesis overview | 18 |
| CHAPTER 2 Methods | 20 |
| 2.1 Computational methods | 20 |
| 2.1.1 Density functional theory | 20 |
| 2.1.2 Interatomic potential model | 22 |
| 2.1.3 Molecular dynamics simulation | 27 |
| 2.2 Experimental methods | 28 |
| 2.2.1 Sample preparation | 28 |
| 2.2.2 Neutron diffraction and Rietveld refinement | 29 |
| 2.2.3 Quasi-elastic neutron scattering | 30 |
| CHAPTER 3 Structural properties of $\text{P2-Na}_{2/3}[\text{Ni}_{1/3}\text{Ti}_{2/3}]\text{O}_2$ | 33 |
| 3.1 Introduction | 33 |
| 3.2 Average structural information from Rietveld refinement | 33 |
| 3.3 Energy minimization based on two interatomic potential models | 40 |
| 3.4 Energetics of Atomic Distribution and Ordering | 43 |
| 3.5 Simulated Average Structure | 45 |
| 3.6 Conclusions | 47 |
| CHAPTER 4 Structural and electronic properties change during cycling | 49 |
| 4.1 Introduction | 49 |
| 4.2 DFT calculations | 49 |
| 4.3 Structural changes upon Na extraction/insertion | 50 |
| 4.4 Electron density distribution and the atomic charge | 54 |
| 4.5 Density of states | 56 |
| 4.6 Electronic conductivity | 58 |
| 4.6.1 Electronic conductivity from the Kubo-Greenwood approach | 58 |
| 4.6.2 Electronic conductivity from the Boltzmann transport equations | 59 |
| 4.7 Conclusions | 62 |

| | | |
|--------------|--|-----|
| CHAPTER 5 | Dynamic properties of P2-Na _{2/3} [Ni _{1/3} Ti _{2/3}]O ₂ | 64 |
| 5.1 | Introduction..... | 64 |
| 5.2 | Self-diffusion of Na ions from QENS | 64 |
| 5.3 | Ionic conductivity and Na self-diffusion from IP-based MD | 68 |
| 5.3.1 | Construction of the polarizable interatomic potential..... | 68 |
| 5.3.2 | IP-based MD simulations..... | 70 |
| 5.3.3 | Extraction of diffusivity and ionic conductivity from IP-based MD..... | 73 |
| 5.4 | First principles MD simulations..... | 79 |
| 5.5 | Conclusions..... | 85 |
| CHAPTER 6 | Study on P2/O3 Na _{2x} [Ni _x Ti _{1-x}]O ₂ with machine learning based interatomic potential models..... | 87 |
| 6.1 | Introduction..... | 87 |
| 6.2 | Construction of the neural network potential..... | 88 |
| 6.3 | Testing the NN potential..... | 91 |
| 6.4 | MD simulations with the NN potential..... | 93 |
| 6.4.1 | Calculation of lattice parameters | 94 |
| 6.4.2 | Diffusion and ionic conduction..... | 96 |
| 6.5 | Conclusions..... | 98 |
| CHAPTER 7 | Conclusions and future work | 100 |
| 7.1 | Conclusions..... | 100 |
| 7.2 | Future work..... | 103 |
| BIBLIOGRAPHY | | 106 |

LIST OF TABLES

| | |
|---|----|
| Table 1: The Comparison between sodium and lithium | 3 |
| Table 2: Structural information of $\text{Na}_{2/3}[\text{Ni}_{1/3}\text{Ti}_{2/3}]\text{O}_2$ using Rietveld refinement of neutron diffraction datasets. | 35 |
| Table 3: Interatomic potential parameters of the Buckingham model and Morse model..... | 42 |
| Table 4: Potential transferability across selected materials containing Na, Ni, Ti, and O. (The mean absolute errors of the Buckingham and Morse potentials are 1.4 and 2.8%, respectively). 43 | |
| Table 5: Polarizable interatomic potential parameters..... | 69 |
| Table 6: Structures used in the training and validation set | 88 |
| Table 7: Parameters of symmetry functions for all atoms | 89 |

LIST OF FIGURES

| | |
|---|----|
| Figure 1: The schematic of a sodium-ion battery | 6 |
| Figure 2: Schematics of (a)P2 and (b)O3 structure for Na_xTMO_2 | 9 |
| Figure 3: Schematics of structures of (a) olivine-type NaFePO_4 , (b) $\text{Na}_3\text{V}_2(\text{PO}_4)_3$ and (c) $\text{Na}_2\text{FePO}_4\text{F}$ | 11 |
| Figure 4: Schematics of the NaFeF_3 structure | 13 |
| Figure 5: Structure of $\text{Na}_x\text{M1}[\text{M2}(\text{CN})_6]_y$ | 14 |
| Figure 6: The distribution of Na ions in edge-sharing and face-sharing sites in P2- $\text{Na}_{2x}[\text{Ni}_x\text{Ti}_{1-x}]\text{O}_2$ viewed (a) along the ab plane (b) along the c axis..... | 17 |
| Figure 7: The schematics of non-polarizable fixed charge model and polarization models including fluctuating charge model, core-shell model and induced dipole model ¹⁴² | 24 |
| Figure 8: The schematic of a neural network architecture to construct interatomic potentials. G_i are the atomic descriptors. E_{at} is the atomic energy. y_{ij} is the output value at node i in layer j . $ak, ij - 1, j$ is the weights connecting node k in layer $j-1$ to the node i in the layer j . b_{ij} is the bias for node i in layer j | 27 |
| Figure 9: Rietveld refinement of $\text{Na}_{2/3}[\text{Ni}_{1/3}\text{Ti}_{2/3}]\text{O}_2$ powders characterized at 15K using detector bank 1 (a) and bank 4 (b), at 300K using bank 1 (c) and bank 4 (d). | 34 |
| Figure 10: 3D nuclear density maps and 2D slices on the $\{001\}$ plane of Na. 3D isosurface level is 0.5 \AA^{-3} while 2D isosurface level is between 0 and 1 \AA^{-3} . Results from the Rietveld refinement at 15 K, Buckingham potential, and Morse potential are shown for each column. | 37 |
| Figure 11: 3D nuclear density maps and 2D slices on the $\{001\}$ plane of Ni. 3D isosurface level is 0.5 \AA^{-3} while 2D isosurface level is between 0 and 1 \AA^{-3} . Results from the Rietveld refinement at 15 K, Buckingham potential, and Morse potential are shown for each column. | 38 |
| Figure 12: 3D nuclear density maps and 2D slices on the $\{001\}$ plane of Ti. 3D isosurface level is 0.5 \AA^{-3} while 2D isosurface level is between 0 and 1 \AA^{-3} . Results from the Rietveld refinement at 15 K, Buckingham potential, and Morse potential are shown for each column. | 39 |
| Figure 13: 3D nuclear density maps and 2D slices on the $\{001\}$ plane of O. 3D isosurface level is 0.5 \AA^{-3} while 2D isosurface level is between 0 and 1 \AA^{-3} . Results from the Rietveld refinement at 15 K, Buckingham potential, and Morse potential are shown for each column. | 40 |
| Figure 14: Energy distribution curve from the Buckingham and Morse potential for $3 \times 2 \times 1$ supercells with four different scenarios of atom distribution: Na equal and Ni equal, Na random and Ni equal, Na equal and Ni random, and Na random and Ni random. | 45 |

| | |
|--|----|
| Figure 15: Example structures of (a) P2 and (b, c) O2 stacking for the supercell used in the atomistic simulation..... | 47 |
| Figure 16: Calculated lattice parameters of P2-Na _x [Ni _{1/3} Ti _{2/3}]O ₂ vs. sodium content x (black squares), compared to an XRD study by Fielden et al. ¹⁸² | 51 |
| Figure 17: (a) The distribution of Ni-O bond lengths (b) an example of a JT-inactive Ni ion (c) an example of a JT-active Ni ion..... | 53 |
| Figure 18: Electron density difference (positive in yellow and negative in cyan) upon (a) Na insertion, (b) Na extraction. The isosurface level is 0.005 Å ⁻³ . The Na, Ni, Ti and O atoms are represented by yellow, gray, blue and red spheres, respectively. | 55 |
| Figure 19: The atomic charge distribution for each atom at different sodium content x in Na _x [Ni _{1/3} Ti _{2/3}]O ₂ based on (a) DDEC model; (b) Bader model..... | 56 |
| Figure 20: The density of states of Na _x [Ni _{1/3} Ti _{2/3}]O ₂ with (a)x=0.44, (b) x=0.67, (c) x=0.89. The Fermi energy is set to be zero. | 57 |
| Figure 21: The electronic conductivity of Na _x [Ni _{1/3} Ti _{2/3}]O ₂ at different x from the Kubo-Greenwood approach | 59 |
| Figure 22: The electrical conductivity of Na _x [Ni _{1/3} Ti _{2/3}]O ₂ at different x. The left, middle, and right panel represents results for Na _{5/9} [Ni _{1/3} Ti _{2/3}]O ₂ , Na _{2/3} [Ni _{1/3} Ti _{2/3}]O ₂ , Na _{7/9} [Ni _{1/3} Ti _{2/3}]O ₂ , respectively. Yellow, green, and purple points represent the calculated electrical conductivity along x, y, and z direction, respectively. | 61 |
| Figure 23: Experimental QENS spectra S(Q,E) for various temperatures at Q=0.3 Å ⁻¹ | 65 |
| Figure 24: (a) Fit of the QENS spectra at 700 K and Q=0.3 Å ⁻¹ . (b) The HWHM of the Lorentzian function at 700 K as a function of Q ² , fitted to the Fickian model at small Q (red line) and the SS model (black line). | 66 |
| Figure 25: Diffusional properties from QENS at 450 to 700K: (a) The Fickian self-diffusivity of Na. (b) The residence time and (c) jump length of Na diffusion with the SS model. | 68 |
| Figure 26: The comparison of IP forces (blue circles) and DFT forces (black line) on each type of atom..... | 70 |
| Figure 27: Lattice parameters of pristine P2-Na _{2/3} [Ni _{1/3} Ti _{2/3}]O ₂ at different temperatures obtained from neutron diffraction by Shanmugam et al ¹⁷⁸ (red stars), DFT-based MD (blue circles), and IP-based MD (green squares). | 72 |
| Figure 28: The nuclear density map of Na during 500 ps simulation at 1100 K. (a) 3D view with an isosurface level of 0.2 Å ⁻³ , (b) 2D slice on the (001) lattice plane with an isosurface level of 0~0.5 Å ⁻³ . “E” and “F” represent edge-share sites and face-share sites | 73 |

| | |
|---|----|
| Figure 29: (a) The $I(\mathbf{Q},t)$ at 1100 K (b) Γ vs. Q^2 (black circles), with the CE fit (black line) and linear fit for the three smallest Q (red line). | 75 |
| Figure 30: Diffusional properties from MD simulations at 900 to 1200 K: (a) The Fickian self-diffusivity of Na. (b) The residence time and (c) jump length of Na diffusion with the Chudley-Elliott model..... | 76 |
| Figure 31: The real part of coherent charge-current correlation at 1100 K in (a) full frequency span. (b) the low-frequency region. The blue and red curves represent the in-plane and through-plan ionic conduction, respectively. | 78 |
| Figure 32: The calculated in-plane ionic conductivity of $\text{Na}_{2/3}[\text{Ni}_{1/3}\text{Ti}_{2/3}]\text{O}_2$ compared with experimental values from Shanmugam et al. ¹⁰⁴ , Shin et al. ¹⁰³ , Smirnova et al. ²⁰⁰ | 79 |
| Figure 33: The nuclear density map of Na from 20 ps MD simulation trajectory at 1100 K. (a) 3D view with an isosurface level of 0.2 \AA^{-3} , (b) 2D slice on the (001) lattice plane with an isosurface level of $0\sim 0.5 \text{ \AA}^{-3}$ | 80 |
| Figure 34: Calculated Fickian diffusivity from FPMD simulation (red) compared to results from IPMD(green) and QENS(blue). | 81 |
| Figure 35: Calculated Fickian diffusivity from FPMD simulation at 900 K for different sodium content..... | 82 |
| Figure 36: Calculated in-plane ionic conductivity of $\text{Na}_{2/3}\text{Ni}_{1/3}\text{Ti}_{2/3}\text{O}_2$ compared with computational values from Chen et al. ²⁰² and experimental data from Shanmugam et al. ¹⁰⁴ , Shin et al. ¹⁰³ , and Smirnova et al. ²⁰⁰ | 84 |
| Figure 37: The calculated in-plane ionic conductivity from FPMD simulation at 900 K for different sodium content. | 85 |
| Figure 38: The comparison of NN-IP energies (red circles for P2 structures and blue circles for O3 structures) and DFT energies (black line) for the training set. | 91 |
| Figure 39: The comparison of NN-IP forces (blue circles) and DFT energies (black line) for the test set for each type of atom in (a) P2 structures and (b) O3 structures. | 92 |
| Figure 40: Lattice parameters of $\text{P2-Na}_{2/3}[\text{Ni}_{1/3}\text{Ti}_{2/3}]\text{O}_2$ at different temperatures obtained from NN-IP based MD simulations (yellow circles) compared to results from neutron diffraction by Shanmugam et al. ¹⁷⁸ (red stars), DFT-based MD (blue diamonds), and IP-based MD (green squares). | 94 |
| Figure 41: Lattice parameters of $\text{O3-Na}_{0.83}[\text{Ni}_{0.42}\text{Ti}_{0.58}]\text{O}_2$ at different temperatures obtained from NN-IP based MD simulations (yellow circles) compared to results extrapolated from XRD by Fielden et al. ¹⁰⁵ (red stars)..... | 95 |
| Figure 42: Fickian diffusivity of Na in $\text{P2-Na}_{2/3}[\text{Ni}_{1/3}\text{Ti}_{2/3}]\text{O}_2$ and $\text{O3-Na}_{0.83}[\text{Ni}_{0.42}\text{Ti}_{0.58}]\text{O}_2$ calculated from IP-NN based MD simulations (yellow squares for $\text{P2-Na}_{2/3}[\text{Ni}_{1/3}\text{Ti}_{2/3}]\text{O}_2$ and green | |

squares for O3-Na_{0.83}[Ni_{0.42}Ti_{0.58}]O₂) compared to results for P2-Na_{2/3}[Ni_{1/3}Ti_{2/3}]O₂ from FPMD(green squares) and QENS(blue circles)..... 96

Figure 43: Calculated in-plane ionic conductivity of P2-Na_{2/3}[Ni_{1/3}Ti_{2/3}]O₂ (blue squares) and O3-Na_{0.83}[Ni_{0.42}Ti_{0.58}]O₂ (blue circles) from IP-NN based MD simulations compared with results from DFT-MD (black) and experimental data for P2-Na_{2/3}[Ni_{1/3}Ti_{2/3}]O₂ and O3-Na_{0.8}[Ni_{0.4}Ti_{0.6}]O₂ from Shanmugam et al.¹⁰⁴ (red), Shin et al.¹⁰³ (green), and Smirnova et al.²⁰⁰ (yellow). Results for P2 and O3 structures are represented as squares and circles respectively. 98

CHAPTER 1 Introduction

1.1 Background

With increasing concerns about fossil fuels dependence and greenhouse gas emissions, renewable energy technologies have developed rapidly in recent decades, like solar and wind energy. The rapid development of these intermittent renewable sources brought in new challenges to developing large-scale electrical energy storage systems with low cost, as they are essential for the smooth grid integration and peak load management. Among the energy storage technologies suitable for grid-scale applications, electrochemical storage systems, i.e., batteries, provide a promising option to store the extra energy. Compared to other energy storage technologies like pumped hydroelectric storage and compressed air storage, advantages of batteries include flexibility, low environmental impacts, high round-trip efficiency, and low maintenance cost^{1,2}.

Among battery technologies, lithium-ion batteries (LIB) have been dominating the electrochemical energy storage market since the first carbon/LiCoO₂ cell was introduced into the market by Sony in 1991³, due to their overwhelming advantages of high power density, high energy density, and long lifetime. Lithium-ion batteries have been widely used in portable electric devices like cell phones, tablets, and laptops as well as electric vehicles. However, applications of lithium-ion batteries in large-scale stationary energy storage are likely to be limited by the high cost and limited availability of lithium resources⁴. Studies based on the analysis of the geological resources of lithium have predicted that the estimated lithium reserve may be insufficient to meet the massive demand for lithium-ion batteries^{5,6}. Furthermore, the low recovery rate of lithium may result in the problem that the recoverable lithium is unable to satisfy the growing lithium demand⁷. Even if lithium resources are abundant, lithium-ion batteries are not an economically feasible option for the grid-scale energy storage. Considering the insufficient abundance and geographical

concentration of lithium reserves, as well as the relatively high cost, the search for an earth-abundant and affordable alternative material to lithium is essential for grid-scale electrochemical energy storage.

Sodium is also in the series of alkali metal elements in the periodic table as lithium, thus sharing some similar chemical properties with lithium. Consequently, as one of the most earth-abundant elements, sodium has attracted researchers' attention as a potential alternative to lithium for battery applications. Sodium-ion batteries, where sodium ions serve as charge carriers, have been studied as early as the late 1970s⁸⁻¹⁰. However, the research development of sodium-ion batteries decelerated as the research focus has been shifted to lithium-ion batteries since a high energy density was reported for lithium-ion batteries¹¹. Until in recent years, with growing interests in grid-scale electrochemical storage systems, sodium-ion batteries became attractive as a cost-effective alternative to lithium-ion batteries for large-scale stationary energy storage applications, because of the low cost and huge natural abundance of sodium resources^{12,13}. Thus, increasing research efforts have been devoted to the study of sodium-ion batteries¹⁴⁻¹⁷.

1.2 Sodium-ion batteries vs. lithium-ion batteries

1.2.1 Sodium vs. lithium

Table 1 shows the comparison of some properties related to the battery performance between sodium and lithium. As shown in the table, sodium is slightly heavier than lithium with an atomic weight of 23 g/mol compared to the 6.9g/mol atomic weight of lithium. The small atomic weight of lithium has been a significant advantage of lithium batteries, leading to a high gravimetric capacity. Similarly, the larger ion size results in a smaller volumetric capacity of sodium-ion batteries. Although sodium is the lightest and smallest element sharing similar properties with lithium (compared to magnesium and potassium), these slight differences make it

hard for sodium-ion batteries to compete with lithium-ion batteries regarding capacity and energy density. The low redox potential of lithium ($E^0(\text{Li}^+/\text{Li}) = -3.04 \text{ V vs. SHE}$) enables the high voltage and high energy density of lithium-ion batteries. Sodium has a close standard electrode potential of -2.71 V , which is also suitable for battery applications. The theoretical capacity of lithium metal is around three times of sodium metal. With the same redox couple, the difference between theoretical capacities becomes smaller, as shown in the example of NaCoO_2 and LiCoO_2 in Table 1. Higher atomic weight, lower reducing potential, and larger ion size contribute to the major constraints for the sodium-ion batteries to achieve as high gravimetric and volumetric energy density as lithium-ion batteries. However, as shown in Table 1, sodium-ion batteries showed tremendous advantages over lithium-ion batteries at cost and material abundance. The price for sodium carbonates is around a hundred times lower than the price of lithium carbonates. While sodium resources are almost unlimited everywhere, lithium resources are constrained by insufficient abundance and uneven distribution¹⁸.

Table 1: The Comparison between sodium and lithium

| | Na | Li |
|---|--------------------------|----------------------------|
| Atomic Weight | 23 g/mol | 6.9 g/mol |
| E_0 vs. SHE | -2.71 V | -3.04V |
| Ionic Radius | 0.98Å | 0.69Å |
| Capacity (metal) | 1165 mAh/g | 3829 mAh/g |
| Capacity (ACoO_2) | 235 mAh/g | 274 mAh/g |
| Melting Point | 97.7 °C | 190.5°C |
| Coordination Preference | octahedral and prismatic | octahedral and tetrahedral |

Table 1 (cont'd)

| | | |
|--|-----------|-----------------|
| Price (Carbonates)¹⁹ | \$150/ton | \$13000/ton |
| Resources¹⁹ | unlimited | 80 million tons |

The difference between the physical properties of sodium and lithium leads to different chemistries in lithium-ion batteries and sodium-ion batteries. Besides abundance and cost, studies have found that sodium-ion batteries exhibit some other advantages over lithium-ion batteries. With a larger ion size than lithium ions, sodium ions have a preference for octahedral and tetrahedral sites, leading to O- type and P-type structures of the sodium transition metal oxides (these two structures will be discussed in the following section). First principles calculations showed that the migration barrier of sodium ions is lower than that of lithium ions in layered structures²⁰. While the similar sizes of lithium ions and transition metal ions would result in thermodynamic instability of lithium-ion transition metal oxides²¹, the larger ion size of sodium leads to the larger ionic size difference between sodium and transition metal ions, providing more options of sodium compounds for researchers.

For grid-scale battery systems, the shortcomings in capacity and energy density can be made up by increasing the number of cells, where abundance and cost are more critical than the energy density of a single stack. Despite the high competitiveness in energy density of lithium-ion batteries, sodium-ion batteries still show great potential in substituting lithium-ion batteries for large-scale energy storage applications where the energy density is not very crucial, considering the unlimited abundance and low cost of sodium.

1.2.2 The working principle of sodium-ion batteries

The working mechanism of sodium-ion batteries is almost identical to that of lithium-ion batteries. Both sodium-ion batteries and lithium-ion batteries are among the rechargeable “rocking-chair” type batteries, as the charge carriers, either sodium ions or lithium ions, are shuttling back and forth between the electrodes during charging and discharging processes. The schematic of a sodium-ion battery is shown in Figure 1.

A typical sodium-ion battery consists of two electrodes, positive and negative, both made with sodium insertion materials, separated by the electrolyte that allows sodium ions but not electrons to travel through. A voltage is produced from the chemical potential difference between the positive and negative electrode of the cell. Such potential difference drives sodium ions to be extracted from the negative electrode, pass through the electrolyte and be inserted into the positive electrode. In the meantime, electrons are lost at the negative electrode and accepted by the positive electrode, traveling through the external circuit, producing an electronic current. In such a process which we call discharge, the chemical energy is converted to the electric energy. The reverse process, when an external voltage is applied to drive sodiums ions and electrons to move in an opposite direction from the positive electrode to the negative electrode is called charge, where the electric energy is converted into chemical energy and stored in the batteries.

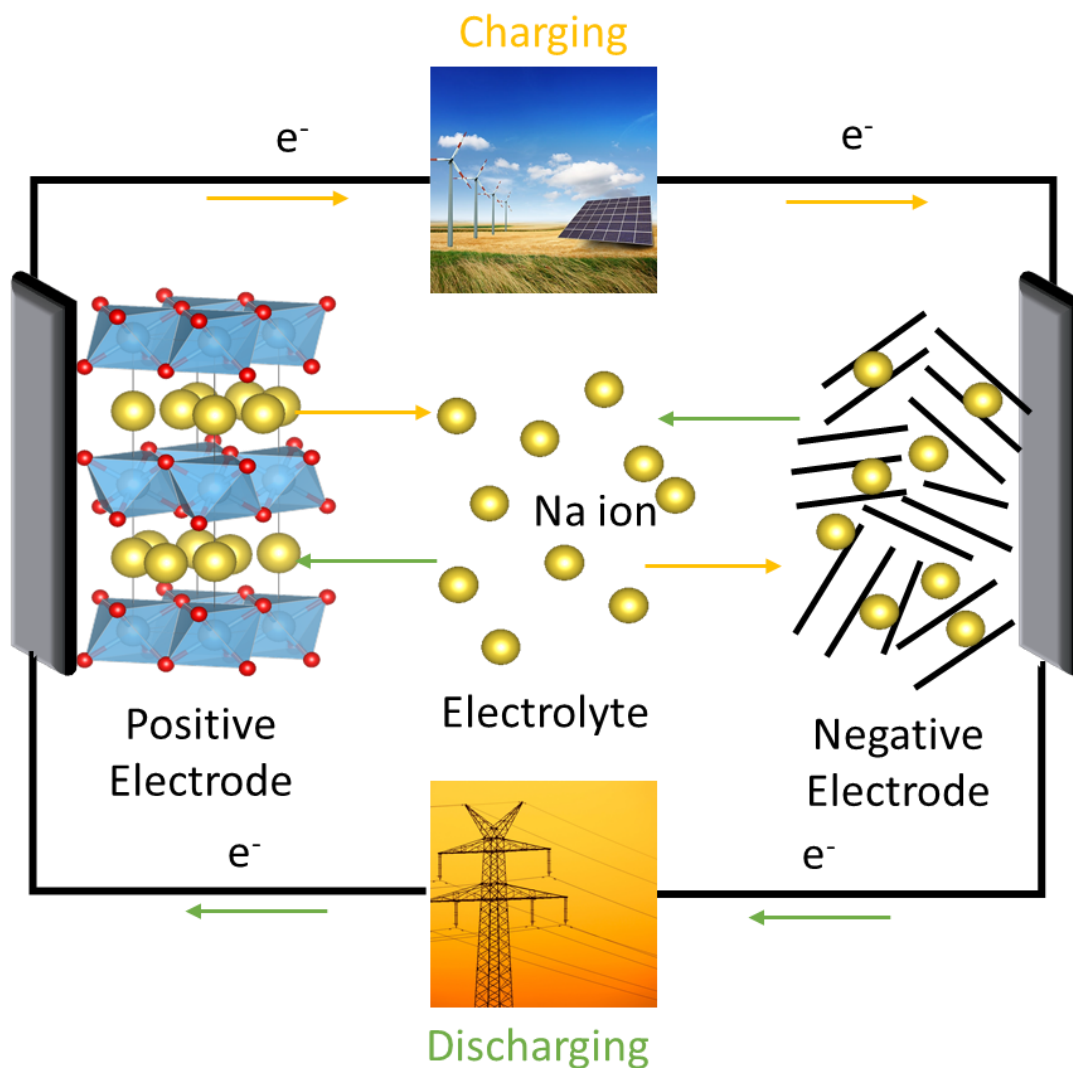


Figure 1: The schematic of a sodium-ion battery

1.3 Electrode materials for sodium-ion batteries

The selection of electrode material is critical for the development of sodium-ion batteries as the performance of the cell is largely dependent on the properties of electrode materials. The basic requirement for the operation of the battery is that the sodium ions can be inserted or extracted from the electrodes while the stable structures can be still maintained. The insertion or the extraction of the Na ions occurs with the reduction or oxidation reaction of some other elements in the electrode material, which in most cases are multivalent transition metals.

Energy density is important for batteries as it determines how much energy can be stored with a certain volume or mass. Since the energy density is the product of the operating voltage and the specific capacity, higher energy density can be accomplished by improving these two factors. The operating voltage of the cell is theoretically proportional to the chemical potential difference between the positive and negative electrode materials according to $V = -\Delta\mu/zF$, where $\Delta\mu$ is the chemical potential difference between the positive and negative electrodes, z the number of elementary charges carried by ions (1 for Na), F the Faraday constant. To achieve higher operating voltages and higher energy densities, a positive electrode material with a higher potential and a negative electrode material with a lower potential are desired. The theoretical specific capacity of the electrode is determined by how many charge carriers are contained in the unit mass material. As a result, the more Na ions can be inserted into or extracted from the unit mass electrode, the higher the theoretical specific capacity can be. However, the actual capacity of the cell that can be achieved is usually much less than the theoretical one as it is limited by the amount of sodium that can be extracted and inserted reversibly without irreversible phase transformations. Thus, the good structural stability of the electrode material at different sodium content is essential for high reversible capacity as well as long cycle life and good capacity retention. High rate capability is also required for a battery to deliver high power and to charge fast. The rate capability is also closely correlated to the properties of the electrode material as it can be limited by sodium diffusion coefficients, sodium diffusion pathways, ionic conductivity, and electronic conductivity of the electrodes. Better rate performance can be achieved by improving the ion and electron transport in the electrode material. In addition, safety, cost, and environmental-friendliness are also important factors to consider when choosing electrode materials for sodium-ion batteries.

For the development of sodium-ion batteries with high performance, the exploration and design of electrode materials that can fulfill these requirements are essential. Tremendous research efforts have been devoted to the search for electrode materials for better performance. A wide range of materials have been proposed as potential positive and negative electrode materials for sodium-ion batteries.

1.3.1 Positive electrode materials

Lithium transition metal oxides with layered structure (Li_xTMO_2 , TM stands for the transition metals like Mn, Co, Ni, V) have been widely investigated and used as positive electrode materials for lithium-ion batteries³ because of their high energy densities. Thus, their sodium analogs Na_xTMO_2 have attracted research interests. It has been found that they are promising candidates for electrode materials as they exhibited high ionic conductivity and large reversible capacities²²⁻²⁴. Moreover, sodium transition metal oxides showed advantages of safety over their lithium counterparts as the capacity loss caused by spinel formation is less likely to happen in these materials, mainly due to the larger ionic radius of sodium^{25,26}.

The structures of sodium transition metal oxides mainly fall into two categories: P-type and O-type according to Delmas²⁷, with sodium atoms occupying prismatic and octahedral sites, respectively. A number of studies have been conducted on P2-type (2 TM layers with ABBA stacking and Na occupying prismatic sites) and O3-type (3 TM layers with ABCABC stacking and Na occupying octahedral sites) Na_xTMO_2 . Structures of P2 and O3 types are shown in Figure 2. Both P2 and O3 type layered Na_xTMO_2 compounds have been investigated extensively as potential electrode materials for sodium-ion batteries. LiCoO_3 , the commercialized cathode material in lithium-ion batteries, is one of the representative materials of the O3 structure. However, the O3 Na materials exhibit different properties from the O3 Li materials as there is an O3-O'3-P3

transformation during Na extraction^{28,29}. The P2-type materials tend to present higher capacity and longer cycle life than O3 type materials, as the sodium ions are more stable in larger prismatic sites than in octahedral sites, despite the fact that the O3 type $\text{Na}_x[\text{TM}]\text{O}_2$ can be synthesized at a lower temperature compared to the P2 analogs and possess more sodium based on the stoichiometry^{30,31}. Furthermore, the sodium ions showed higher diffusion and lower diffusion barriers in P2-type Na_xTMO_2 , leading to a better rate performance^{32,33}.

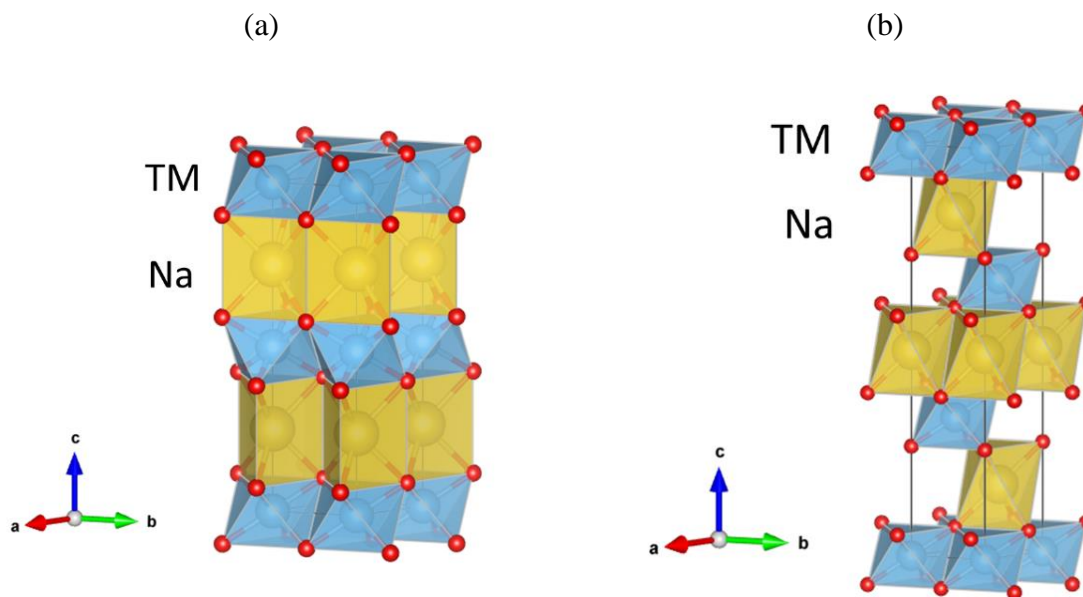


Figure 2: Schematics of (a)P2 and (b)O3 structure for Na_xTMO_2

Early studies on Na_xTMO_2 started dating back to the 1980s when the electrochemical properties of Na_xCoO_2 were studied²⁸. With resurgent research interests in sodium-ion batteries, Na_xCoO_2 has been revisited by researchers as electrode materials for sodium-ion batteries. Comparing to their analogs Li_xCoO_2 , which are widely used as cathode materials in Li-ion batteries, Na_xCoO_2 presents more complex phase transitions during the insertion and extraction of sodium ions, with multiple voltage drops and plateaus in the electrochemical curve³⁴. The phase diagram of P2-type Na_xCoO_2 was studied by Berthelot et al. with a combination of in-situ x-ray diffraction and electrochemical methods³⁵. A higher capacity but worse cycling stability was observed for the

sodium manganese oxides P2- Na_xMnO_2 . The O3-type NaMnO_2 studied by Ma et al.³⁶ showed a capacity of 185 mAh/g for the first cycle but a large capacity loss after several cycles. A capacity of 140 mAh/g in P2-type $\text{Na}_{0.6}\text{MnO}_2$ was reported by Caballero et al.³⁷. However, the capacity faded after a few cycles. The poor structure stability of Na_xMnO_2 might be related to the Jahn-Teller distortion of Mn^{3+} . Improved capacity retention was observed with different synthesis routes and electrolytes, while the cycling stability can be further improved by doping Mg into P2- $\text{Na}_{0.67}\text{MnO}_2$.³⁸

While most layered sodium transition metal oxides with a single type of transition metal may suffer from low capacity and cycling stability, attempts have been made to increase the cycling and structural stability by introducing additional transition metal elements into the material. The mixing of transition metals can improve the structural stability and affect the sodium diffusion barriers in Na_xTMO_2 ^{39,40}. A variety of binary systems were proposed and studied as promising candidates for positive electrodes such as the combination of Fe/Mn⁴¹⁻⁴⁴, Mg/Mn^{45,46}, Ni/Mn⁴⁷⁻⁴⁹. Some ternary systems were also investigated such as $\text{NaNi}_{1/3}\text{Mn}_{1/3}\text{Co}_{1/3}\text{O}_2$ ⁵⁰, $\text{Na}_{2/3}\text{Ni}_{1/3}\text{Mn}_{2/3-x}\text{Ti}_x\text{O}_2$ ⁵¹, $\text{Na}_{0.8}\text{Ni}_{0.3}\text{Co}_{0.2}\text{Ti}_{0.5}\text{O}_2$ ⁵², $\text{NaFe}_{0.4}\text{Ni}_{0.3}\text{Ti}_{0.3}\text{O}_2$ ⁵³ and $\text{Na}_{0.67}\text{Mn}_{0.65}\text{Fe}_{0.20}\text{Ni}_{0.15}\text{O}_2$ ⁵⁴.

Besides the layered sodium transition metal oxide, other materials were also studied as potential positive electrodes for sodium-ion batteries, for example, the phosphates materials, which showed better stability than the oxide materials. Moreover, phosphates materials present higher voltage than that of the metal oxides, mainly due to the inductive effect of PO_4^{3-} polyanion^{55,56}. Among the phosphates materials, olivine-type NaFePO_4 (Figure 3(a)) has attracted the most attention for the high theoretical specific capacity it could achieve as well as the success of LiFePO_4 in commercialized lithium-ion batteries. Studies have found that olivine-type NaFePO_4 can be synthesized through the ion exchange from LiFePO_4 ⁵⁷. Ali et al.⁵⁸ developed a high-

performance cathode for sodium-ion batteries using olivine-type NaFePO_4 , obtaining an excellent retention capacity of 94% after 100 cycles and a reversible capacity of 142 mAh/g. The NASICON-type phosphate materials are also promising options for positive electrodes with a flat voltage plateau and an open framework to enhance sodium transport. A storage capacity of 107 mAh/g and 93% capacity retention after 80 cycles were achieved using $\text{Na}_3\text{V}_2(\text{PO}_4)_3$ (Figure 3(b)) with as cathode and carbon nanocomposites as anodes for sodium-ion batteries in a recent study by Jian et al⁵⁹. The electrochemical performance of $\text{Na}_3\text{V}_2(\text{PO}_4)_3$ can be further improved by combining it with carbon materials^{60,61}. Ellis et al⁶². investigated the possibility of using fluorophosphate $\text{Na}_2\text{FePO}_4\text{F}$ ((Figure 3(c))) as cathodes in Na-ion batteries. With two-dimensional sodium transport pathways, it delivered a capacity of 135 mAh/g, which is 85% of the theoretical value.

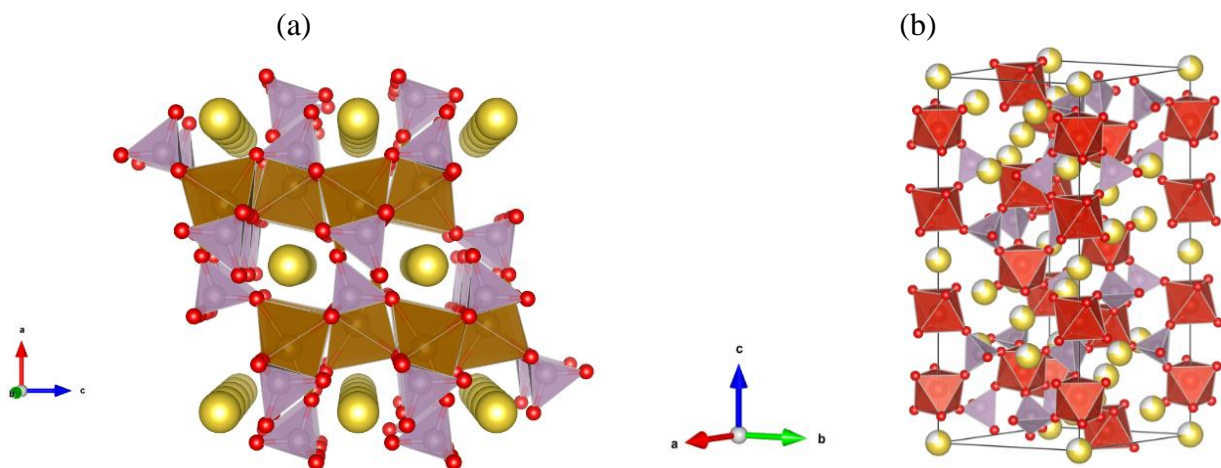
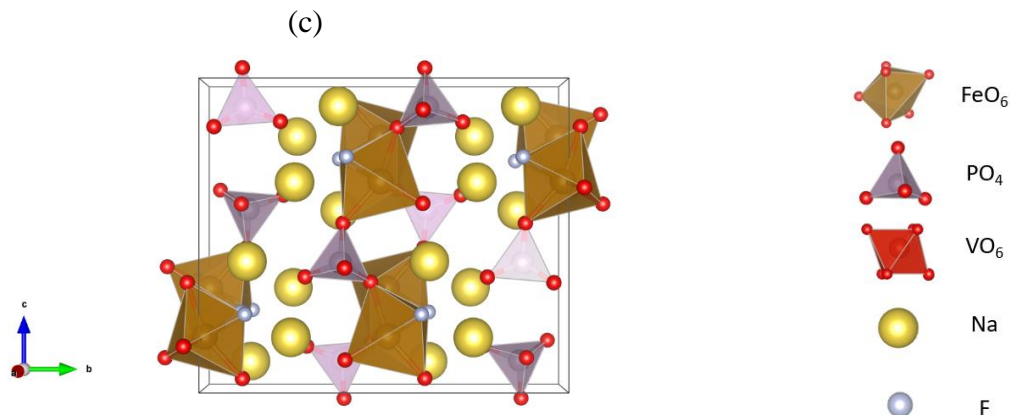


Figure 3: Schematics of structures of (a) olivine-type NaFePO_4 , (b) $\text{Na}_3\text{V}_2(\text{PO}_4)_3$ and (c) $\text{Na}_2\text{FePO}_4\text{F}$

Figure 3 (cont'd)



Fluoride compounds like NaMF₃ (M stands for the transition metal like Fe, Mn, Co, Ni, V) or MF₃ have also been studied as positive electrode materials with high voltage resulting from the highly ionic metal-ligand bonds. The initial study on NaFeF₃ (Figure 4) showed an initial discharge capacity of 130 mAh g⁻¹ while both NaMnF₃ and NaNiF₃ both showed poor electrochemical performance in a Na/Na⁺ cell⁶³. Kitajou et al.⁶⁴ synthesized highly crystalline NaFeF₃, with the obtained NaFeF₃ achieved an initial discharge capacity of 197 mAh/g in the voltage range of 1.5 V to 4.5 V, with good Coulombic efficiency. The performance of perovskite-type metal trifluorides for both Li and Na batteries, including FeF₃, TiF₃, VF₃, MnF₃, and CoF₃ was studied by Nishijima et al.⁶⁵. The FeF₃ system, with a high theoretical capacity of 712 mAh/g, showed a reversible capacity of 100 mAh/g with a discharge voltage of 2.2 V. FeF₃·xH₂O/graphene showed improved electrochemical performance with the addition of graphene⁶⁶.

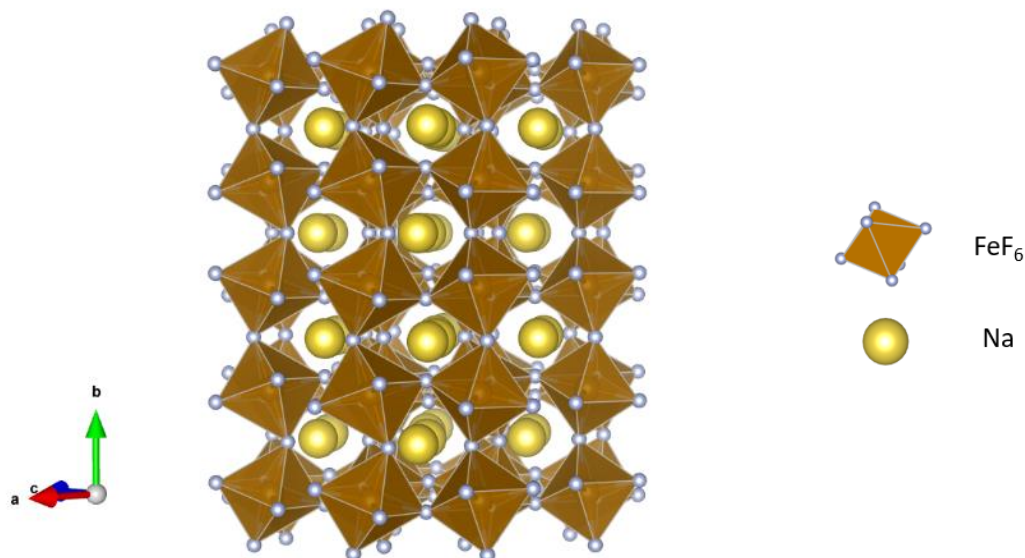


Figure 4: Schematics of the NaFeF₃ structure

Other materials being studied as positive electrode materials for sodium-ion batteries include Prussian blue analogs with a chemical formula of Na_xM1[M2(CN)₆]_y·nH₂O. The open framework of Prussian blue analogs promises efficient sodium diffusion during cycling. A few systems were investigated such as Na_{0.61}Fe[Fe(CN)₆]_{0.94}⁶⁷, Na₂Mn[Mn(CN)₆]⁶⁸, Na₂Zn₃[Fe(CN)₆]₂·nH₂O⁶⁹, Na₂Mn[Fe(CN)₆]₂·nH₂O⁷⁰. It is worth mentioning that some organic materials are also attractive candidates for positive electrodes with high gravimetric energy density and flexibility. A reversible capacity of 484 mAh/g was achieved with disodium rhodizone (Na₂C₆O₆)⁷¹. The sodium 4,4'-stilbene-dicarboxylate electrode delivered a reversible capacity of 105 mAh/g at a current density of 2 A/g⁷².

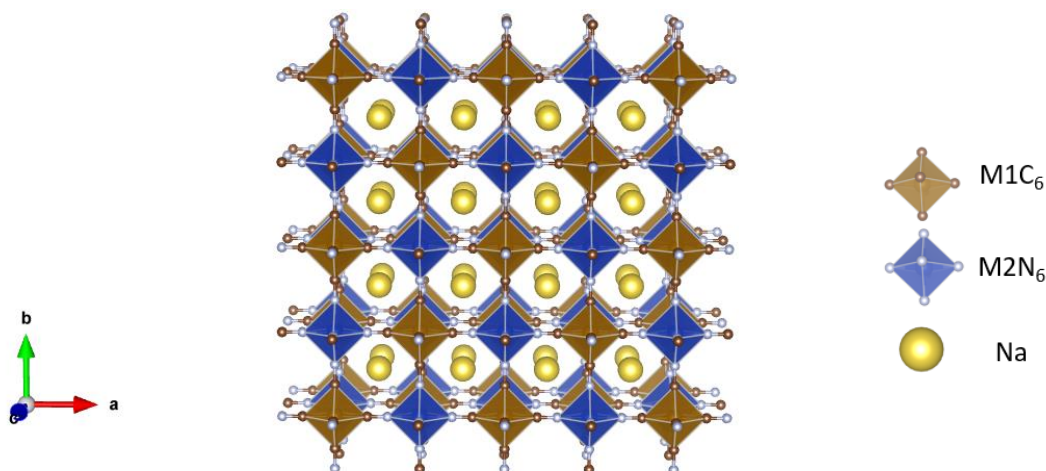


Figure 5: Structure of $\text{Na}_x\text{M1}[\text{M2}(\text{CN})_6]_y$

1.3.2 Negative electrode materials

Carbon-based materials are common materials used as anodes in batteries with high electrical conductivity and low cost. Although graphite has been widely used as anode materials in lithium-ion batteries, it is not suitable for sodium-ion batteries as sodium atoms could hardly be inserted into graphitic materials⁷³. The potential of other carbon-based materials being used as anodes in sodium-ion batteries has been investigated. Hard carbon has been identified as a promising candidate for anode materials as similar reversible insertion/extraction mechanisms have been observed for sodium and lithium in hard carbon⁷³. A high reversible capacity of 300 mAh/g was obtained by using hard carbon as the anode material for sodium-ion batteries in a study by Stevens et al⁷⁴. A study by Komaba et al.⁷⁵ attained a high overall capacity of more than 200 mAh/g and excellent reversibility using hard carbon as the anode and layered $\text{NaNi}_2\text{Mn}_{0.5}\text{O}_2$ as cathodes for the sodium-ion battery. With a modified synthesis method, a large reversible capacity of 478 mAh/g could be achieved with hard carbon⁷⁶. A study by Ding et al.⁷⁷ showed that the carbon nanosheets with larger intergraphene spacing could achieve a stable capacity of 298mAh/g and excellent cycle retention. Zhu et al.⁷⁸ developed a novel material using 30 nm Sb nanoparticles

encapsulated in 400 nm carbon fibers, leading to excellent cycle stability with only 0.06% decay per cycle and a high overall capacity with an initial capacity of 422 mAh/g.

Some transition metal oxides are also promising negative electrode materials for sodium-ion batteries with high capacity. Jiang et al.⁷⁹ investigated the performance of sodium-ion batteries using a series of transition metal oxides as anodes, including Fe₂O₃, Mn₃O₄, Co₃O₄, and NiO. The results showed that the cell with Fe₂O₃ anode exhibited a large capacity of 385 mAh/g after 200 cycles. Anatase titanium dioxide TiO₂ showed ~150 mAh/g over 100 cycles as the negative electrode in Na cells⁸⁰. Some other titanium-based compounds exhibit low potential, thus suitable for negative electrode materials. For example, Na₂Ti₃O₇ with the layered structure was identified as a promising negative electrode material for sodium-ion batteries with an average potential of 0.3 V vs Na⁺/Na⁰⁸¹. A charge capacity of 188 mAh/g of the cell was obtained using synthesized Na₂Ti₃O₇/carbon black composite as the negative electrode and sodium metal as the counter electrode⁸². O3-type NaTiO₂ delivered a reversible capacity of 152 mAh/g, corresponding to ~0.5 Na reversible intercalation⁸³. The titanium-containing sodium transition metal oxides P2-type Na_{0.66}[Li_{0.22}Ti_{0.78}]O₂ and O3-type Na_{0.66}Mg_{0.34}Ti_{0.66}O₂ as well as NASICON-type NaTi₂(PO₄)₃ have also been demonstrated to be promising candidates as negative electrode materials for sodium-ion batteries⁸⁴⁻⁸⁶.

Alloy-based negative electrode materials attract research interests as they can achieve a much higher theoretical capacity compared to intercalation-based materials. Sn, Si, P, Sb, and Ge-based materials have been studied for sodium-ion batteries⁸⁷⁻⁹¹. However, the alloy-based negative electrode materials usually suffer from large volume changes during cycling.

1.3.3 Bi-functional electrode materials

In most cases, materials with either high or low potential vs Na electrodes are considered to be suitable for positive or negative electrode materials of sodium-ion batteries, respectively. Some intercalation-based electrode materials are found to be able to function as either positive or negative electrodes, usually due to the coexistence of both high and low redox couples. Such bi-functional electrode materials enable the construction of symmetric cells where the positive and negative electrodes are made of the same material, bring additional advantages of simpler design and lower manufacturing cost. A few bi-functional electrode materials for sodium-ion batteries have been proposed and studied, including layered sodium transition metal type materials with both P2 and O3 structures such as $\text{Na}_{0.6}[\text{Cr}_{0.6}\text{Ti}_{0.4}]\text{O}_2$ ⁹², $\text{Na}_{0.66}[\text{Ni}_{0.17}\text{Co}_{0.17}\text{Ti}_{0.66}]\text{O}_2$ ⁹³, $\text{Na}_{0.5}[\text{Ni}_{0.25}\text{Mn}_{0.75}]\text{O}_2$ ⁹⁴, NASICON-type materials $\text{Na}_3\text{V}_2(\text{PO}_4)_3$ ^{95,96}, and organic materials $\text{Na}_4\text{C}_8\text{H}_2\text{O}_6$ ⁹⁷.

1.4 The $\text{Na}_{2x}[\text{Ni}_x\text{Ti}_{1-x}]\text{O}_2$ group

Among the layered sodium transition metal oxide materials, the $\text{Na}_{2x}[\text{Ni}_x\text{Ti}_{1-x}]\text{O}_2$ series have been identified as promising bi-functional electrode materials for sodium-ion batteries with coexistence of high redox potential ($E = 3.7 \text{ V vs. Na/Na}^+$) for Ni and low redox potential ($E = 0.7 \text{ V vs. Na/Na}^+$) for Ti. The P2- $\text{Na}_{2/3}[\text{Ni}_{1/3}\text{Ti}_{2/3}]\text{O}_2$ showed good electrochemical performance, delivering a reversible capacity around 75 mAh/g as either cathodes or anodes⁹⁸. The symmetric cell built with O3-type $\text{Na}_{0.8}[\text{Ni}_{0.4}\text{Ti}_{0.6}]\text{O}_2$ as both positive and negative electrode delivered a reversible discharge capacity of 85 mAh/g with good rate capability⁹⁹.

The structures of P2-type and O3-type $\text{Na}_{2x}[\text{Ni}_x\text{Ti}_{1-x}]\text{O}_2$ are shown in Figure 2. As discussed above, in P2-type $\text{Na}_{2x}[\text{Ni}_x\text{Ti}_{1-x}]\text{O}_2$, Ni/Ti atoms are distributed in the 2 transition metal layers in the unit cell with Na ions occupying the Prismatic sites. In P2 $\text{Na}_{2x}[\text{Ni}_x\text{Ti}_{1-x}]\text{O}_2$, the Na

ions are distributed in two sites, the edge and face-sharing sites (Na_e and Na_f in Figure 6)), depending on whether Na prisms are sharing edges or faces with the TMO_6 octahedra. In O3 type $\text{Na}_{2x}[\text{Ni}_x\text{Ti}_{1-x}]\text{O}_2$, Ni/Ti atoms are distributing in the 3 transition metal layers in the unit cell with Na ions occupying the Octahedral sites. In both P2 and O3 $\text{Na}_{2x}[\text{Ni}_x\text{Ti}_{1-x}]\text{O}_2$, no evidence of the ordering of Ni/Ti or Na/vacancy was found from powder X-ray diffraction experiments^{100,101}. The disordered distribution of Ni/Ti and Na/vacancy (especially for P2-type with Na occupying two different sites) lead to complex local structural features of $\text{Na}_{2x}[\text{Ni}_x\text{Ti}_{1-x}]\text{O}_2$ and also raise questions on how these structural features affect the dynamic and electronic properties of the material.

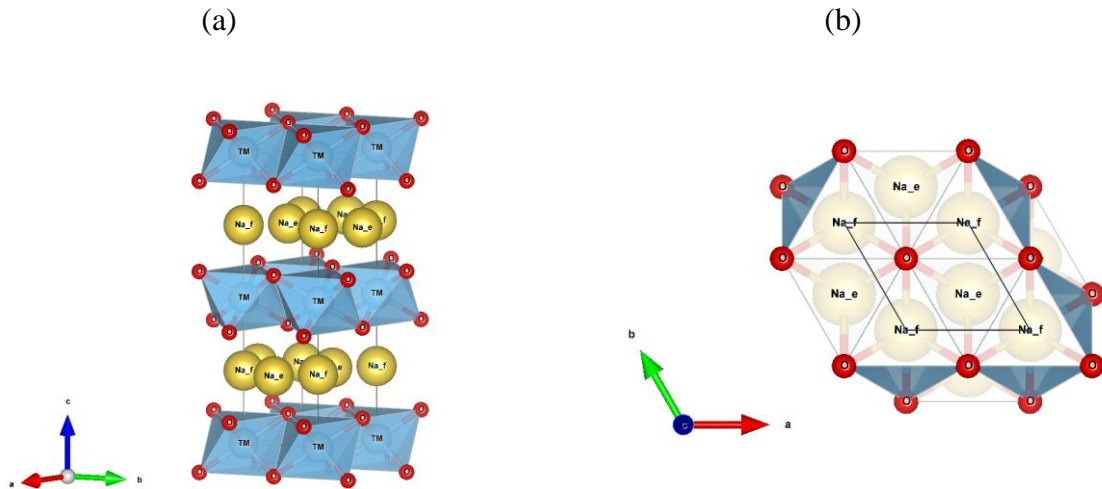


Figure 6: The distribution of Na ions in edge-sharing and face-sharing sites in P2-
 $\text{Na}_{2x}[\text{Ni}_x\text{Ti}_{1-x}]\text{O}_2$ viewed (a) along the ab plane (b) along the c axis.

A few studies have been performed to study the properties of $\text{Na}_{2x}[\text{Ni}_x\text{Ti}_{1-x}]\text{O}_2$. Electrochemical experiments have been conducted for both P2 and O3 $\text{Na}_{2x}[\text{Ni}_x\text{Ti}_{1-x}]\text{O}_2$ to assess the cycling performance^{98,102} as well as the transport properties^{103,104}. The structural stability of $\text{Na}_{2x}[\text{Ni}_x\text{Ti}_{1-x}]\text{O}_2$ during cycling was investigated using in situ x-ray diffractions^{105,106}. However, the fundamental understandings of this material series and the underlying mechanism during the electrochemical processes are still limited.

1.5 Thesis overview

With the general background information provided above, including an introduction of the sodium-ion batteries, a discussion of its significance to address the environmental challenges and a review of the research progress on some electrode materials for sodium-ion batteries, this thesis aims to seek the answers to the fundamental research questions related to $\text{Na}_{2x}[\text{Ni}_x\text{Ti}_{1-x}]\text{O}_2$ as bi-functional electrode materials for sodium-ion batteries. For example, how would the complex local structure caused by disordered Na/vacancy and Ni/Ti impact the dynamics of Na in the material? How would the atomic and electronic structure change during the electrochemical processes when the Na ions are being inserted and extracted from the material? What redox reactions would occur when the material is used as either a positive or negative electrode? How do Na ions diffuse in the material and how to enhance diffusion? How does the diffusion mechanism differ in P2 and O3 structures? How are the atomic-scale features related to the macroscopic electrochemical properties and further the battery performance? These questions will be addressed in the following chapters. The answers to them not only help us to gain a better atomic-level understanding of this material but also provide insights on further improving the performance of similar materials as well as the discovery and design of the new electrode materials.

CHAPTER 2 provides a brief introduction of the theoretical backgrounds of the computational and experimental methods and how they are applied in this thesis. CHAPTER 3 investigates the average and local structure of $\text{P2-Na}_{2/3}[\text{Ni}_{1/3}\text{Ti}_{2/3}]\text{O}_2$ using a combination of Rietveld refinement on neutron diffraction datasets and atomistic simulation. Two potential sets are applied for the atomistic simulation and the energetics of atomic distribution and ordering are discussed. In CHAPTER 4, the structural and electronic properties of $\text{P2-Na}_x[\text{Ni}_{1/3}\text{Ti}_{2/3}]\text{O}_2$ are investigated using density functional theory. The structural and electronic change of P2-

$\text{Na}_x[\text{Ni}_{1/3}\text{Ti}_{2/3}]\text{O}_2$ are examined as Na ions inserted and extracted from the material during charging/discharging. The density of states, electron density distribution, and electronic conductivities are calculated and discussed in this chapter. In CHAPTER 5 the diffusion mechanism as well as ionic conductivity $\text{P2-Na}_{2/3}[\text{Ni}_{1/3}\text{Ti}_{2/3}]\text{O}_2$ are investigated with a combination of experimental and computational techniques. The quasi-elastic neutron scattering (QENS) experiments and molecular dynamics (MD) simulations based on interatomic potential (IP) and density functional theory (DFT) are performed to identify the diffusion mechanism. CHAPTER 6 extends the analysis to the O3 system with the use of machine learning based interatomic potential models. CHAPTER 7 summarizes the work in this thesis and discusses the future directions based on this work.

CHAPTER 2 Methods

2.1 Computational methods

2.1.1 Density functional theory

Density functional theory (DFT)¹⁰⁷ is a computational method to investigate the ground state electronic structures of materials and has been a useful tool to study properties of electrode materials including the phase stability¹⁰⁸, defect energetics¹⁰⁹, order/disorder phenomenon¹¹⁰, conduction pathways, and migration activation energies²⁰. In Kohn-Sham¹¹¹ DFT calculations, the interacting many-body system is simplified to non-interacting single-electron systems with an effective potential V_{eff} , resulting in a set of single-electron Schrödinger-like equations as in Eq. 1.

$$\left[-\frac{\hbar^2}{2m} \nabla^2 + V_{\text{eff}}(r) \right] \psi_i(r) = \varepsilon_i \psi_i(r) \quad \text{Eq. 1}$$

Where $\psi_i(\mathbf{r})$ are the Kohn-Sham orbitals, which relate to the spatially dependent electron density $n(\mathbf{r})$ according to $n(\mathbf{r}) = \sum_{i=1}^N |\varphi_i(\mathbf{r})|^2$. The total electron energy E of many-body systems is determined as functionals of $n(\mathbf{r})$:

$$E[n(\mathbf{r})] = T[n(\mathbf{r})] + V_e n[n(\mathbf{r})] + E_H[n(\mathbf{r})] + E_{\text{xc}}[n(\mathbf{r})] \quad \text{Eq. 2}$$

Where T is the non-interacting kinetic energy, V_{en} the electron-nuclei interaction energy, E_H the Hartree term for the electron-electron Coulomb interaction, and E_{xc} the exchange-correlation energy. The first three terms in Eq. 2 can be determined according to the following equations:

$$T[n(\mathbf{r})] = -\frac{\hbar^2}{2m} \sum_{i=1}^N \int \psi_i^*(r) \nabla^2 \psi_i(r) dr \quad \text{Eq. 3}$$

$$V_{\text{en}}[n(\mathbf{r})] = -\sum_j \int \frac{Ze^2}{|\mathbf{r}_j - \mathbf{R}_j|} n(\mathbf{r}) d\mathbf{r} \quad \text{Eq. 4}$$

$$E_H[\rho] = \frac{e^2}{2} \int d\mathbf{r} \int d\mathbf{r}' \frac{\rho(\mathbf{r})\rho(\mathbf{r}')}{|\mathbf{r} - \mathbf{r}'|} \quad \text{Eq. 5}$$

The exchange-correlation energy $E_{xc}[n(\mathbf{r})]$ consists of exchange energy $E_x[n(\mathbf{r})]$ and correlation energy $E_c[n(\mathbf{r})]$, accounting for the exchange and correlation interactions between electrons, respectively. $E_{xc}[n(\mathbf{r})]$ is the only unknown term in Eq. 2 and can be approximated by functionals in DFT calculations, for example, local-density approximation (LDA) and generalized gradient approximation (GGA). In LDA, $E_{xc}[n(\mathbf{r})]$ depends on the local densities only as in Eq. 6:

$$E_{xc}^{LDA}[n(\mathbf{r})] = \int d\mathbf{r} n(\mathbf{r}) \epsilon_{xc}(n(\mathbf{r})) \quad \text{Eq. 6}$$

where ϵ_{xc} is the exchange-correlation energy of homogeneous electron gas of density $n(\mathbf{r})$. In GGA, $E_{xc}[n(\mathbf{r})]$ depends on not only the local densities but also the first derivative of densities as in Eq. 7:

$$E_{xc}^{GGA}[n(\mathbf{r})] = \int f^{GGA}[n(\mathbf{r}), \nabla n(\mathbf{r})] d\mathbf{r} \quad \text{Eq. 7}$$

where f^{GGA} is a function of electron densities $n(\mathbf{r})$ and their gradients $\nabla n(\mathbf{r})$. GGA exchange-correlation functionals that are commonly used include PBE¹¹², PW91¹¹³, BLYP^{114,115} and PBEsol¹¹⁶. We used PBE functionals for all the DFT calculations of the $\text{Na}_{2x}[\text{Ni}_x\text{Ti}_{1-x}]\text{O}_2$ series in this work.

While LDA and GGA approximations have been successfully applied to predict properties for most materials, they can produce large errors when dealing with the electron correlation effects in the 3d localized orbitals of transition metal oxides¹¹⁷. A GGA+U approach¹¹⁸ was employed for $\text{Na}_{2x}[\text{Ni}_x\text{Ti}_{1-x}]\text{O}_2$ in this work to account for the electron localization of Ni ions. It is also worth mentioning that the standard Kohn-Sham DFT calculations do not include the long-range correlations to treat weak van der Waals (vdW) interactions in layered materials. This can be remedied by adding an atom-pairwise dispersion term E_{disp} to Eq. 2. The dispersion-corrected PBE

functional with Becke-Jonson damping (PBE-D3BJ) functional^{119,120} was used for layered $\text{Na}_{2x}[\text{Ni}_x\text{Ti}_{1-x}]\text{O}_2$ in this thesis.

With the self-consistent solutions calculated in DFT, the ground state electron density for minimized structure is obtained. The topological analysis of electron density can be utilized to investigate materials properties, for example, atomic charges, bond orders, atomic energies, and atomic volumes. The common models to assign electron densities to each atom include Density Derived Electrostatic and Chemical (DDEC) charges¹²¹, Bader charges¹²², Hirshfeld charges¹²³, and Mulliken charges¹²⁴. Considering that the Hirshfeld charge model tends to underestimate the charge^{125,126} and the Mulliken charge model is sensitive to the basis sets^{127,128}, DDEC6 and Bader models are applied to calculate the atomic charges in this thesis. The DDEC charge model assigns electron densities to atoms by reproducing the chemical states while the Bader charge model assigns the charges based on the zero flux surfaces.

2.1.2 Interatomic potential model

While the DFT calculations provide relatively accurate evaluations of energies and forces, the high computational cost has limited the time and length scale accessible to DFT. Compared to DFT calculations, the interatomic potential (IP) model with much lower costs can be applied to investigate systems with hundreds of thousands of atoms and up to microseconds. The interatomic potential model describes the interatomic interactions as a function of the atomic positions thus the potential energy of a system U is expressed as Eq. 8:

$$\begin{aligned}
 U = & \sum_i U_{1,i}(\mathbf{r}_i) + \sum_i \sum_{i<j} U_{2,(i,j)}(\mathbf{r}_i, \mathbf{r}_j) \\
 & + \sum_i \sum_{i<j} \sum_{j<k} U_{3,(i,j,k)}(\mathbf{r}_i, \mathbf{r}_j, \mathbf{r}_k) + \dots
 \end{aligned}
 \tag{Eq. 8}$$

where U_1 , U_2 , U_3 are the one-body, two-body and three-body terms, \mathbf{r} the positions of the atoms.

2.1.2.1 Empirical interatomic potential model

The empirical IP model is based on analytical functions that are derived from physical principles. Parameters for these analytical functions in the empirical IP model can be obtained either from the first-principles results¹²⁹ or based on the empirical fit to experimental data^{130,131}. A widely-used empirical interatomic potential model is the pair potential Lenard-Jones (LJ)¹³² potential, which defines the potential U as a function of the distance between two particles r with two parameters ε and σ :

$$U^{\text{Lennard-Jones}}(r) = 4\varepsilon \left[\left(\frac{\sigma}{r} \right)^{12} - \left(\frac{\sigma}{r} \right)^6 \right] \quad \text{Eq. 9}$$

The LJ potential consists of a short-range repulsive term (r^{-12}) and a long-range attractive term (r^{-6}). A wide range of different IP models have been developed to address different systems and different problems, for example, the embedded atom method (EAM)¹³³ and Finnis-Sinclair potentials¹³⁴ for metallic materials, Tersoff¹³⁵ and Stillinger-Weber¹³⁶ for covalent materials, ReaxFF¹³⁷ and Charge Optimized Many Body potential (COMB)¹³⁸ as reactive potentials for more complex systems.

For ionic materials like oxides materials $\text{Na}_{2x}[\text{Ni}_x\text{Ti}_{1-x}]\text{O}_2$ studied in this thesis, pairwise potentials are commonly used, typically consisting of the long-range electrostatic interactions defined by the Coulombic law and the short-range interactions for the repulsion between atoms. For the electrostatic interactions, the atoms can be represented as either fixed point charges at atomic centers or polarization models, with the former neglecting the effect of polarization. Classical polarization models include the core-shell (or Drude oscillator) model¹³⁹, induced-dipole model¹⁴⁰, and fluctuation charge model¹⁴¹. The schematics of the non-polarizable model and these

polarization models are shown in Figure 7¹⁴². In the core-shell model, each atom is split into two charged sites, core and shell, with a fixed total charge. The shell is connected to the core atom with a harmonic spring. In the induced dipole model, the polarizable atoms are represented as induced dipoles with an induced dipole moment μ proportional to the external electric field. In the fluctuation charge model or the chemical potential equilibration model, the atomic charges can be changed during the simulation to be redistributed to make the electronegativity equal to the chemical potential.

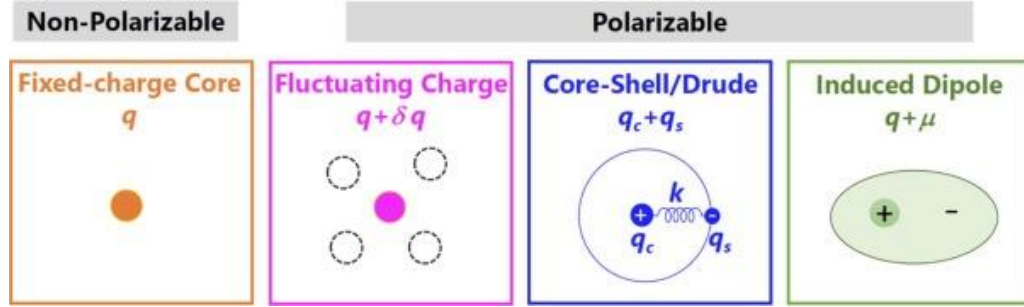


Figure 7: The schematics of non-polarizable fixed charge model and polarization models including fluctuating charge model, core-shell model and induced dipole model¹⁴²

The core-shell model and induced dipole model are applied in this thesis. The common models to describe the short-range pairwise interactions include Buckingham¹⁴³ and Morse¹⁴⁴ potential model used in this work, with the potentials expressed as the following equations:

$$U^{Buckingham}(r) = Ae^{(-r/\rho)} - Cr^{(-6)} \quad \text{Eq. 10}$$

$$U^{Morse}(r) = D \left[(1 - e^{(-a(r-r_0))})^2 - 1 \right] \quad \text{Eq. 11}$$

where r is the distance between two interacting atoms, A , C , ρ , D , r_0 are the parameters in the models.

2.1.2.2 Machine-learning based interatomic potential model

Unlike empirical interatomic potential models, machine learning (ML) based potentials do not use physics-derived functional forms to describe the atomic interactions but mathematical functions to represent the potential energy surface. The ML-based IP model is constructed using machine learning techniques with a reference data set containing accurate energies and forces for different configurations. The reference data set is typically generated with quantum mechanical calculations such as DFT. With the reference data, descriptors representing the local environment of each atom in a mathematical way are used as inputs for the machine learning process. Commonly used atomic descriptors include atom-centered symmetry functions (ACSF)¹⁴⁵, smooth overlap of atomic positions (SOAP)¹⁴⁶, Coulomb matrix¹⁴⁷, bispectrum of the atomic neighbor density¹⁴⁸. A few approaches to construct ML-based potentials have been developed with different descriptors and machine learning algorithms, such as neural network (NN) potentials¹⁴⁹, Gaussian approximation potentials (GAP)¹⁴⁸, spectral neighbor analysis potentials (SNAP)¹⁵⁰ and moment tensor potentials¹⁵¹.

NN potential models with atom-centered symmetry functions (ACSF) were developed for $\text{Na}_{2x}[\text{Ni}_x\text{Ti}_{1-x}]\text{O}_2$ in this thesis. Both radial symmetry functions G_i^2 (Eq. 12) and angular symmetry functions G_i^4 (Eq. 13) are used as descriptors.

$$G_i^2 = \sum_j e^{-\eta(R_{ij}-R_s)^2} \cdot f_c(R_{ij}) \quad \text{Eq. 12}$$

$$G_i^4 = 2^{1-\zeta} \sum_{j,k \neq i}^{\text{all}} (1 + \lambda \cos \theta_{ijk})^\zeta \cdot e^{-\eta(R_{ij}^2 + R_{ik}^2 + R_{jk}^2)} \cdot f_c(R_{ij}) \cdot f_c(R_{ik}) \cdot f_c(R_{jk}) \quad \text{Eq. 13}$$

R_{ij} is the distance between atoms i and j . θ_{ijk} is the angle formed by R_{ij} and R_{ik} , centered at atom i . η , R_s , λ and ζ are parameters in the symmetry functions. $f_c(R_{ij})$ is the cutoff function defined as Eq. 14 with the cutoff radius R_c .

$$f_c(R_{ij}) = \begin{cases} 0.5 \cdot \left[\cos \left(\frac{\pi R_{ij}}{R_c} \right) + 1 \right] & \text{for } R_{ij} \leq R_c \\ 0 & \text{for } R_{ij} > R_c \end{cases} \quad \text{Eq. 14}$$

Neural networks consisting of an input layer, an output layer, and one or more hidden layers in between are used to construct NN potentials. For each atom, a set of atomic descriptors $\{G_i\}$ is supplied in the input layer, then passed to the hidden layers, to calculate the energy contribution of this atom in the output layer. The schematic of such neural network architecture with two hidden layers is shown in Figure 8. At each node i in the layer j , the value x_i^j is calculated from a linear combination of the output values y_k^{j-1} at each connected node k in the preceding layer $j-1$ as in Eq. 15. A nonlinear activation function f_i^j is applied to yield y_i^j at node i in layer j through $y_i^j = f_i^j(x_i^j)$.

$$x_i^j = b_i^j + \sum_{k=1}^{N_{j-1}} a_{k,i}^{j-1,j} \cdot y_k^{j-1} \quad \text{Eq. 15}$$

Weight parameters $\{a\}$ and the bias weights $\{b\}$ are optimized during the training process to minimize the root mean squared error (RMSE) of the energies and forces of the train set.

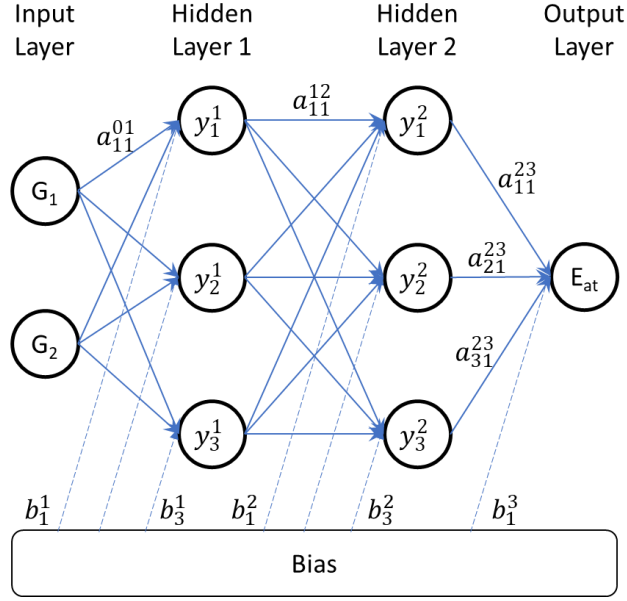


Figure 8: The schematic of a neural network architecture to construct interatomic potentials. G_i are the atomic descriptors. E_{at} is the atomic energy. y_i^j is the output value at node i in layer j . $a_{k,i}^{j-1,j}$ is the weights connecting node k in layer $j-1$ to the node i in the layer j .

b_i^j is the bias for node i in layer j .

2.1.3 Molecular dynamics simulation

The molecular dynamics (MD) simulation records the time evolution of the atoms and molecules in the system based on Newton's equation. Depending on how the potential energy is determined, MD simulations can be carried out with different physical models including the first principles calculations like DFT and parametric models like IP models. The forces are calculated as the derivatives of the potential energy $\mathbf{F} = -\nabla U(\mathbf{r})$. The motions of the particle follow Newton's law as in classical mechanics:

$$\mathbf{F}_i = m_i \frac{d^2 r_i(t)}{dt^2} \quad \text{Eq. 16}$$

Where \mathbf{F}_i is the force acting on particle i at position \mathbf{r} with mass m_i at time t . With initial positions and velocities assigned for each particle in the system, the next positions of particles can

be predicted based on Eq. 16 after a short time step Δt . Numerical integration methods are combined with Eq. 16 to evolve the motions and predict the position $\mathbf{r}_i(t+\Delta t)$ at time $t+\Delta t$ based on known position $\mathbf{r}_i(t)$ at time t . The Verlet integration is commonly used as in Eq. 17 which provides good numerical stability and time-reversibility.

$$\mathbf{r}(t + \Delta t) = 2\mathbf{r}(t) - \mathbf{r}(t - \Delta t) - \frac{1}{m} \frac{dU(\mathbf{r}(t))}{d\mathbf{r}} \Delta t^2 \quad \text{Eq. 17}$$

To study the system under different thermodynamic states, MD simulations are performed with different ensembles such as microcanonical ensemble (NVE), canonical ensemble (NVT), and isobaric-isothermal ensemble (NPT). The NVE ensemble corresponds to an isolated system with the number of atoms (N), the volume of the system (V), and the total energy (E) conserved. In the NVT ensemble, N and V along with the temperature of the system (T) are conserved. The system is coupled to a thermostat, which regulates the temperature through the modifications of the velocities of the particles. Popular thermostats used in MD simulations include the Berendsen thermostat¹⁵², Anderson thermostat¹⁵³, and Nosé-Hoover thermostat^{154,155}. The number of atoms (N), the pressure (P), and the temperature of the system (T) are conserved in an NPT ensemble. A barostat is applied along with a thermostat to control the pressure and temperature, such as Berendsen thermostat¹⁵² and Parrinello-Rahman barostat¹⁵⁶.

2.2 Experimental methods

2.2.1 Sample preparation

In this thesis, $\text{Na}_{2/3}[\text{Ni}_{1/3}\text{Ti}_{2/3}]\text{O}_2$ powders were all synthesized by solid-state reactions. The solid-state synthesis method has been commonly used to synthesize ceramic materials and has been used to prepare $\text{Na}_{2x}[\text{Ni}_x\text{Ti}_{1-x}]\text{O}_2$ successfully in previous studies^{98,157}. Stoichiometric amounts of Na_2CO_3 ($\geq 99.5\%$), NiO (99%), and TiO_2 ($\geq 99\%$) precursor powders, all from Sigma-

Aldrich were mixed, dry-milled, and fired at 900 °C for 12 hours. 10% excess of Na₂CO₃ powders were added to compensate for volatility losses during the high temperature process.

2.2.2 Neutron diffraction and Rietveld refinement

Neutron diffraction, based on the elastic scattering of neutrons, is a powerful materials characterization technique to extract the structural information of the sample material. As neutrons are scattered by the sample, there is an exchange of momentum $\hbar\mathbf{Q} = \hbar(\mathbf{k}_s - \mathbf{k}_i)$, where \hbar is reduced Planck's constant, \mathbf{k}_i and \mathbf{k}_s the incident and scattered wave vectors respectively and \mathbf{Q} the scattering vector. In the elastic neutron scattering process, the energy of incident neutrons equals the energy of the scattered neutrons. Compared to X-ray diffraction, neutron diffraction provides a more reliable and accurate estimation of the atomic displacement parameters (ADP) as neutrons are scattered by nuclei. Moreover, with similar numbers of electrons but different neutron scattering power, Ni and Ti can be more easily differentiated in neutron scattering experiments than in X-ray diffraction. From the diffraction experiments, the structural information of the materials such as the lattice parameters and atomic positions can be obtained based on a quantitative analysis of the diffraction pattern such as the peak positions and peak intensities. The Bragg's peak positions are determined based on the relationship between the distance between lattice planes d , the scattering angle θ and the wavelength λ described as Bragg's Law $\lambda = 2d \sin \theta$. For a diffraction peak from (hkl) planes in perfect crystal materials, the peak intensity I_{hkl} is related to the structure factor F_{hkl} by

$$I_{hkl} \propto |F_{hkl}|^2 = \left| \sum_j b_j \cdot e^{2\pi i(h \cdot x_j + k \cdot y_j + l \cdot z_j)} \right|^2 \quad \text{Eq. 18}$$

where b_j is the neutron scattering length of the j^{th} atom and depends on the isotope.

Rietveld refinement¹⁵⁸ is commonly used as a quantitative analysis of the diffraction data to extract detailed information of the structure, based on a least-square fitting of the calculated pattern to the observed pattern. With an initial guess of the structure, the diffraction pattern can be calculated with known peak positions and intensities. The structural parameters including lattice parameters, atomic positions, occupancies, atomic displacement parameters, as well as the profile parameters including background, peak shape and width are refined to minimize the sum of squared residuals:

$$\sum_i w_i (y_i^{obs} - y_i^{calc})^2 \quad \text{Eq. 19}$$

where y_i^{obs} and y_i^{calc} are the observed and calculated intensity of the i^{th} data point, respectively, w_i the weighting factor.

Different parameters can be calculated to assess the quality of the fitting, for example, the commonly used parameter weighted profile R-factor (R_{wp}):

$$R_{wp} = \left\{ \sum_i w_i (y_i^{obs} - y_i^{calc})^2 / \sum_i w_i \{(y_i^{obs})^2\} \right\}^{1/2} \quad \text{Eq. 20}$$

2.2.3 Quasi-elastic neutron scattering

In interactions between neutrons and the sample, the elastic scattering of neutrons with zero energy transfer can be used to determine the structure information as in neutron diffraction experiments. The rotational and translational motions of atoms and molecules can result in a distribution of energy exchanges in a small range (typically within 1 meV). Such a scattering process is called quasi-elastic neutron scattering (QENS) and can be used to investigate the diffusion in the sample¹⁵⁹. QENS experiments provide both temporal and microscopic spatial information on atomic dynamics and can provide experimental verification to the computational

results on diffusion behaviors. QENS experiments are commonly used accompanied by MD simulations as they probe the diffusion behaviors at similar length and time scales^{160,161}.

With both energy transfer and momentum transfer occurring in QENS, the intensity is measured as a function of momentum/wave vector \mathbf{Q} and energy/ frequency ω in the QENS experiment, related to the dynamical structure factor $S(\mathbf{Q}, \omega)$. The incoherent and coherent structure factors $S_{\text{inc}}(\mathbf{Q}, \omega)$ and $S_{\text{coh}}(\mathbf{Q}, \omega)$ are the Fourier transform of self and collective intermediate scattering functions $I_{\text{self}}(\mathbf{Q}, t)$ and $I_{\text{coll}}(\mathbf{Q}, t)$, respectively:

$$S_{\text{inc}}(\mathbf{Q}, \omega) = \frac{1}{2\pi} \int_{-\infty}^{+\infty} I_{\text{self}}(\mathbf{Q}, t) \exp(-i\omega t) dt \quad \text{Eq. 21}$$

$$S_{\text{coh}}(\mathbf{Q}, \omega) = \frac{1}{2\pi} \int_{-\infty}^{+\infty} I_{\text{coll}}(\mathbf{Q}, t) \exp(-i\omega t) dt \quad \text{Eq. 22}$$

$$I_{\text{self}}(\mathbf{Q}, t) = \frac{1}{N} \left\langle \sum_i \exp(-i\mathbf{Q} \cdot [\mathbf{R}_i(t) - \mathbf{R}_i(0)]) \right\rangle \quad \text{Eq. 23}$$

$$I_{\text{coll}}(\mathbf{Q}, t) = \frac{1}{N} \sum_j \sum_i \langle \exp(-i\mathbf{Q} \cdot [\mathbf{R}_j(t) - \mathbf{R}_i(0)]) \rangle \quad \text{Eq. 24}$$

For continuous long-range translational diffusion following Fick's Law, the self intermediate scattering function is related to the self-diffusivity D according to

$$I_{\text{self}}(\mathbf{Q}, t) = \exp(-\Gamma t) = \exp(-D\mathbf{Q}^2 t) \quad \text{Eq. 25}$$

In energy space, the incoherent scattering function is a Lorentzian peak:

$$S_{\text{inc}}(Q, \omega) = \frac{1}{\pi} \frac{\Gamma}{\omega^2 + (\Gamma)^2} = \frac{1}{\pi} \frac{DQ^2}{\omega^2 + (DQ^2)^2} \quad \text{Eq. 26}$$

which can be observed as a broadening of the elastic peak with a half-width-half-maximum (HWHM) or Γ of DQ^2 .

At smaller distances or large Q , the local motions of the particles may not occur following Fick's law but in jumps, where the Q -dependence of Γ would deviate from $\Gamma = DQ^2$. In this case,

the Q-dependence of Γ can be described by jump diffusion models such as Chudley-Elliott (CE) jump model¹⁶² and the Singwi-Sjölander (SS) jump model¹⁶³ we applied in this work:

$$\text{CE model: } \Gamma = \frac{1}{\tau} \left(1 - \frac{\sin(Qd)}{Qd}\right) \quad \text{Eq. 27}$$

$$\text{SS model: } \Gamma = \frac{1}{\tau} \left(\frac{Q^2 \langle r^2 \rangle / 6}{1 + Q^2 \langle r^2 \rangle / 6}\right) \quad \text{Eq. 28}$$

where the jumps are characterized by the residence time τ and the constant jump length d in the CE model or the mean jump distance r in the SS model.

CHAPTER 3 Structural properties of P2-Na_{2/3}[Ni_{1/3}Ti_{2/3}]O₂

3.1 Introduction

While sodium host materials rely on the rapid ion and electron conduction processes to achieve good sodium intercalation properties, it is important to understand the average and local structural features of P2-Na_{2/3}[Ni_{1/3}Ti_{2/3}]O₂, which are closely related to these conduction processes. In P2-Na_{2/3}[Ni_{1/3}Ti_{2/3}]O₂, the partial occupancy of Na atoms over two different sites and disordered distribution of Ni and Ti atoms lead to complex local structural features of P2-Na_{2/3}[Ni_{1/3}Ti_{2/3}]O₂, which have not been fully understood yet.

The average structure of P2-Na_{2/3}[Ni_{1/3}Ti_{2/3}]O₂ can be obtained from time-of-flight neutron diffraction based on the Rietveld refinement. Besides the structural information from the previous study based on x-ray diffraction¹⁰⁰, the atomic displacement parameters (ADP) at different temperatures, which are also correlated with partial occupancies, can be more accurately obtained by neutron diffraction. The refined structure from neutron diffraction can provide an initial configuration for atomistic modeling. Classical simulations based on force fields are particularly useful to study disordered materials as they allow the exploration of the broad energy landscape by evaluating a large number of initial configurations¹⁶⁴⁻¹⁶⁹. In this chapter, the average and local structural properties and energetics of atomic distribution in P2-Na_{2/3}[Ni_{1/3}Ti_{2/3}]O₂ are investigated using neutron diffraction and force-field based atomistic simulations.

3.2 Average structural information from Rietveld refinement

Time-of-flight (TOF) neutron diffraction experiments were performed at 15 K and 300 K with the POWGEN diffractometer at Spallation Neutron Source (SNS) of Oak Ridge National Laboratory (ORNL) to study the average structure of P2-Na_{2/3}[Ni_{1/3}Ti_{2/3}]O₂. The software package JANA2006¹⁷⁰ was used to perform the Rietveld refinement to analyze the neutron diffraction data

and plot the nuclear density maps. Although anisotropic thermal displacement is physically more realistic in these complex oxides, we obtained negative atomic displacement parameters (ADP) values for transition metal atoms during the refinement procedure. Hence, an isotropic model was applied for nickel and titanium atoms while anisotropy was maintained for the remaining atoms. The structural model based on the $P63/mmc$ space group simulated the observed Bragg peak positions accurately as shown in Figure 9. The bump at the d spacing of ~ 4.2 Å could not be indexed by the main and impurity phase reflections, which might be due to the complex local ordering of the sodium and/or transition metal atoms.

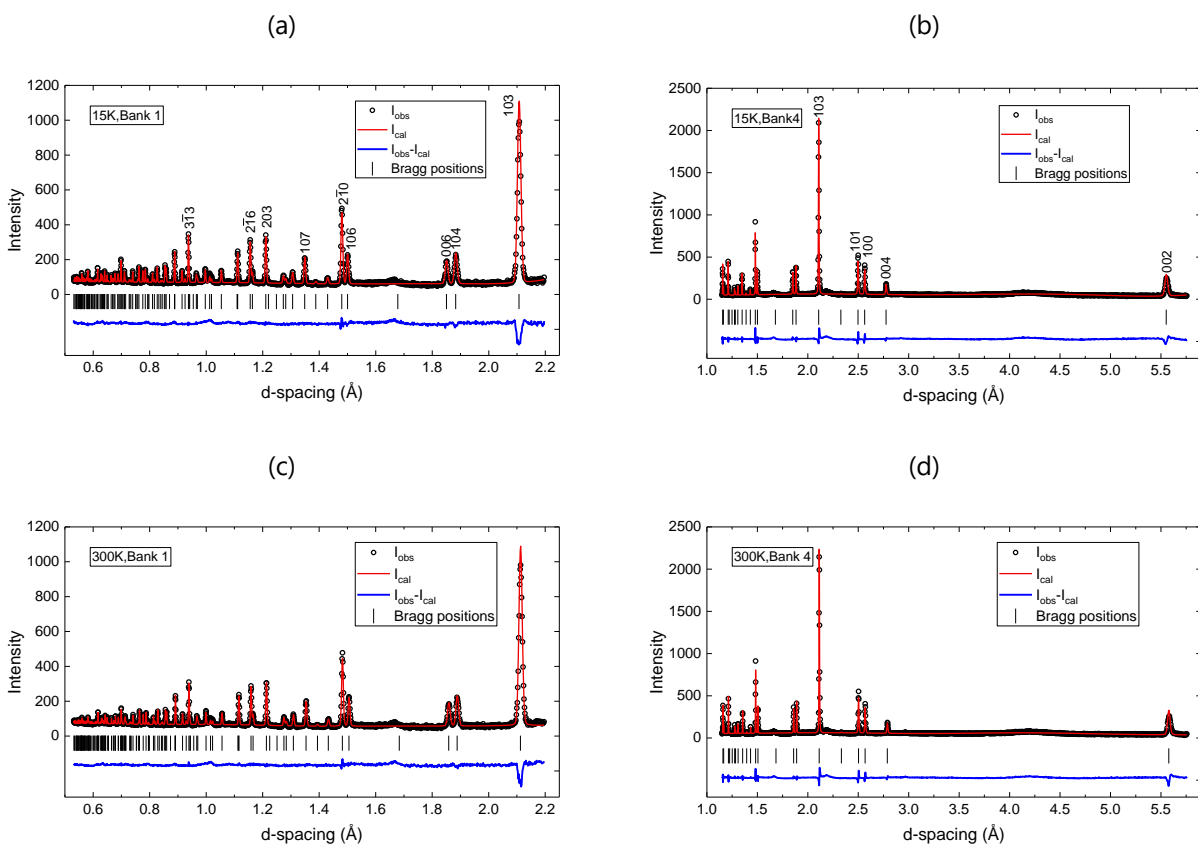


Figure 9: Rietveld refinement of $\text{Na}_{2/3}[\text{Ni}_{1/3}\text{Ti}_{2/3}]\text{O}_2$ powders characterized at 15K using detector bank 1 (a) and bank 4 (b), at 300K using bank 1 (c) and bank 4 (d).

Table 2 provides obtained structural information from Rietveld refinement of neutron diffraction datasets at different temperatures. Estimated lattice parameters are comparable with the previous XRD report on the same material¹⁰⁰. The powders show a tendency for higher occupancy of ‘2c’ sodium sites (edge-sharing or Na_e) compared to ‘2b’ sites (face-sharing or Na_f), i.e. 0.505 vs 0.162, which may be resulting from the energy penalty in occupying the ‘2b’ sodium sites (0, 0, 1/4) due to the repulsive interactions as they are positioned directly in-line with the transition metal ‘2a’ sites (0, 0, 0). At ambient temperatures (300 K), the higher thermal energy allows for slightly increased occupancy of the energetically unfavorable ‘2b’, i.e., 0.169 vs 0.162 at 15 K. The occupancy of face-sharing Na was 0.198 in the previous XRD study¹⁰⁰. Calculated thermal expansion coefficients between 15 and 300 K are: $\alpha_a=5.91\times 10^{-6} \text{ K}^{-1}$, $\alpha_c=1.57\times 10^{-5} \text{ K}^{-1}$. These coefficients are fairly positive and a large anisotropy is observed, typical of isostructural layered oxides such as P2-Na_xMnO₂¹⁷¹.

Table 2: Structural information of Na_{2/3}[Ni_{1/3}Ti_{2/3}]O₂ using Rietveld refinement of neutron diffraction datasets.

a. Temperature=15 K

| Element (Site) | x | y | z | Occupancy | U _{iso} (Å ²) | U ₁₁ (Å ²) | U ₃₃ (Å ²) |
|----------------------|--------|--------|-------------|-----------|------------------------------------|-----------------------------------|-----------------------------------|
| Na _f (2b) | 0 | 0 | 0.25 | 0.162(7) | - | 0.009(6) | 0.001(9) |
| Na _e (2c) | 0.3333 | 0.6667 | 0.25 | 0.505(7) | - | 0.018(2) | 0.009(3) |
| Ni (2a) | 0 | 0 | 0 | 0.3333 | 0.006(3) | - | - |
| Ti (2a) | 0 | 0 | 0 | 0.6667 | 0.015(5) | - | - |
| O (4f) | 0.6667 | 0.3333 | 0.09583(13) | 1 | - | 0.0067(4) | 0.0062(6) |

Lattice parameters: $a=b=2.9593\text{\AA}$, $c=11.1014\text{\AA}$; goodness of fit: $R_{wp}=9.30\%$.

Table 2 (cont'd)

b. Temperature=300 K

| Element (Site) | x | y | z | Occupancy | $U_{\text{iso}}(\text{\AA}^2)$ | $U_{11}(\text{\AA}^2)$ | $U_{33}(\text{\AA}^2)$ |
|----------------------|--------|--------|-------------|-----------|--------------------------------|------------------------|------------------------|
| Na _f (2b) | 0 | 0 | 0.25 | 0.169(8) | - | 0.022(8) | 0.004(10) |
| Na _e (2c) | 0.3333 | 0.6667 | 0.25 | 0.498(8) | - | 0.031(3) | 0.012(4) |
| Ni (2a) | 0 | 0 | 0.0 | 0.3333 | 0.009(3) | - | - |
| Ti (2a) | 0 | 0 | 0.0 | 0.6667 | 0.019(6) | - | - |
| O (4f) | 0.6667 | 0.3333 | 0.09523(15) | 1.0 | - | 0.0084(6) | 0.0088(8) |

Lattice parameters: $a=b=2.9643\text{\AA}$, $c=11.1510\text{\AA}$; goodness of fit: $R_{\text{wp}}=8.86\%$.

Table 2 can be visualized as nuclear density maps where the density of each species is shown as spheres (isotropic) or ellipsoids (anisotropic) in the left column in Figure 10 to Figure 13. For example, Figure 10(a) depicts the nuclear density map of Na in the refined structure at 15 K. For the shown isosurface level of 1\AA^{-3} , Na_e density spots appear larger than Na_f due to the higher fractional occupancy (Table 2a). In addition, sodium thermal ellipsoids also appear considerably oblate with the major axis along the ‘*ab*’ plane. The degree of oblateness is quantified using displacement ratio $\left(r = \sqrt{U_{33}/U_{11}} - 1 \right)$ which compares ‘in-plane’ (U_{11}) with the ‘out-of-plane’ (U_{33}) deviation. At 15 K, Na_e and Na_f atoms have negative ‘*r*’ values of -0.29 and -0.67, respectively, which are consistent with the oblate sodium ellipsoids. The lower ‘*r*’ value for Na_f is due to the repulsion from Ni and Ti atoms. These negative ‘*r*’ values are lower compared to other materials with layered structure like O3-NaCrO₂ ($r=-0.18$)¹⁷². The ‘in-plane’ repulsive interactions are lower in P2 than O3 phases due to the lower sodium content and hence the P2 phase displays more pronounced ‘in-plane’ deviations and oblateness. The transition metal atoms were taken to be isotropic for the reason discussed previously and hence appear as perfect spheres in Figure 11(a,

d) for Ni and in Figure 12(a, d) for Ti. We also allowed Ni and Ti to take different ADP parameters in order to yield positive ADP values. Oxygen atoms were refined anisotropically but they appear spherically in Figure 13(a, d) since $U_{11} \approx U_{33}$.

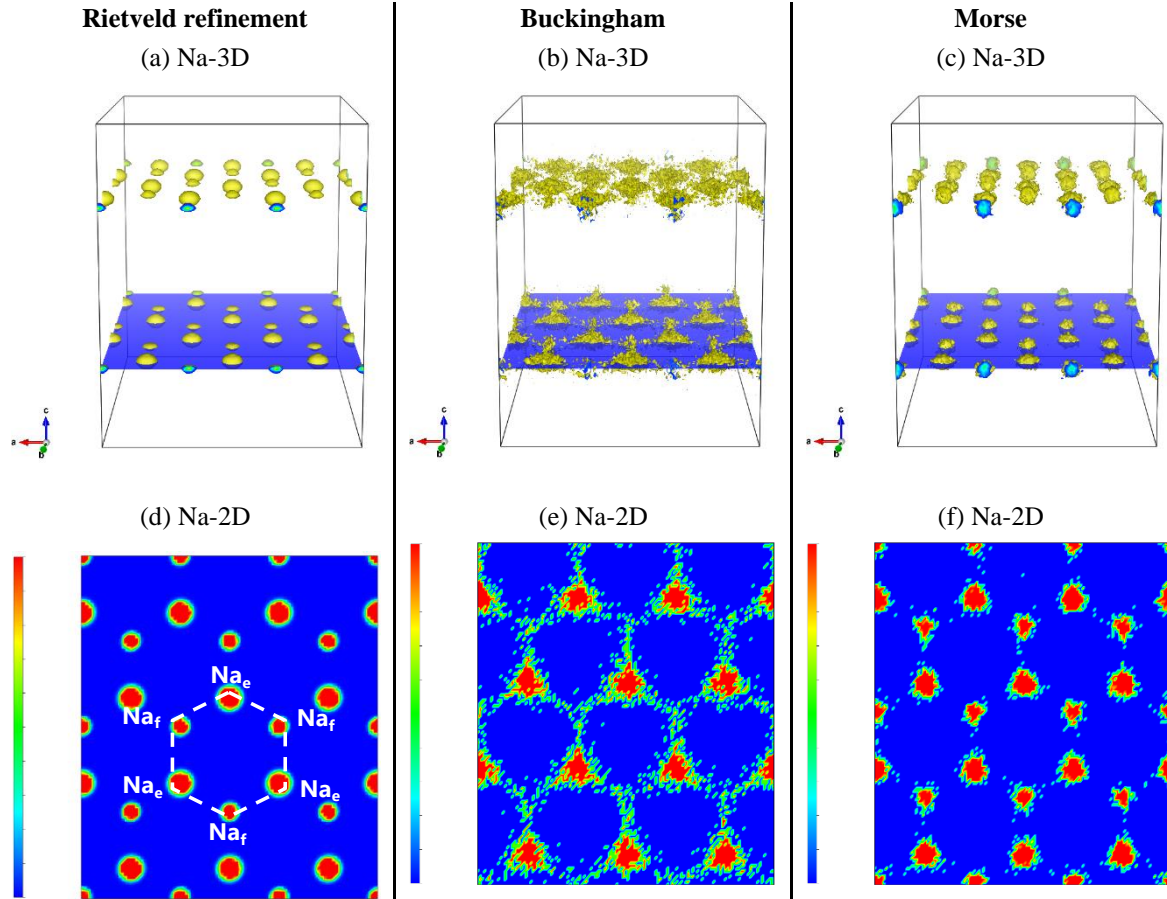


Figure 10: 3D nuclear density maps and 2D slices on the $\{001\}$ plane of Na. 3D isosurface level is 0.5 \AA^{-3} while 2D isosurface level is between 0 and 1 \AA^{-3} . Results from the Rietveld refinement at 15 K, Buckingham potential, and Morse potential are shown for each column.

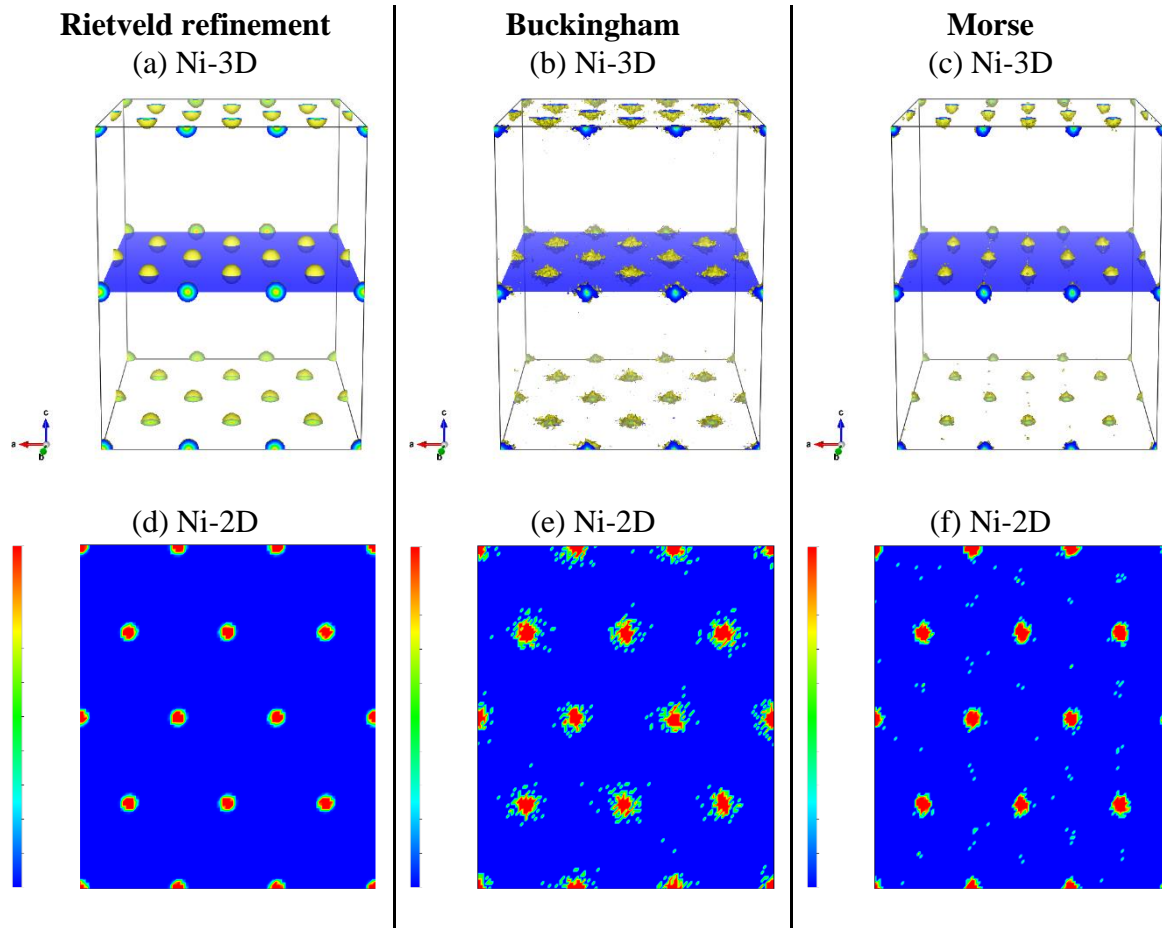


Figure 11: 3D nuclear density maps and 2D slices on the {001} plane of Ni. 3D isosurface level is 0.5 \AA^{-3} while 2D isosurface level is between 0 and 1 \AA^{-3} . Results from the Rietveld refinement at 15 K, Buckingham potential, and Morse potential are shown for each column.

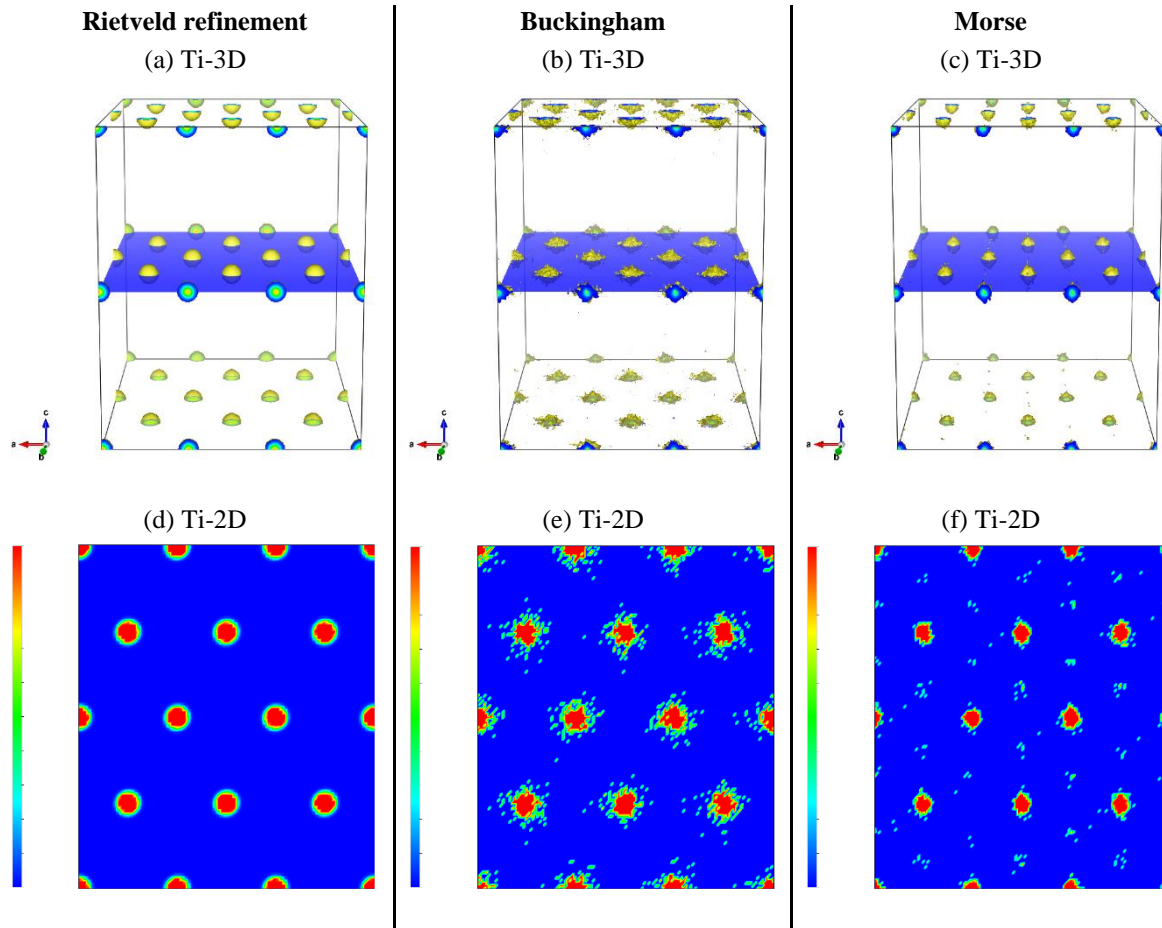


Figure 12: 3D nuclear density maps and 2D slices on the $\{001\}$ plane of Ti. 3D isosurface level is 0.5 \AA^{-3} while 2D isosurface level is between 0 and 1 \AA^{-3} . Results from the Rietveld refinement at 15 K, Buckingham potential, and Morse potential are shown for each column.

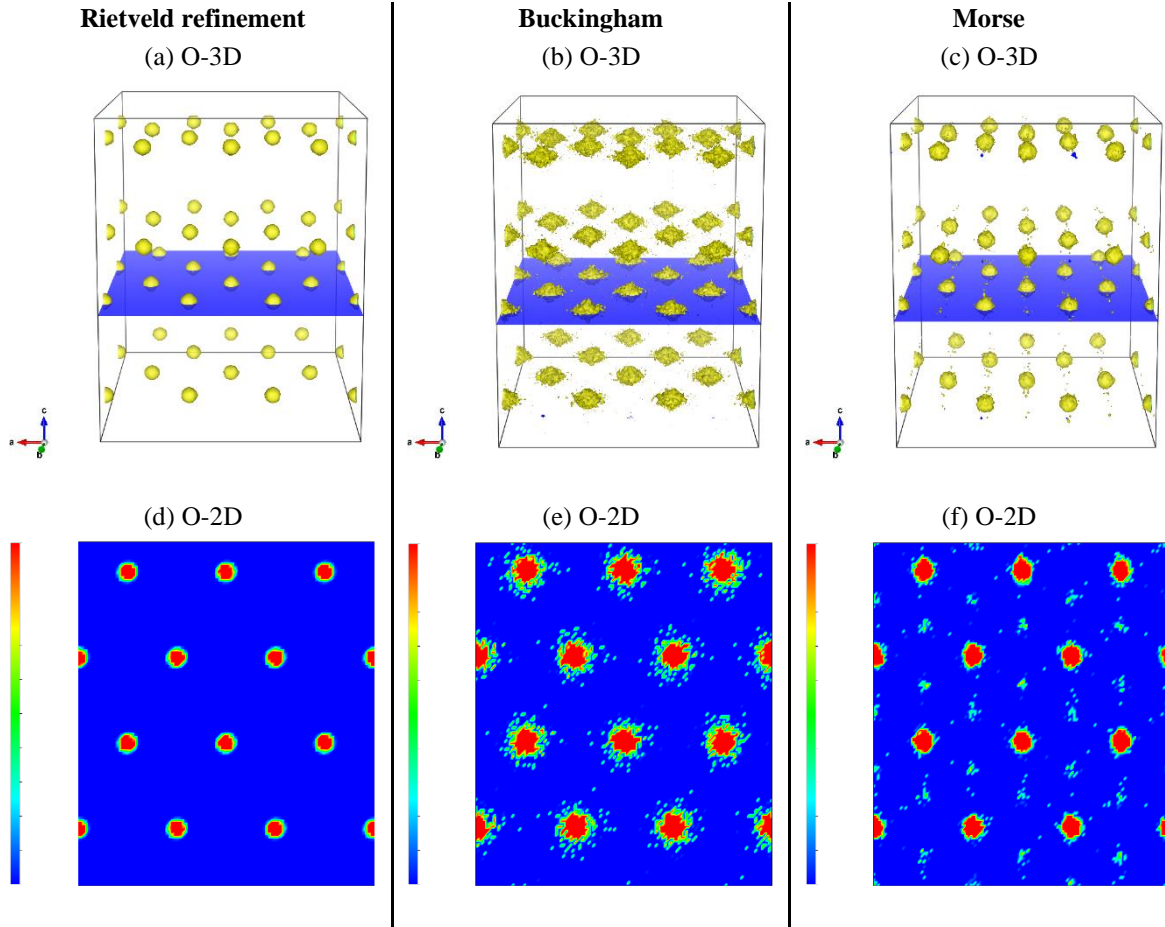


Figure 13: 3D nuclear density maps and 2D slices on the $\{001\}$ plane of O. 3D isosurface level is 0.5 \AA^{-3} while 2D isosurface level is between 0 and 1 \AA^{-3} . Results from the Rietveld refinement at 15 K, Buckingham potential, and Morse potential are shown for each column.

3.3 Energy minimization based on two interatomic potential models

The disordered distribution of Na_e/Na_f in the Na layers and Ni/Ti in the TM layers in Na_{2/3}[Ni_{1/3}Ti_{2/3}]O₂, which may affect Na dynamics, is critical for us to understand the local structure. We explored the energy landscape and investigated the overall energetics with the randomized supercells containing 24 formula units of Na_{2/3}[Ni_{1/3}Ti_{2/3}]O₂, with two NaO₆ trigonal prism layers and two NiO₆/TiO₆ octahedral layers. The equivalent orthorhombic supercell in space group Cmcm (#63) was constructed by converting the unit cell in the original space group P6₃/mmc (#194) through the following transformation matrix without any origin shift:

$$T = \begin{pmatrix} 3 & 2 & 0 \\ 0 & 4 & 0 \\ 0 & 0 & 1 \end{pmatrix}$$

The 16 sodium atoms in each supercell can be allocated equally or disproportionately to the two individual sodium layers, while still maintaining the overall composition. The presence of plentiful vacant sites in the sodium layer leads to a large number of possible configurations even for structures with equal sodium count between the layers. Likewise, the 24 transition metal atoms can be distributed equally or disproportionately while keeping the overall Ti:Ni ratio at 2:1. Using these randomized configurations, we explore the energy landscape and investigate the overall energetics using atomistic simulation. Since there are a large number of possible configurations for Na/vacancy and Ni/Ti distribution, 5000 randomized structures were sampled to yield statistically relevant results for four different scenarios based on Na/vacancy and Ni/Ti distribution in the two layers: Na equal and Ni equal, Na random and Ni equal, Na equal and Ni random, and Na random and Ni random.

The energy minimization for each configuration was performed in General Utility Lattice Program (GULP)¹⁷³ with the lattice parameters fixed. The long-range interactions were defined by Coulombic law, while two different types of potential models, Buckingham and Morse, as specified in Table 3, were used for the short-range interactions. For the Buckingham potential model, titanium and oxygen atoms were treated as polarizable and represented with the Dick-Overhauser core-shell approach while remaining atoms were treated as non-polarizable¹⁷⁴. The model parameters for Ti-O interactions were taken from a defect study of anatase¹³⁰, while the parameters for other interactions were derived in GULP to fit the experimentally obtained structure for P2-Na_{2/3}[Ni_{1/3}Ti_{2/3}]O₂ at 15 K. For the Morse potential model, the Morse function with a Lennard-Jones repulsive term added was used. The empirical Morse potential parameters were obtained from a self-consistent model for evaluating oxides and silicates¹³¹. Electronic polarization

effects were neglected in Morse potential. The short-range potential cutoff radius was set to be 10 Å for the Buckingham model and 12 Å for the Morse model.

Table 3: Interatomic potential parameters of the Buckingham model and Morse model.

a. Buckingham model

$$U^{Buckingham} = Ae^{-r/\rho} - Cr^{-6}$$

| Interactions | A (eV) | ρ (Å) | C (eV Å ⁶) |
|---------------------------------|-------------------------|------------|------------------------|
| Na-O | 1172.75 | 0.281 | 0.0 |
| Ni-O | 868.03 | 0.317 | 0.0 |
| Ti-O | 5111.70 | 0.2625 | 0 |
| O-O | 12420.50 | 0.2215 | 29.07 |
| Core-Shell Potential Parameters | | | |
| Species | k (eV Å ⁻²) | Y (e) | |
| Ti | 314 | -0.1 | |
| O | 31 | -2.8 | |

b. Morse model

$$U^{Morse} = D[(1 - e^{-a(r-r_0)})^2 - 1] + Ar^{-12}$$

| Morse Parameters | | | | | |
|------------------|----------------------|------------------------------------|--------------------|-------------------------|--|
| Interactions | D _{ij} (eV) | a _{ij} (Å ⁻²) | r ₀ (Å) | A (eV Å ¹²) | |
| Na-O | 0.0234 | 1.76 | 3.01 | 5.0 | |
| Ni-O | 0.0294 | 2.68 | 2.50 | 3.0 | |
| Ti-O | 0.0242 | 2.25 | 2.71 | 1.0 | |
| O-O | 0.0424 | 1.38 | 3.62 | 22.0 | |

We evaluated the validity of the atomistic potential models by examining their ability to reproduce experimental lattice parameters of a selected group of materials containing Na, Ni, Ti, and O, including NiO (cubic), TiO₂ (tetragonal), NiTiO₃ (rhombohedral), Na₂Ti₃O₇ (monoclinic) and Na₈Ti₁₆O₃₂ (monoclinic). The comparison of computed lattice parameters from both Buckingham and Morse potential sets and experimental values are shown in Table 4. The mean absolute errors employing Buckingham and Morse potential sets are 1.4 and 2.8%, respectively,

demonstrating the general validity of the studied pairwise atomic interactions and transferability across various structure polytypes, except for $\text{Na}_2\text{Ti}_3\text{O}_7$ and $\text{Na}_2\text{Ti}_6\text{O}_{13}$ in the Morse model. Good reproducibility of lattice parameters for $\text{Na}_{2/3}[\text{Ni}_{1/3}\text{Ti}_{2/3}]\text{O}_2$ at 15 K were confirmed by small deviations for both Buckingham ($\epsilon=0.08\%$) and Morse ($\epsilon=1.2\%$) model.

Table 4: Potential transferability across selected materials containing Na, Ni, Ti, and O. (The mean absolute errors of the Buckingham and Morse potentials are 1.4 and 2.8%, respectively).

| Buckingham | | | | | | | | | | |
|-------------------|-------|-------|------------------|-------|--------------------|--------|--|-------|---|--------|
| Lattice | NiO | | TiO ₂ | | NiTiO ₃ | | Na ₂ Ti ₃ O ₇ | | Na ₂ Ti ₆ O ₁₃ | |
| | Cubic | | Tetragonal | | Hexagonal | | Monoclinic | | Monoclinic | |
| | Expt. | Calc. | Expt. | Calc. | Expt. | Calc. | Expt. | Calc. | Expt. | Calc. |
| a (Å) | 4.178 | 4.173 | 4.594 | 4.428 | 5.032 | 5.090 | 9.133 | 9.186 | 15.131 | 15.296 |
| b (Å) | - | - | - | - | - | - | 3.806 | 3.717 | 3.745 | 3.698 |
| c (Å) | - | - | 2.959 | 3.068 | 13.792 | 13.766 | 8.566 | 8.612 | 9.159 | 9.098 |

| Morse | | | | | | | | | | |
|--------------|-------|-------|------------------|-------|--------------------|--------|--|-------|---|--------|
| Lattice | NiO | | TiO ₂ | | NiTiO ₃ | | Na ₂ Ti ₃ O ₇ | | Na ₂ Ti ₆ O ₁₃ | |
| | Cubic | | Tetragonal | | Hexagonal | | Monoclinic | | Monoclinic | |
| | Expt. | Calc. | Expt. | Calc. | Expt. | Calc. | Expt. | Calc. | Expt. | Calc. |
| a (Å) | 4.178 | 4.188 | 4.594 | 4.571 | 5.032 | 5.074 | 9.133 | 9.613 | 15.131 | 15.550 |
| b (Å) | - | - | - | - | - | - | 3.806 | 3.605 | 3.745 | 3.577 |
| c (Å) | - | - | 2.959 | 3.004 | 13.792 | 13.978 | 8.566 | 8.872 | 9.159 | 9.625 |

3.4 Energetics of Atomic Distribution and Ordering

Energy distribution histograms of optimized structures using two potential sets are shown in Figure 14. It was found that the distribution of sodium atoms and distribution of nickel and titanium atoms, i.e., four scenarios, have different effects on the energy distribution. The structures with random Ni/Ti distribution, Figure 14(c, d, g, h), exhibit two energy peaks with higher energy values while those with Ni/Ti equal distribution, Figure 14(a, b, e, f), exhibit just one energy peak with lower energy values. When taking a closer look at configurations corresponding to the two

energy peaks presented in the energy distribution histogram for equal sodium and random Ni/Ti distribution, Figure 14(c, g), it was found that the higher energy peak is associated to configurations with large deviation in the number of same type atoms per layer. These configurations tend to have 6 Ni atoms and 6 Ti atoms in one layer, and 2 Ni atoms and 10 Ti atoms in the other layer. The structures that contribute towards the low energy peak tend to have equal number of the same type atoms distributed in each layer (4 Ni atoms and 8 Ti atoms in each layer), i.e., similar to Figure 14(a, e). If we compare (a) and (b) or (e) and (f), we can see that random distribution of Na in two layers does not add extra energy peaks but leads to higher energy of the peak position. This trend suggests that the distribution of transition metal atoms plays a larger role in the overall energetics than sodium atoms and equal distribution of both sodium atoms and transition metal atoms provides the lowest energy values and hence the most favorable configurations. We further examined the in-plane distribution of Ni and Ti in these configurations and no Ni/Ti ordering was observed.

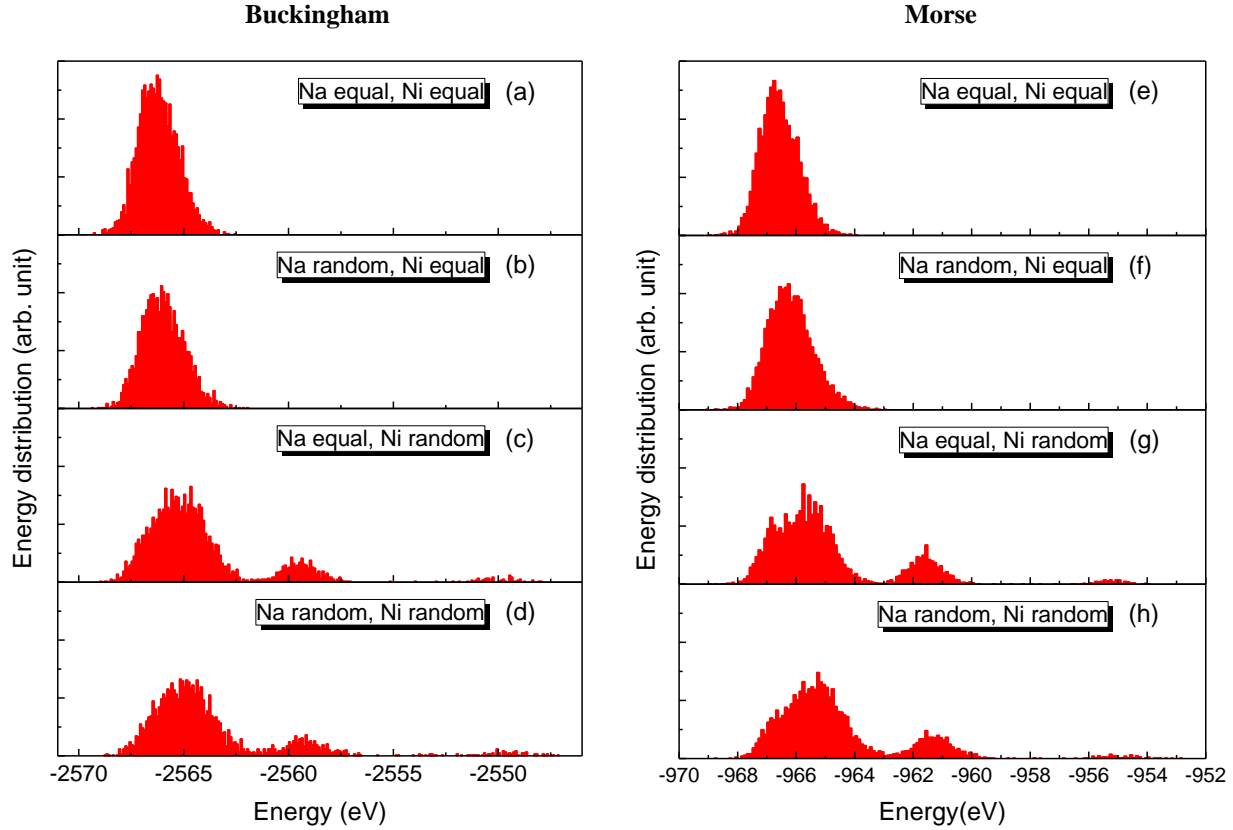


Figure 14: Energy distribution curve from the Buckingham and Morse potential for 3x2x1 supercells with four different scenarios of atom distribution: Na equal and Ni equal, Na random and Ni equal, Na equal and Ni random, and Na random and Ni random.

3.5 Simulated Average Structure

Atomic coordinates of optimized structures in Figure 14(a, e) were used to generate nuclear density maps for each individual species. After energy minimization, atomic coordinates were shifted to have one Ni or Ti atom at the origin to facilitate the comparison of different structures. The nuclear probability density maps were generated by calculating the probability of atomic distribution in individual pixels (resolution $\sim 0.1 \text{ \AA}$). 3D nuclear density maps and 2D slices were visualized using VESTA¹⁷⁵. This provides a graphical representation of the simulated average

structures. Because atomic densities in the two layers are similar, we only presented results for one of the layers.

As shown in Figure 10(b, c), sodium density spots obtained from atomistic simulation are compressed into oblate spheroids (major axis in the ‘*ab*’ plane) for both Buckingham and Morse potential models, which is consistent with the nuclear density map and negative sodium displacement ratio from the Rietveld refinement. The spheroidal elongation suggests that sodium gets thermally displaced in-plane and this might lead to the low diffusional activation energy. 2D isosurface sections are sliced along the {001} family to distinguish density spots between two sodium sites. For the Buckingham potential, most sodium clusters around edge-sharing sites, with the rest of sodium atoms distributed in the channels between edge- and face-sharing sites. On the other hand, sodium atoms from the Morse potential are localized at edge and face-sharing sites with higher concentration at edge sites, showing a close resemblance to the Rietveld analysis.

The transition metal (Ni/Ti) and O densities from atomistic simulation in Figure 11 to Figure 13 remain fairly spherical for both Buckingham and Morse potentials, although the distribution of atoms based on the Morse model is more concentrated. This suggests that the isotropic thermal displacement assumption in Rietveld analysis is reasonable. However, the 2D view along the {001} plane of Morse density maps also shows extra density spots that were not observed in experimental results, i.e. (f) of Figure 11 to Figure 13, suggesting possible gliding of Ni/TiO₆ layers. In these offset structures, one of the transition metal oxide layers glides along the *ab* plane, leading to the transition from P2 stacking to a O2 stacking, where the sodium atoms occupy octahedral sites. An example of this O2 structure is shown in Figure 15(b, c) from two different perspectives, while an example of the P2 structure is shown in Figure 15(a). Such P2-O2 phase transformations have been reported for other sodium transition metal oxides including

$\text{Na}_{2/3}[\text{Ni}_{1/3}\text{Mn}_{2/3}]\text{O}_2$ ¹⁷⁶ and $\text{Na}_{0.7}\text{Fe}_{0.4}\text{Mn}_{0.4}\text{Co}_{0.2}\text{O}_2$ ¹⁷⁷ during electrochemical insertion/extraction. On the other hand, O2 stacking was not observed in the simulated density maps based on the Buckingham potential. Energetics analysis of O2 structures from the Morse potential indicates that they also have a Gaussian distribution (e.g., Figure 14) with energy values comparable to normal structures (P2). As the O2 stacking does not add extra peaks to the diffraction pattern, the existence of O2 stacking is not able to be verified by the neutron diffraction results. Further studies are needed to better understand the possible static and dynamic features of the O2 stacking of this material.

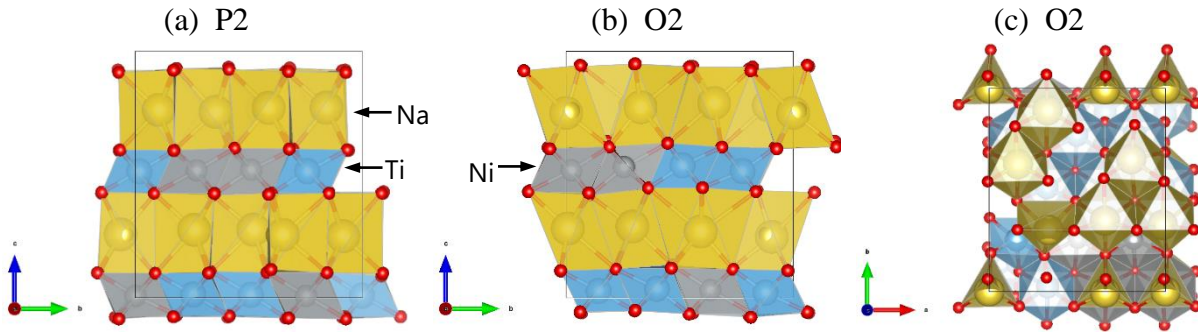


Figure 15: Example structures of (a) P2 and (b, c) O2 stacking for the supercell used in the atomistic simulation.

3.6 Conclusions

The average and local structural properties and energetics of atomic distribution in P2- $\text{Na}_{2/3}[\text{Ni}_{1/3}\text{Ti}_{2/3}]\text{O}_2$ were investigated using neutron diffraction and interatomic potential based atomistic simulations. The average crystal structure can be adequately described by a unit cell based on the $\text{P6}_3/\text{mmc}$ space group, in which face-sharing sites have lower occupancy compared with edge-sharing sites. In addition, refinement of anisotropic atomic displacement has revealed considerable oblateness in sodium motion along the ab plane, possibly caused by the repulsion from the transition metal oxide layer. Atomistic simulation based on the Buckingham and Morse

potential models suggest that it is energy favorable to have equal distributions of Na and transition metal in each of the two layers in the unit cell. While nuclear density maps from the Morse potential overall agree well with those from neutron diffraction, they also show signs of transition metal layer gliding that leads to O2 stacking.

CHAPTER 4 Structural and electronic properties change during cycling

4.1 Introduction

In this chapter, we focused on the structural and electronic properties of the layered P2-type $\text{Na}_x[\text{Ni}_{1/3}\text{Ti}_{2/3}]\text{O}_2$ using density functional theory. As Na ions are electrochemically inserted and extracted during the charge/discharge processes, the structural and electronic change of $\text{Na}_x[\text{Ni}_{1/3}\text{Ti}_{2/3}]\text{O}_2$ upon Na insertion and extraction were examined. The electronic conductivity, which is closely correlated to the battery performance, was also investigated in order to better our understanding of how to improve material performance in batteries.

4.2 DFT calculations

Considering the disordered distribution of Na_e/Na_f in the Na layers and Ni/Ti in the TM layers, the input configurations were determined based on the potential energy landscape analysis for a large number of randomized configurations explicated in CHAPTER 3. As it was found to be most energetically favorable to have equal Na ions in each Na layer and equal Ni ions in each TM layer in the unit cell¹⁷⁸, such equal Na/equal Ni distribution was applied in all simulation cells in this study. The most probable configurations from the energy distribution were selected as the representative structures for the DFT calculation. $3 \times 3 \times 1$ $\text{Na}_x[\text{Ni}_{1/3}\text{Ti}_{2/3}]\text{O}_2$ supercells containing 18 formula units with varying sodium contents ($x=0.33, 0.44, 0.56, 0.67, 0.78, 0.89$ and 1) were used as the input configuration. All DFT calculations were performed using the Vienna Ab initio Simulation Package (VASP)¹⁷⁹ within the projector augmented-wave (PAW) approach¹⁸⁰. The dispersion-corrected Perdew-Burke-Ernzerhof with Becke-Jonson damping (PBE-D3BJ) functional^{119,120} was used. To account for the electron localization of Ni ions, the Hubbard U correction was applied with $U_{\text{Ni}}=6.2$ eV¹⁸¹.

4.3 Structural changes upon Na extraction/insertion

To study the structural stability of $\text{Na}_x[\text{Ni}_{1/3}\text{Ti}_{2/3}]\text{O}_2$ during cycling, the structural evolution of $\text{Na}_x[\text{Ni}_{1/3}\text{Ti}_{2/3}]\text{O}_2$ upon sodium insertion and extraction was investigated by DFT-based MD simulations. The MD simulations were carried out at 300 K with the NPT ensemble for 3 ps with a time step of 1 fs. A plane-wave energy cut-off of 450 eV and single Γ point were used for the k-mesh. The lattice parameters of $\text{Na}_x[\text{Ni}_{1/3}\text{Ti}_{2/3}]\text{O}_2$ at 300 K obtained from DFT-based MD calculations were plotted with varying sodium content x as in Figure 16. The error bars indicate the fluctuation (standard deviation) of lattice parameters during MD simulation, which is primarily determined by the cell size. An expansion along a axis and a contraction of c were observed upon sodium insertion from the pristine state, exhibiting the same trend with previous in-situ XRD study¹⁸². The expansion of ab plane is probably due to the increase of the total number of Na ions within the layer leading to repulsion between the Na ions, while the decrease of c can be attributed to the increasing Coulomb attraction between the layers resulting from increasing sodium ions. The structural changes introduced by Na extraction from the pristine state are relatively small. For both a and c direction, lattice constants stay at a stable value with small fluctuations, which might be related to the balance of Coulomb forces due to the decrease of Na ions and increase of TM charges. While a possible P2 to O2 phase transition was observed in our previous ex situ XRD study⁹⁸ when x in $\text{Na}_x[\text{Ni}_{1/3}\text{Ti}_{2/3}]\text{O}_2$ drops below 1/3, such transition was not found in the x range of 1/3~1 either in that experimental study or in this work. With no phase transition and a relatively small lattice constant change leading to a volume change less than 2% observed in the studied Na content range, we expect a small possibility of structure collapse and an overall good structural stability of the material in the Na content range of 1/3 to 1, as confirmed by experiments⁹⁸.

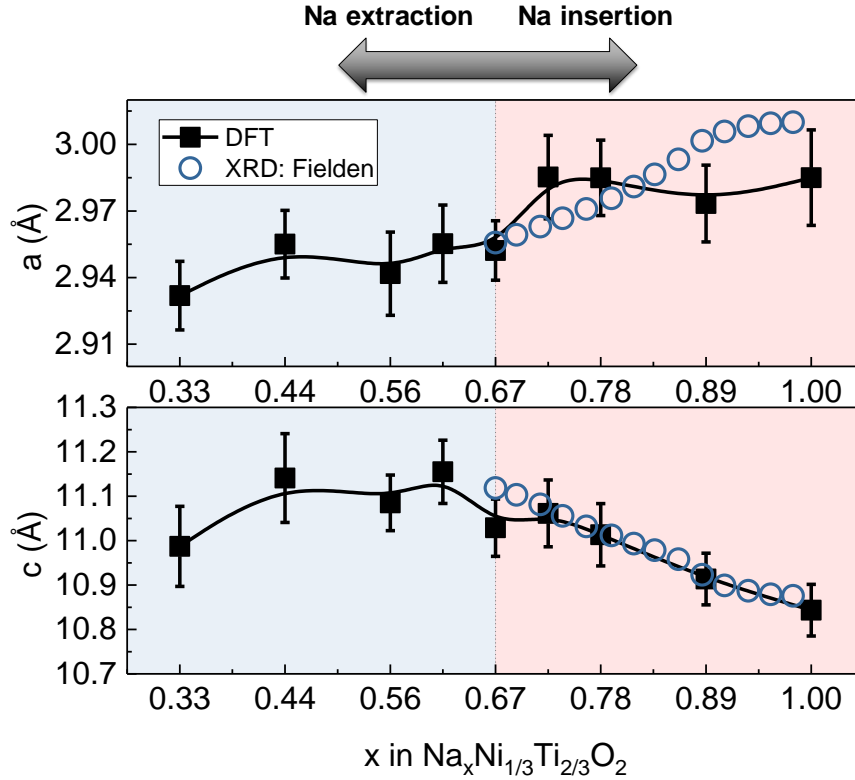


Figure 16: Calculated lattice parameters of P2-Na_x[Ni_{1/3}Ti_{2/3}]O₂ vs. sodium content x (black squares), compared to an XRD study by Fielden et al.¹⁸²

For further analysis of the structural change with respect to x, especially for the sodium extraction region, the TM-O bond lengths of the average structure for each composition were calculated. The local Jahn-Teller (JT) distortion of TM-centered octahedra can be identified from the unequal distribution of six TM-O bond lengths (two longer bonds and four shorter bonds), which provides information on the oxidation state of the TM ions. It was found that none of the Ti ions are JT active in any of the compositions we studied, while in some compositions, some of the Ni ions are JT active with two longer Ni-O bonds around 2.4 Å and four shorter bonds around 1.9 Å. Figure 17(a) presents the distribution of the four shortest Ni-O bonds (red circles) and the two longest Ni-O bonds (blue diamonds) connected to each Ni. For the pristine and sodium-rich material (x ≥ 0.67), bond lengths for the four shortest Ni-O bonds and two longest Ni-O bonds of

each Ni atom are well separated, indicating all Ni ions are JT active with one example shown in Figure 17(c). With Na ions extracted from the pristine state, some of the Ni ions become JT inactive with an example shown in Figure 17(b), with the bond lengths of two longest Ni-O overlapping with four shortest bonds in Figure 17(a). The decrease of JT distortion upon Na extraction can be an indication of the redox change of the Ni ions, as also observed in LiNiO₂ during lithium deintercalation by X-ray absorption fine structure (XAFS)¹⁸³. Such JT transition adds the complexity of overall lattice change when Na ions being extracted, providing a possible reason for the plateau of lattice parameters upon Na extraction. When furtherly examining the local environment of the Ni atoms that undergo such JT transition, we did not find a direct correlation between the positions of these Ni ions and either the positions of removed Na or the local Ni/Ti ordering. Considering the dynamics of the system, the JT transition of Ni was mostly likely to be affected by the global structural fluctuations, rather than the local environment.

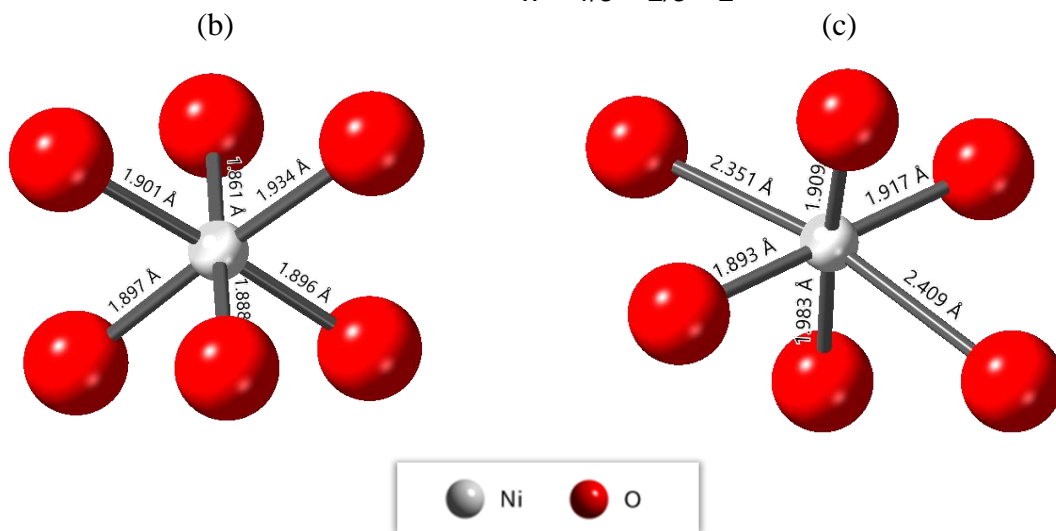
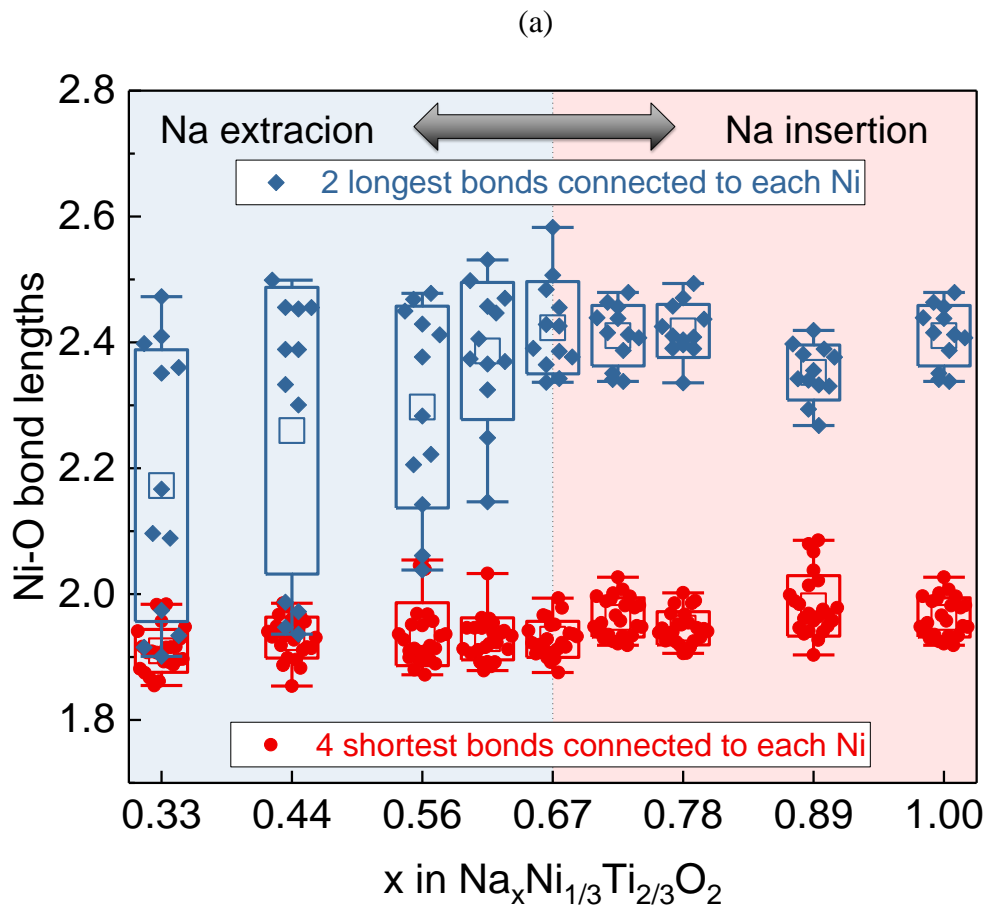


Figure 17: (a) The distribution of Ni-O bond lengths (b) an example of a JT-inactive Ni ion (c) an example of a JT-active Ni ion.

4.4 Electron density distribution and the atomic charge

To study the local electron distribution change and redox reactions that occurred during cycling, the electron density distribution and atomic charge for different sodium content in $\text{P2-Na}_x[\text{Ni}_{1/3}\text{Ti}_{2/3}]\text{O}_2$ were studied using DFT. The configuration for DFT calculation is the average structure obtained from MD. A plane-wave energy cut-off of 450 eV and a Gamma-centered k-mesh ($6\times 6\times 6$) were used for electronic structure calculations. To visualize the electron transfer involved in the redox reactions during Na insertion and extraction, the electron density difference between the pristine cell and the cell upon Na insertion and extraction are calculated by DFT and plotted using VESTA¹⁷⁵ as in Figure 18 with an isosurface level of 0.005 \AA^{-3} . While the significant electron density change around the inserted/extracted Na ion is directly correlated to the insertion or extraction of Na, the electron change around the surrounding TM ions provides information on the redox reaction occurring upon Na insertion/extraction. The electron density around Ni decreased as one Na ion was extracted (Figure 18(a)), indicating the oxidation of Ni. No noticeable electron density change was found around the Ti ions, implying that the Ti ions are not active in the redox reactions during Na extraction. Similarly, the electron gain around Ti ions (Figure 18(b)) indicates the reduction of Ti upon Na insertion, where the Ni ions are electrochemically inactive. It is worth mentioning that the surrounding O ions bonded to the Na ion also lose and gain electrons upon Na extraction and insertion, respectively, suggesting the participation of O in the redox reactions, which have also been observed in similar materials $\text{P2-Na}_x[\text{Ni}_{1/3}\text{Mn}_{2/3}]\text{O}_2$ ¹⁸⁴ and $\text{P2-Na}_{2/3}[\text{Mn}_{1/3}\text{Co}_{2/3}]\text{O}_2$ ¹⁸⁵.

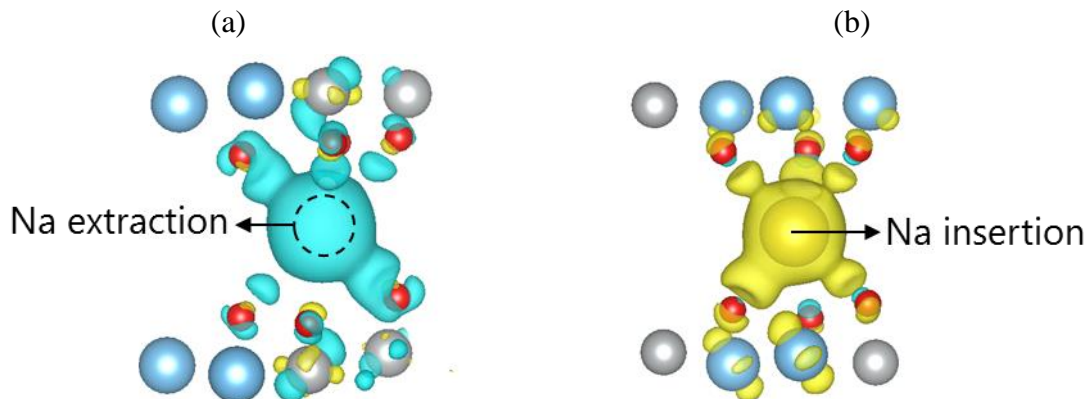


Figure 18: Electron density difference (positive in yellow and negative in cyan) upon (a) Na insertion, (b) Na extraction. The isosurface level is 0.005 \AA^{-3} . The Na, Ni, Ti and O atoms are represented by yellow, gray, blue and red spheres, respectively.

The redox processes during Na extraction/insertion could be associated with the change of atomic charges. The common charge models to assign electron densities to each atom include Density Derived Electrostatic and Chemical (DDEC) charges¹²¹, Bader charges¹²², Hirshfeld charges¹²³, and Mulliken charges¹²⁴. Considering that the Hirshfeld charge model tends to underestimate the charge^{125,126} and the Mulliken charge model is sensitive to the basis sets^{127,128}, we only applied the DDEC6 and Bader models to calculate the atomic charge in this study.

Figure 19(a) shows the distribution of calculated atomic charges of each atom for different compositions as well as the average atomic charges for each type of atom. The DDEC and Bader results gave the same trends for the atomic charge. During Na insertion and extraction, the charge of Na ions stays at a stable value around 1. For transition metal ions, Ni and Ti act differently upon Na insertion and extraction. With Na ions inserted, the charge of Ti ions decreased while the charge of Ni maintained at the same level. On the contrary, the charge of Ti ions stayed flat and the charge of some Ni ions increased, corresponding to the Jahn-Teller transition of Ni discussed before. The trend of the atomic charge confirms that the Ni is redox active during Na extraction and Ti is redox

active during Na insertion, consistent with what we observed from electron density distribution. The increasing O charge with increasing x provides another evidence that the oxygen ions are also involved in the redox reactions, also consistent with the observed electron density change around O.

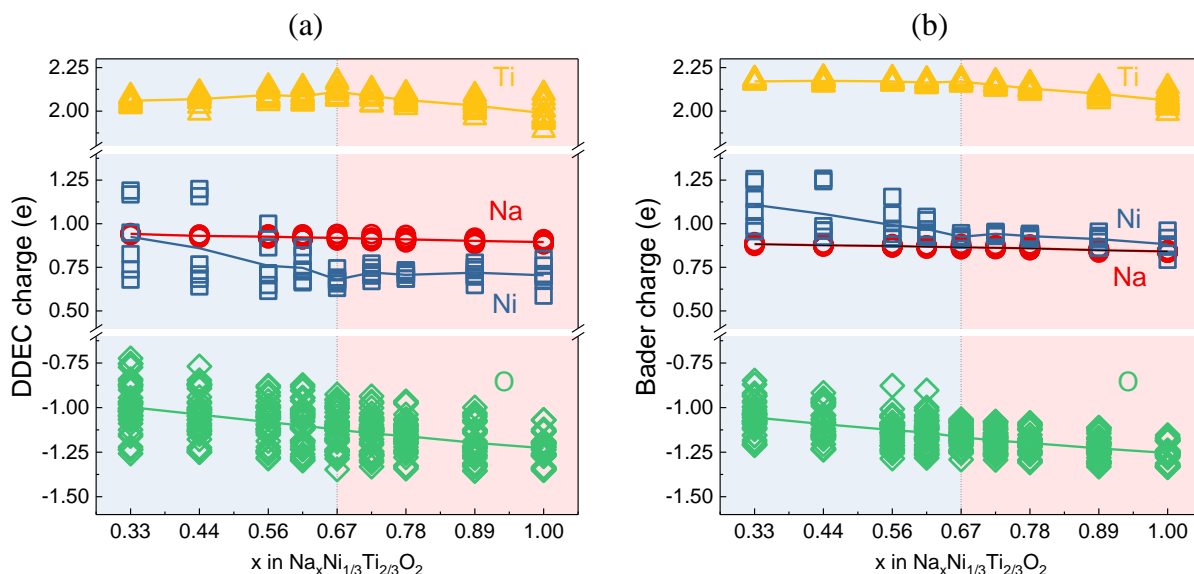


Figure 19: The atomic charge distribution for each atom at different sodium content x in $\text{Na}_x[\text{Ni}_{1/3}\text{Ti}_{2/3}]\text{O}_2$ based on (a) DDEC model; (b) Bader model.

4.5 Density of states

To gain a further understanding of the change of electronic structures during cycling, the density of states (DOS) of $\text{Na}_x[\text{Ni}_{1/3}\text{Ti}_{2/3}]\text{O}_2$ with different sodium contents ($x=0.44, 0.67, 0.89$) was calculated. The total DOS, as well as the partial DOS for Na, d-orbitals of Ni and Ti, and p-orbital for O, are presented in Figure 20.

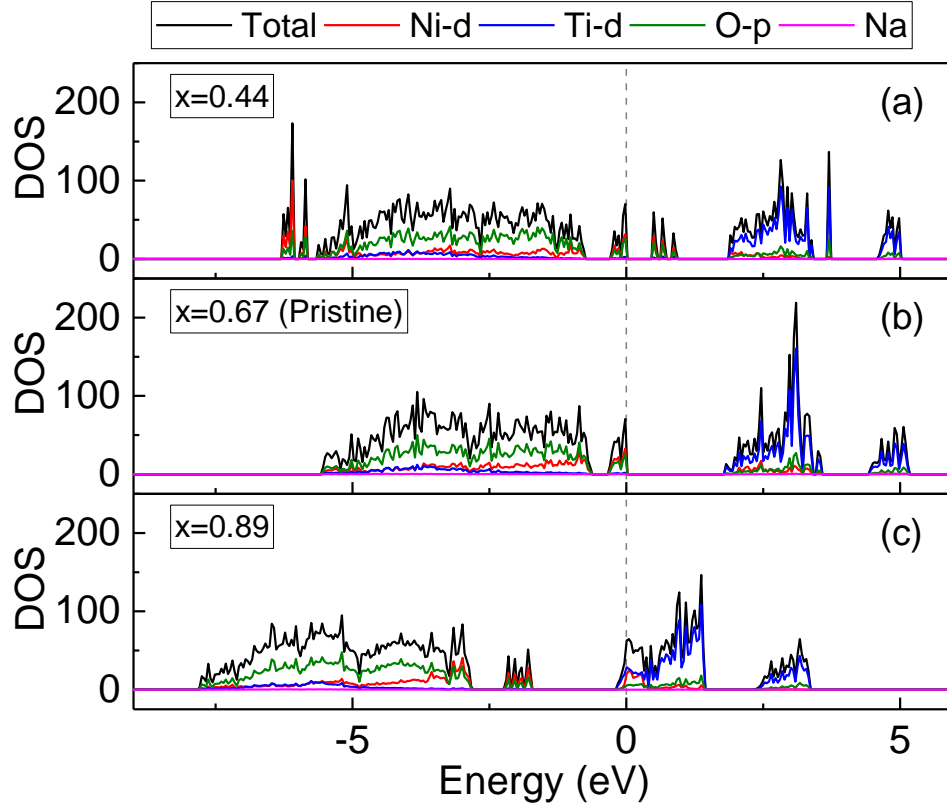


Figure 20: The density of states of $\text{Na}_x[\text{Ni}_{1/3}\text{Ti}_{2/3}]\text{O}_2$ with (a) $x=0.44$, (b) $x=0.67$, (c) $x=0.89$. The Fermi energy is set to be zero.

When Na is extracted from the pristine state, e.g., from $x=0.67$ (Figure 20(b)) to $x=0.44$ (Figure 20(a)), the mixed Ni-d and O-p band at the top of the valence band split into two bands with one fully occupied and the other unoccupied. The unoccupied Ni/O band suggests partial electron loss, i.e., oxidation of Ni and O upon Na extraction. An insignificant change of Ti-d band was found from $x=0.67$ to $x=0.44$, suggesting that the Na extraction had less influence on Ti oxidation state. In the meanwhile, the split band leads to a smaller bandgap compared to the pristine material.

When Na is inserted from the pristine state, e.g., from $x=0.67$ (Figure 20(b)) to $x=0.89$ (Figure 20(c)), the Fermi level moved toward the higher energy end, leading to a partially occupied Ti-d band. The partial occupancy of the Ti-d band indicates the electron gaining of Ti, consistent

with the reduction of Ti during Na insertion. The main Ni bands stayed fully filled before and after Na insertion, suggesting that the Ni ions are inactive in the redox reactions during Na insertion.

4.6 Electronic conductivity

As high electronic conductivity is desired for electrode materials, we calculated the electronic conductivity for different compositions using two approaches based on the electronic structure calculated from DFT.

4.6.1 Electronic conductivity from the Kubo-Greenwood approach

DFT calculations were carried out with a plane-wave energy cut-off of 450 eV and a Gamma-centered k-mesh (6×6×6). The electronic conductivities were derived from the frequency-dependent complex dielectric function based on the Kubo-Greenwood approach^{186,187}.

Based on the Kubo-Greenwood formula, the transverse conductivity $\sigma_{\perp}(\mathbf{q}, \omega)$ is related to the transverse component of the dielectric function $\epsilon_{\perp r}(\mathbf{q}, \omega)$ by:

$$\epsilon_{\perp r}(\mathbf{q}, \omega) = 1 + \frac{i}{\epsilon_0 \omega} \sigma_{\perp}(\mathbf{q}, \omega) \quad \text{Eq. 29}$$

where \mathbf{q} and ω are the wave vector and frequency, respectively. Thus, with $\mathbf{q} \rightarrow 0$ the electronic conductivity σ_e is related to the imaginary part of dielectric function ϵ_2 as $\sigma_e(\omega) = \omega \epsilon_2(\omega)$. The DC electronic conductivity was obtained by the extrapolation of σ_e as $\omega \rightarrow 0$.

The obtained electronic conductivities of P2-Na_x[Ni_{1/3}Ti_{2/3}]O₂ at different x were plotted in Figure 21. At all compositions, the electronic conductivities for the Cartesian xx and yy direction are similar, both higher than along the zz direction, suggesting electron conduction in P2-Na_x[Ni_{1/3}Ti_{2/3}]O₂ is mainly two-dimensional along the *ab* plane. The electronic conductivities in all directions increased when either inserting and removing Na atoms, which may be due to the increasing electron delocalization during atom oxidation and reduction processes.

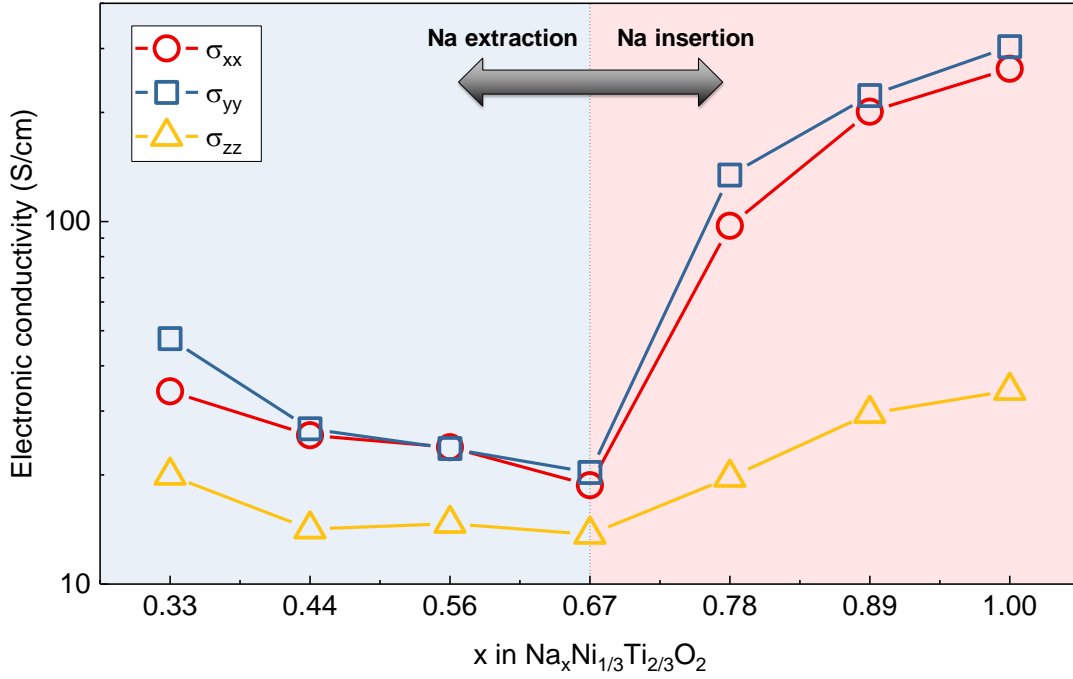


Figure 21: The electronic conductivity of $\text{Na}_x[\text{Ni}_{1/3}\text{Ti}_{2/3}]\text{O}_2$ at different x from the Kubo-Greenwood approach

4.6.2 Electronic conductivity from the Boltzmann transport equations

To account for the dynamics in the material, 50 input structures were randomly selected from the MD trajectory for each composition to calculate the electronic conductivity. The DFT electronic structure calculations were conducted for each configuration with a cut-off energy of 450 eV and a Gamma-centered k-mesh of $4 \times 4 \times 3$. The electrical conductivities were calculated using maximally localized Wannier functions as basis functions with the BoltzWann module¹² in the Wannier90 package² based on the semiclassical Boltzmann transport equations. The current density \mathbf{J} and the electronic heat current \mathbf{J}_Q is related to the conductivity σ as Eq. 30 and Eq. 31 respectively:

$$\mathbf{J} = \sigma(\mathbf{E} - S\nabla T) \quad \text{Eq. 30}$$

$$J_Q = T\sigma SE - K\nabla T, \quad \text{Eq. 31}$$

where \mathbf{E} is the electric field; \mathbf{S} is the Seebeck coefficient; ∇T is the temperature gradient. \mathbf{K} is related to the thermal conductivity according to $\kappa = \mathbf{K} - T\sigma\mathbf{S}^2$. The conductivity depending on chemical potential μ and temperature T can be derived as:

$$[\sigma]_{ij}(\mu, T) = e^2 \int_{-\infty}^{+\infty} dE \left(-\frac{\partial f(E, \mu, T)}{\partial E} \right) \Sigma_{ij}(E) \quad \text{Eq. 32}$$

where $f(\varepsilon, \mu, T)$ is the Fermi-Dirac distribution function as Eq. 33 and $\Sigma_{ij}(E)$ expressed as Eq. 34:

$$f(\varepsilon, \mu, T) = \frac{1}{e^{(\varepsilon-\mu)/k_B T} + 1} \quad \text{Eq. 33}$$

$$\Sigma_{ij}(E) = \frac{1}{V} \sum_{n,k} v_i(n, k) v_j(n, k) \tau_{nk} \delta(E - E_{n,k}) \quad \text{Eq. 34}$$

where τ_{nk} is the relaxation time for the electron on band n at wave vector, v and E the velocity and energy respectively, V the volume. The relaxation time was approximated as a constant value of 10 fs for all electrons.

Figure 22 shows the calculated electronic conductivity in three directions along the Cartesian x , y , and z for three different compositions. Each data point represents the value calculated from one individual structure, while the box gives the standard deviation of the data. The numbers in the plot label the average calculated electronic conductivities for all configurations of a composition. Despite the limitation of the DFT+U method in choosing the semi-empirical U values, the electronic structure calculations still provide valuable insights in the Na concentration dependence of the electronic conductivity of this material.

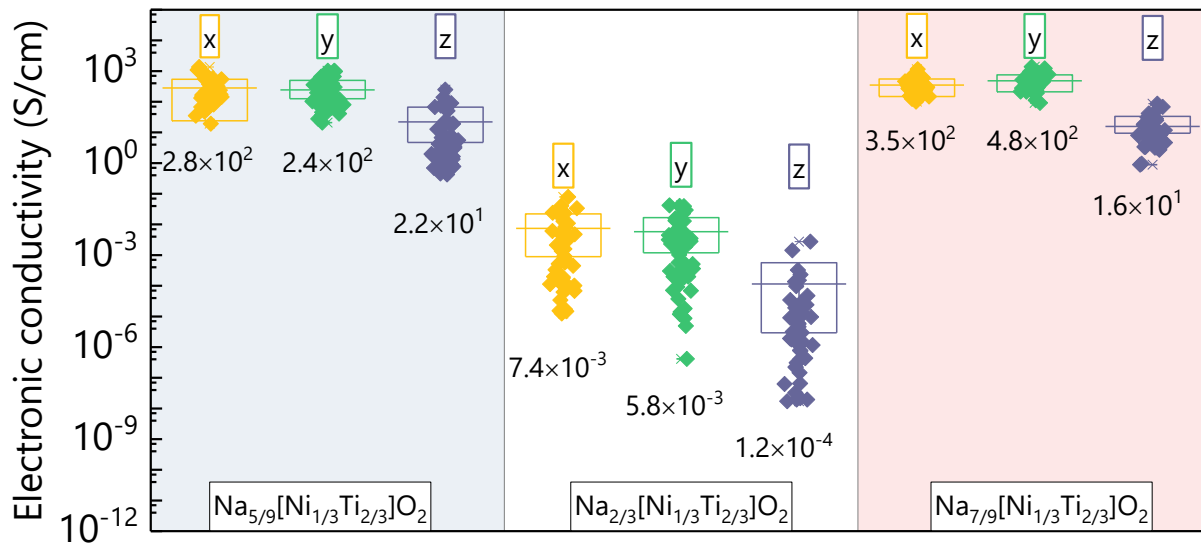


Figure 22: The electrical conductivity of $\text{Na}_x[\text{Ni}_{1/3}\text{Ti}_{2/3}]\text{O}_2$ at different x . The left, middle, and right panel represents results for $\text{Na}_{5/9}[\text{Ni}_{1/3}\text{Ti}_{2/3}]\text{O}_2$, $\text{Na}_{2/3}[\text{Ni}_{1/3}\text{Ti}_{2/3}]\text{O}_2$, $\text{Na}_{7/9}[\text{Ni}_{1/3}\text{Ti}_{2/3}]\text{O}_2$, respectively. Yellow, green, and purple points represent the calculated electrical conductivity along x , y , and z direction, respectively.

It is clear that electronic conductivity is sensitive to atomic structure as its value varies significantly, by orders of magnitude, for different configurations. For all compositions, electronic conductivities observed along the Cartesian x and y directions are about one order's magnitude higher than that along the z (i.e. crystallographic c) direction, suggesting the mainly two-dimensional electron conduction. However, the electronic conductivity along the z direction (e.g. ~ 10 S/cm) of Na-rich and deficient phases is not negligible, unlike the case of ionic conductivity. There is a significant increase (about 5 order's magnitude) in the electronic conductivity when sodium content is decreased or increased from the pristine phase by 16.7% (i.e. from $x=2/3$ to $x=5/9$ and from $x=2/3$ to $x=7/9$). This trend is consistent with the above results using a single configuration calculation based on the Kubo-Greenwood approach. This significant increase of electronic conductivity is not surprising as the pristine phase of $\text{Na}_{2/3}[\text{Ni}_{1/3}\text{Ti}_{2/3}]\text{O}_2$ contains

nominally Ni^{2+} and Ti^{4+} , while decrease or increase of Na content will activate $\text{Ni}^{2+}/\text{Ni}^{3+}$ or $\text{Ti}^{4+}/\text{Ti}^{3+}$ redox couple, respectively.

4.7 Conclusions

In this chapter, we studied the structural and electronic properties of P2-type $\text{Na}_x[\text{Ni}_{1/3}\text{Ti}_{2/3}]\text{O}_2$ during electrochemical oxidation/reduction using DFT calculations. For structural evolutions during electrochemical processes, it was found that the insertion of sodium leads to expansion of the *ab* plane and contraction of *c* axis. On the other hand, the extraction of sodium brings in a small structural change, which might be related to the JT active to JT inactive transition for Ni ions during Na extraction.

Electronic properties including the electron density distribution, the atomic charge, and density of states were analyzed, all leading to the same conclusion that Ni and Ti are the major redox-active ion during Na extraction and insertion, respectively, with O also participating in the redox reaction all the way.

To assess the electrochemical performance of P2-type $\text{Na}_x[\text{Ni}_{1/3}\text{Ti}_{2/3}]\text{O}_2$, we examined the electronic conductivity of the material using two approaches based on the electronic structure calculated from DFT, Kubo-Greenwood approach and Boltzmann transport equations. Both approaches showed similar results that the dominant electronic conduction occurs within the 2D layers along *ab* plane and an increase of electronic conductivity can be resulted from both inserting and extracting Na ions. From the results based on Boltzmann transport equations, the pristine $\text{Na}_{2/3}[\text{Ni}_{1/3}\text{Ti}_{2/3}]\text{O}_2$ showed an electronic conductivity of $\sim 10^{-3}$ S/cm, of which a significant increase can be achieved by either removing or inserting Na ions. Removing or inserting 16.7% of the Na can lead to an increase in the electronic conductivity of 5 orders. Such an improved understanding

of structural and electronic properties could be utilized to optimize materials and devices for better battery performance.

CHAPTER 5 Dynamic properties of P2- $\text{Na}_{2/3}[\text{Ni}_{1/3}\text{Ti}_{2/3}]\text{O}_2$

5.1 Introduction

To assess the rate performance of P2-type layered material $\text{Na}_{2/3}[\text{Ni}_{1/3}\text{Ti}_{2/3}]\text{O}_2$, we investigated the diffusion mechanism as well as ionic conductivity with a combination of experimental and computational techniques. The quasi-elastic neutron scattering (QENS) experiments and molecular dynamics (MD) simulations based on interatomic potential (IP) and density functional theory (DFT) were performed to identify the diffusion mechanism.

5.2 Self-diffusion of Na ions from QENS

QENS experiments were conducted using the time-of-flight backscattering spectrometer (BASIS)¹⁸⁸ at the Oak Ridge National Laboratory (ORNL). The sample $\text{Na}_{2/3}[\text{Ni}_{1/3}\text{Ti}_{2/3}]\text{O}_2$ powders were synthesized by solid-state reactions, heated to 200 °C for 10 hours, and then stored in an argon atmosphere to limit the exposure to moisture. The measurements were performed from 450 to 700 K to study the Na ion dynamics and at 30 K for the instrument resolution function. The data were normalized by the Vanadium measurement and reduced in the Mantid package¹⁸⁹, with the energy transfer (E) range of ± 100 μeV (0.4 μeV binning) and momentum transfer (Q) range of 0.3 to 1.9 \AA^{-1} (0.2 \AA^{-1} binning). The QENS spectra at each Q , with a convolution of the resolution function, were fitted with a combination of one delta function (for the elastic peak), a Lorentzian peak (for the quasi-elastic features), and a flat background using the DAVE package¹⁹⁰.

In QENS experiments, the quasi-elastic broadening of spectra was the direct evidence of diffusive motions, as shown in the measured QENS spectra $S(Q, E)$ for $Q=0.3$ \AA^{-1} , i.e., Figure 23. The inset plot in Figure 23 shows the increased QENS broadening with increasing temperature, suggesting enhanced diffusion at higher temperatures.

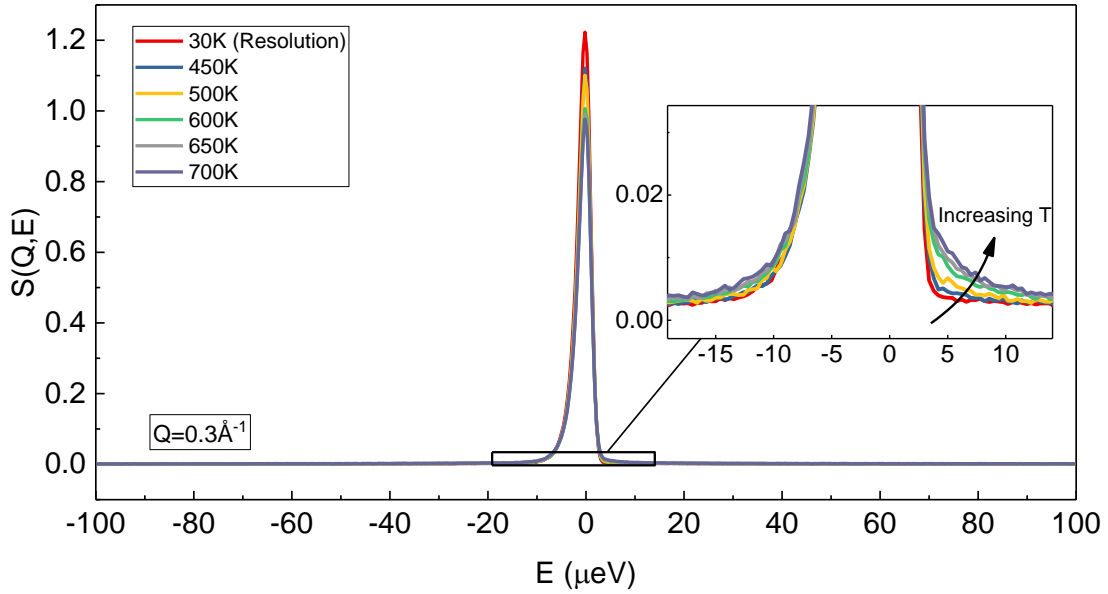


Figure 23: Experimental QENS spectra $S(Q,E)$ for various temperatures at $Q=0.3 \text{ \AA}^{-1}$.

The quantitative analysis of spectra was conducted to further understand the Na diffusion behaviors in the sample. The measured QENS data at each temperature and each Q , was fitted with a combination of a flat background, one delta function for the elastic peak and a Lorentzian peak for the quasi-elastic features, convoluted with the resolution function. An example for 700 K and $Q=0.3 \text{ \AA}^{-1}$ shows the fit and residuals in Figure 24(a). The Q -dependence of half-width-half-maximum (HWHM or Γ) of the Lorentzian peak characterizes the diffusive motions of Na. Figure 24(b) shows an example of Γ against Q at 700 K.

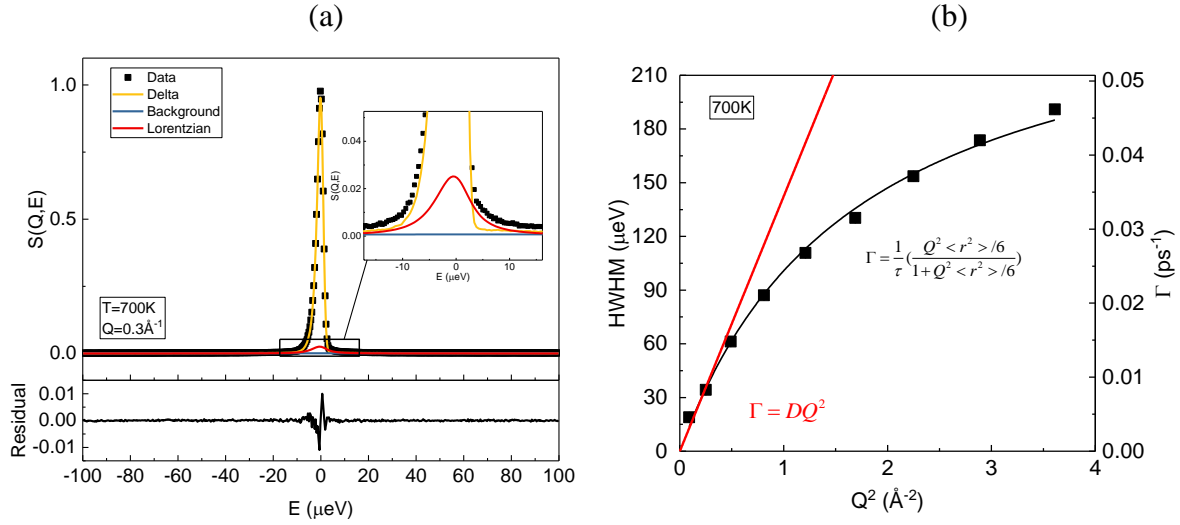


Figure 24: (a) Fit of the QENS spectra at 700 K and $Q=0.3 \text{ \AA}^{-1}$. (b) The HWHM of the Lorentzian function at 700 K as a function of Q^2 , fitted to the Fickian model at small Q (red line) and the SS model (black line).

In the low- Q region, a linear relationship between Γ and Q^2 indicates continuous translational diffusion of Na ions following Fick's law at large distances. The Fick's model describes the long-range dynamics. The Fickian diffusivity D was calculated according to $\Gamma(Q) = DQ^2$ in $Q \leq 0.5 \text{ \AA}^{-1}$ range, as the slope of the red line in Figure 24(b). The Fickian diffusivity values extracted from the QENS spectra at different temperatures are plotted in Figure 25 (blue filled circles). The Na self-diffusivity in the temperature range of 450 to 700 K is on the order of $10^{-6} \text{ cm}^2/\text{s}$, which falls in the same range with the similar layered compound $\text{Na}_{0.8}\text{CoO}_2$ from a QENS study¹⁹¹. Based on the Arrhenius fit for the temperature dependence of Na self-diffusivity, we obtained an activation energy of $0.15 \pm 0.004 \text{ eV}$ and a diffusivity of $\sim 10^{-7} \text{ cm}^2/\text{s}$ at room temperature. The low activation energy barrier of this material is comparable to some P2-type compounds including $\text{Na}_{2/3}[\text{Ni}_{1/3}\text{Mn}_{1/3}\text{Ti}_{1/3}]\text{O}_2$ (0.17 eV from FPMD¹⁹²), $\text{Na}_{0.8}\text{CoO}_2$ (0.17eV at $\sim 350\text{K}$ from QENS¹⁹¹), and $\text{Na}_x[\text{Ni}_{2/3}\text{Mn}_{2/3}]\text{O}_2$ with $1/3 < x < 2/3$ (0.17eV from the Nudged Elastic

Band (NEB) method¹⁸⁴). It is lower than some other P2 compounds such as $\text{Na}_{0.6}[\text{Cr}_{0.6}\text{Ti}_{0.4}]\text{O}_2$ (0.35 eV from FPMD⁹²), $\text{Na}_{5/6}\text{Li}_{1/12}\text{Ni}_{1/4}\text{Mn}_{2/3}\text{O}_2$ (0.28 eV from FPMD¹⁹³).

At large Q (small distance), the deviation from the linear relationship between Γ and Q^2 with Γ approaching a plateau suggests localized jump behavior. The Singwi-Sjölander (SS) jump model¹⁶³ was used to describe the local dynamics of Na ions (black line in Figure 24(b)), where the average residence time τ and mean jump length r were obtained from the Q -dependence of Γ based on :

$$\Gamma(Q) = \frac{1}{\tau} \left(\frac{Q^2 \langle r^2 \rangle / 6}{1 + Q^2 \langle r^2 \rangle / 6} \right) \quad \text{Eq. 35}$$

The SS model only applies to the short-range behaviors of Na dynamics at large Q . The mean jump length and residence time obtained from the SS model with the temperature dependence are plotted in Figure 25(b). The jump lengths are between 1 and 2 Å which fit into the dimension of the honeycomb sublattice in the Na layer, as the distance from an edge-share site to a nearest-neighbor face-share site and vice versa is around 1.7 Å. This confirms that Na primarily migrates between edge-share and face-share sites within the 2D diffusion pathway. The average jump length of Na increases with temperature, while the residence time decreases with temperature as more frequent and longer jumps can be activated by higher thermal energy.

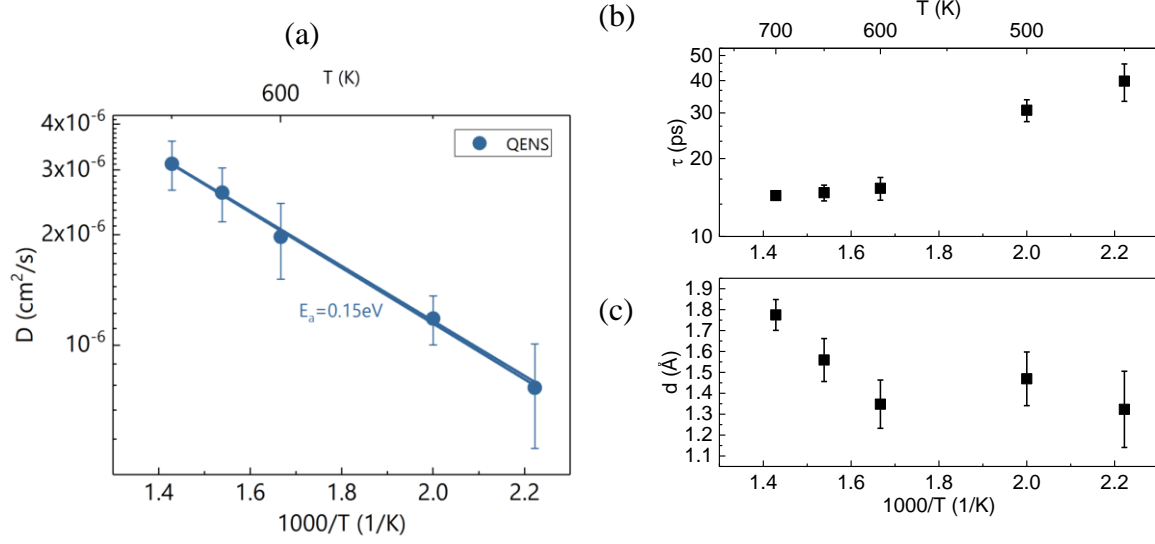


Figure 25: Diffusional properties from QENS at 450 to 700K: (a) The Fickian self-diffusivity of Na. (b) The residence time and (c) jump length of Na diffusion with the SS model.

5.3 Ionic conductivity and Na self-diffusion from IP-based MD

IP-based MD simulations were performed to study dynamic properties including diffusion behaviors and ionic conductivity at the larger time and length scale.

5.3.1 Construction of the polarizable interatomic potential model

Parameters for the polarizable interatomic potential model¹⁹⁴ were obtained from DFT results using the force-matching method. The charge for each atom was taken from the DFT calculation based on DDEC3 approach¹⁹⁵, as it provided better results in structure reproduction compared to DDEC6 charge¹²¹. The short-range pairwise interactions are described by a combination of Buckingham¹⁴³ and Morse¹⁴⁴ potential model as the following equation:

$$U^{ij} = Ae^{-r/\rho} - Cr_{ij}^{-6} + D[(1 - e^{-a(r_{ij}-r_0)})^2 - 1] \quad \text{Eq. 36}$$

The O atoms were treated as induced dipoles while other atoms were non-polarizable. The obtained polarizability for O is 1.99 \AA^3 . The Tang-Toennies damping functions¹⁹⁶ were applied

for correction of short-range charge-dipole interactions between atom i and atom j as the following equation:

$$g^{ij}(r_{ij}) = 1 - c^{ij} \exp(-b^{ij} r_{ij}) \sum_{k=0}^4 \frac{(b^{ij} r_{ij})^k}{k!} \quad \text{Eq. 37}$$

The obtained parameters are listed in Table 5.

Table 5: Polarizable interatomic potential parameters.

a. short-range pairwise interactions $U^{ij} = Ae^{-r/\rho} - Cr_{ij}^{-6} + D[(1 - e^{-a(r_{ij}-r_0)})^2 - 1]$

| Interactions | A(eV) | $\rho(\text{\AA})$ | C(eV \AA^6) | D(eV) | a(\AA^{-1}) | r ₀ (\AA) |
|--------------|--------|--------------------|-----------------------|-------|------------------------|---------------------------------|
| Na-O | 1300.1 | 0.28 | - | - | - | - |
| Ni-O | 1003.8 | 0.17 | - | 0.002 | 3.95 | 2.46 |
| Ti-O | 1907.4 | 0.27 | 14.8 | - | - | - |
| O-O | 1250.0 | 0.30 | 39.8 | - | - | - |

b. Tang-Toennies damping functions $g^{ij}(r_{ij}) = 1 - c^{ij} \exp(-b^{ij} r_{ij}) \sum_{k=0}^4 \frac{(b^{ij} r_{ij})^k}{k!}$

| Interactions | Na-O | Ni-O | Ti-O |
|-----------------|------|------|------|
| b ^{ij} | 2.86 | 3.46 | 2.96 |
| c ^{ij} | 1.72 | 1.41 | 0.91 |

As the parameters for the IP model were obtained from DFT through force-matching, the goodness of fitting was assessed by the root mean squared error (RMSE) of calculated forces on each type of atom. The RMSE are 0.182, 0.586, 0.737, and 0.451 eV/ \AA for Na, Ni, Ti, and O, respectively. The comparison of forces calculated from the obtained IP model and DFT is shown in Figure 26.

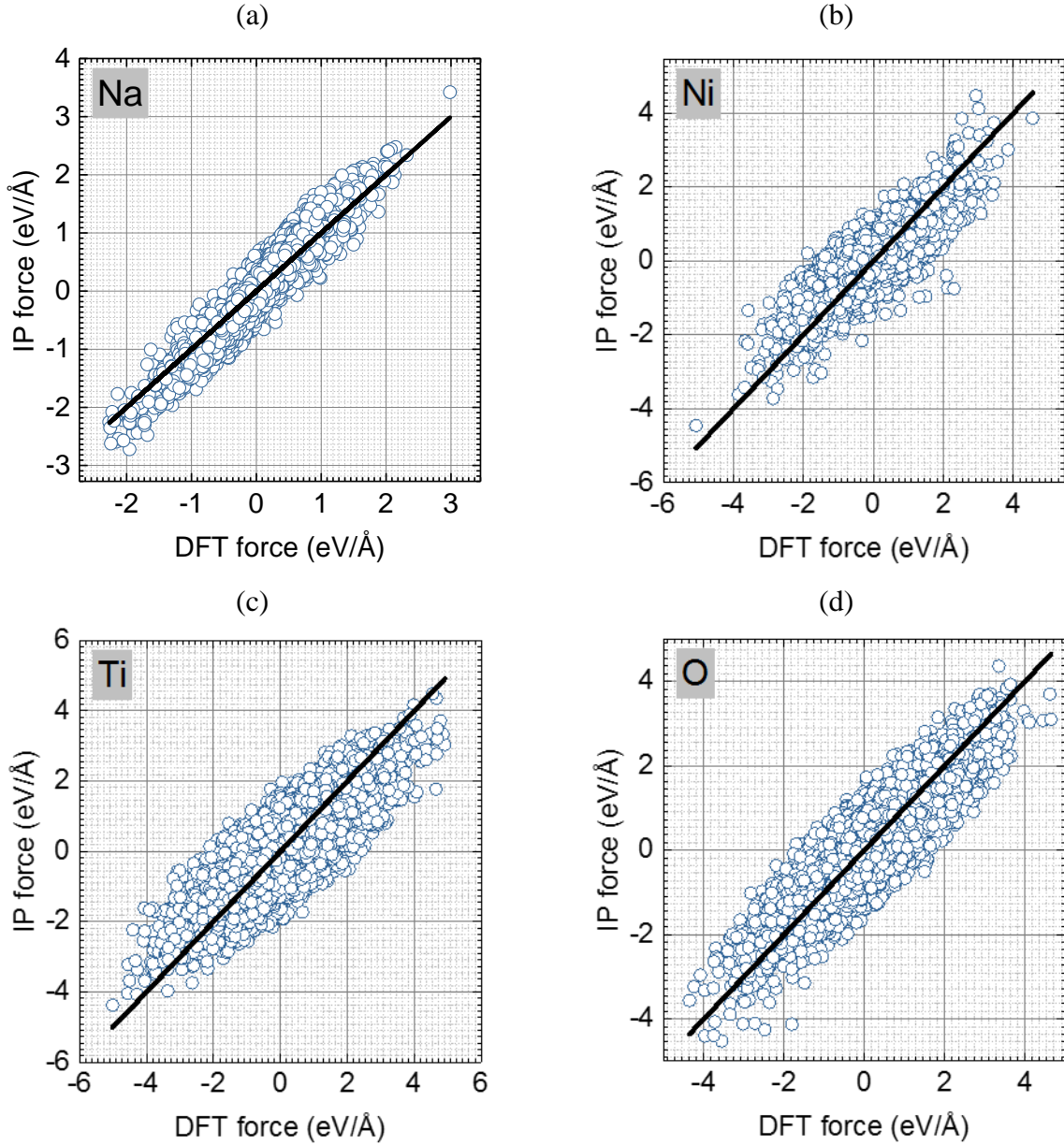


Figure 26: The comparison of IP forces (blue circles) and DFT forces (black line) on each type of atom.

5.3.2 IP-based MD simulations

The IP-based MD(IPMD) simulation was performed with the FIST module implemented in cp2k¹⁹⁷. A $9 \times 9 \times 3$ $\text{Na}_{2/3}[\text{Ni}_{1/3}\text{Ti}_{2/3}]\text{O}_2$ supercell containing 1782 atoms was used. An NPT ensemble was performed at different temperatures from 300 to 1200 K with a simulation time of 50 ps to obtain the lattice parameters. Due to the computational cost concerns, the NVE runs with 50 ps

equilibrium time were conducted at only high temperatures from 900 to 1200 K to calculate diffusion and ionic conduction, using incoherent density correlation functions and coherent charge-current correlation functions¹⁹⁸ respectively, as explicated below. The time step was 1 fs.

Both DFT and IP-based MD simulations with the NPT ensemble were used to predict the structure of P2-Na_{2/3}[Ni_{1/3}Ti_{2/3}]O₂ at different temperatures for the validation of the two models. The calculated unit cell parameters were compared with experimental results obtained from the previous neutron diffraction study (ND) by Shanmugam et al. for the same material¹⁷⁸ as shown in 3.2. For the lattice parameters at 300 K, calculated results from DFT and IP differ from the experiment by 0.41% and 1.42% along *a*, 1.09% and 0.11% along *c*, respectively. The reliabilities of the two models were confirmed by a small deviation between calculated and experimental results concerning both lattice constants and the thermal expansion along *a* and *c* direction.

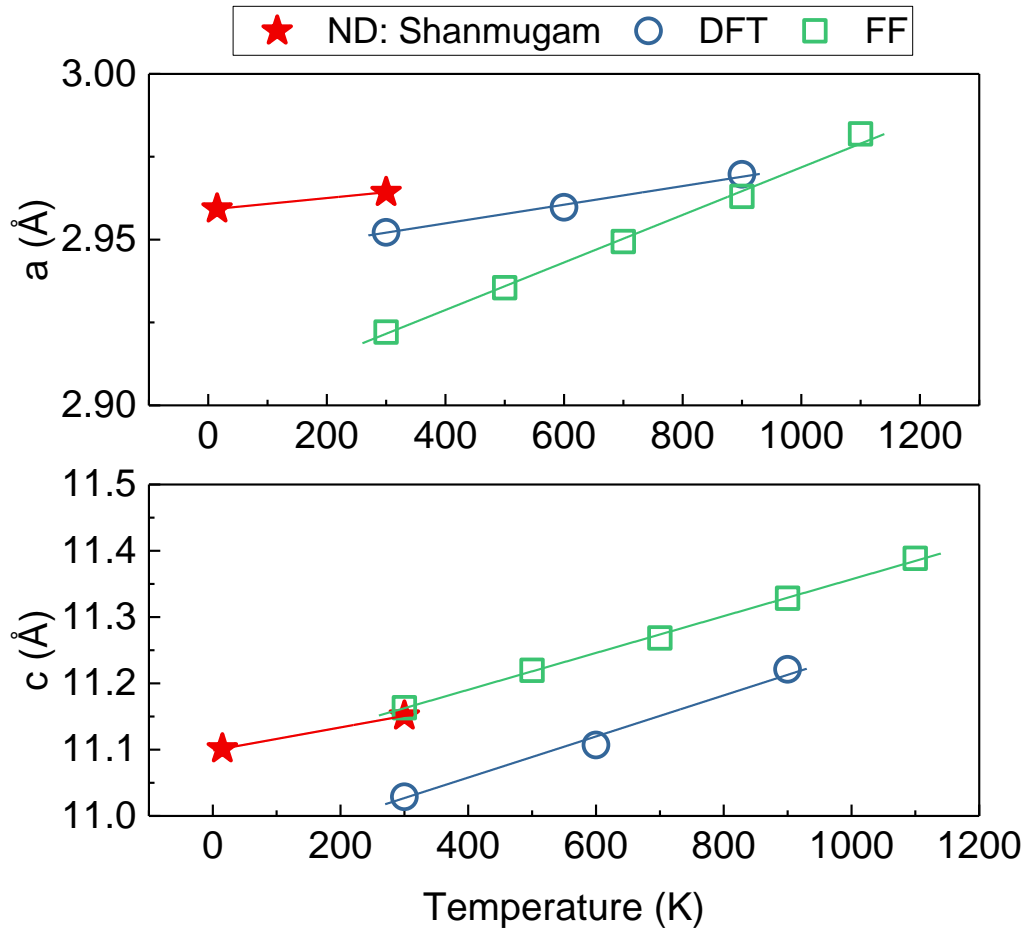


Figure 27: Lattice parameters of pristine $\text{P2-Na}_{2/3}[\text{Ni}_{1/3}\text{Ti}_{2/3}]\text{O}_2$ at different temperatures obtained from neutron diffraction by Shanmugam et al¹⁷⁸ (red stars), DFT-based MD (blue circles), and IP-based MD (green squares).

For the visualization of Na diffusion pathways in $\text{P2-Na}_{2/3}[\text{Ni}_{1/3}\text{Ti}_{2/3}]\text{O}_2$, the nuclear density map of Na was generated by plotting the Na atom distribution along the MD simulation trajectory. For clarity, the Na densities in the simulation cell at 1100 K were projected to a smaller cell ($3 \times 3 \times 1$) using VESTA¹⁷⁵ as in Figure 28. The Na trajectory reveals that Na ions are highly mobile along the *ab* plane at high temperatures, forming a honey-comb like 2D diffusion network connected by bridges between edge-share (E) and face-share (F) sites, similar to other layered P2 sodium insertion materials^{33,39}. The regions enclosed by the isosurface are larger for the edge-share sites

than for the face-share sites, suggesting higher occupancy at edge-share sites, consistent with the results from XRD as discussed in the previous section 3.2.

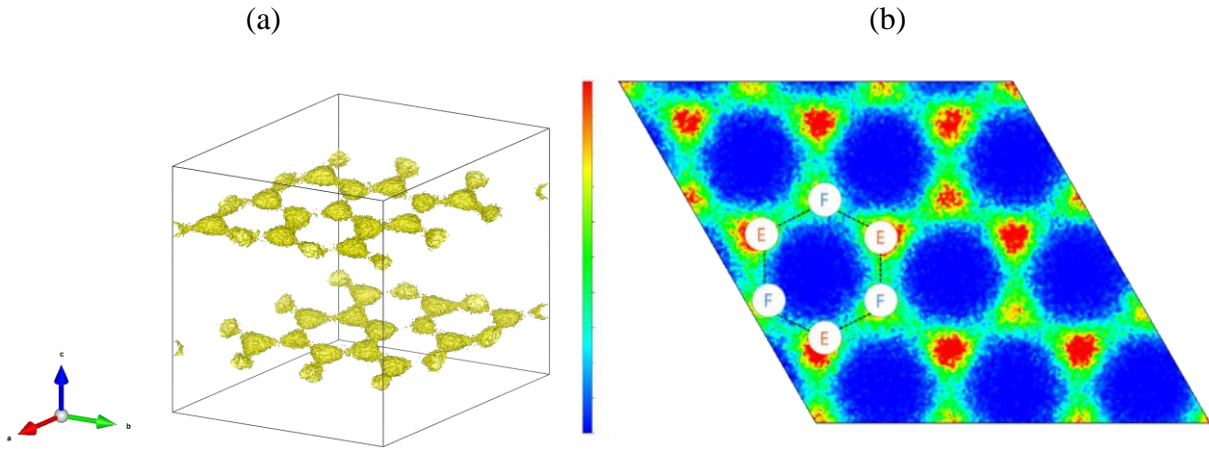


Figure 28: The nuclear density map of Na during 500 ps simulation at 1100 K. (a) 3D view with an isosurface level of 0.2 \AA^{-3} , (b) 2D slice on the (001) lattice plane with an isosurface level of $0\sim 0.5 \text{ \AA}^{-3}$. “E” and “F” represent edge-share sites and face-share sites

5.3.3 Extraction of diffusivity and ionic conductivity from IP-based MD

The diffusion and ionic conduction were calculated using incoherent density correlation functions and coherent charge-current correlation functions¹⁹⁸. For the calculation of Na self-diffusion, the production time for NVE is ranged from 1 ns (for 1200 K) to 8.5 ns (for 900 K) to ensure an adequate time of Na jumps were sampled. The position data were utilized every 1 ps. The incoherent density correlation function, also known as the incoherent intermediate scattering function, was calculated based on the following equation:

$$I_{\alpha}(Q, t) = \left\langle \frac{1}{N_{\alpha}} \sum_{n=1}^{N_{\alpha}} e^{-jQ \cdot r_n^{\alpha}(0)} e^{jQ \cdot r_n^{\alpha}(t)} \right\rangle$$

Where N_{α} stands for the total number of atom α and \mathbf{r} stands for the position vectors. \mathbf{Q} is the wave vector transfer, given by $\mathbf{Q}_{n_x n_y n_z} = n_x \mathbf{a}^* + n_y \mathbf{b}^* + n_z \mathbf{c}^*$, where \mathbf{a}^* , \mathbf{b}^* , \mathbf{c}^* are reciprocal unit vectors and n_x , n_y , and n_z are all integers.

The $I(\mathbf{Q}, t)$ for different \mathbf{Q} values were calculated from MD trajectories with values at 1100 K shown in Figure 29(a), for both through-plane \mathbf{Q} (red curves) and in-plane \mathbf{Q} (blue curves). The through-plane $I(\mathbf{Q}, t)$ have plateaus of around 1, suggesting no Na diffusion across the layer. This is consistent with the Na density map in Figure 28.

The relaxation of the correlation function $I(\mathbf{Q}, t)$ can be described by the stretched exponential decay, also known as the Kohlrausch-Williams-Watts (KWW) function¹⁹⁹:

$$I(Q, t) = \exp[-(\Gamma^{KWW} t)^{\beta}] \quad \text{Eq. 38}$$

where Γ^{KWW} represents the relaxation rate and β is the stretching factor ranged from 0 to 1. Both Γ^{KWW} and β are \mathbf{Q} -dependent and can be obtained by least-squared fitting. The mean relaxation rate Γ is given by $\Gamma = \frac{\Gamma^{KWW}}{\beta} G\left(\frac{1}{\beta}\right)$, where G is the gamma function. The obtained mean relaxation rate Γ with Q dependency is shown in Figure 29(b).

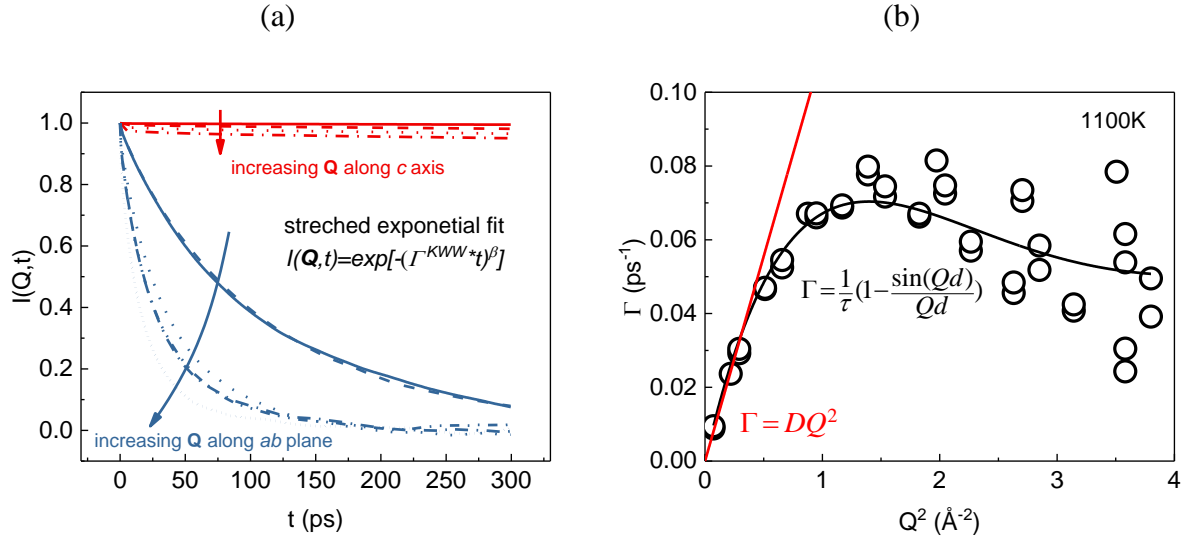


Figure 29: (a) The $I(\mathbf{Q},t)$ at 1100 K (b) Γ vs. Q^2 (black circles), with the CE fit (black line) and linear fit for the three smallest \mathbf{Q} (red line).

Within the small \mathbf{Q} regime of Figure 29(b), the Fickian diffusivity D was obtained by a linear fitting of Γ vs. Q^2 for the three smallest in-plane \mathbf{Q} values according to $\Gamma = DQ^2$. The Fickian self-diffusivity from 900 to 1200 K are plotted in Figure 30(a). The activation energy for Na diffusion obtained by the Arrhenius fit is 0.53 ± 0.02 eV. The extrapolated Na diffusion coefficient at 300 K is around 3×10^{-12} cm²/s, one order higher than the measured value from a previous study ($10^{-14} \sim 10^{-13}$ cm²/s)¹⁰⁴. For the entire \mathbf{Q} regime of Figure 29(a), the Chudley-Elliott jump model¹⁶² was used to describe the Na diffusion mechanism. According to the CE model, Γ was fitted to the

equation $\Gamma = \frac{1}{\tau} \left(1 - \frac{\sin(Qd)}{Qd}\right)$ as a function of \mathbf{Q} values to obtain the residence time τ and jump

length d . The temperature dependence of τ and d are plotted in Figure 30(b) and (c). The residence time τ decreases with increasing temperature (activation energy of 0.62 ± 0.04 eV), suggesting more frequent jumps with higher temperature. The decreasing jump length d with increasing temperature may be due to the growing delocalization of Na ions as temperature rises. Considering

that the distance between closest edge-share and face-share site is around 1.7 \AA , the mean jump length of

Na from 900 to 1200 K is roughly 2-3 times of that distance.

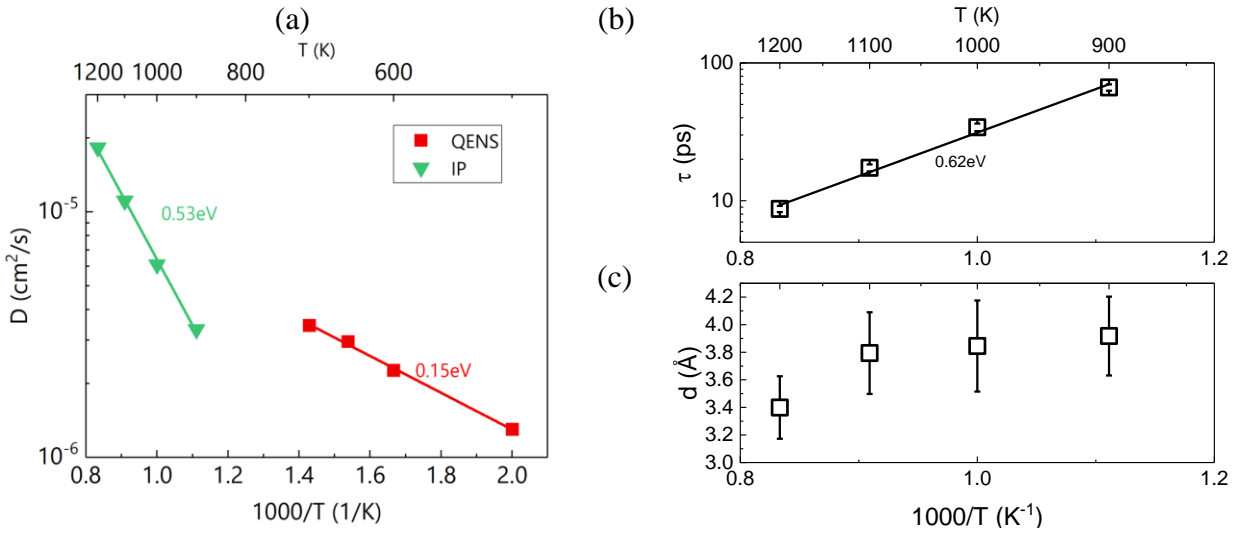


Figure 30: Diffusional properties from MD simulations at 900 to 1200 K: (a) The Fickian self-diffusivity of Na. (b) The residence time and (c) jump length of Na diffusion with the Chudley-Elliott model.

The results of Na diffusion from IP-based MD were compared to the results from QENS experiment in Figure 30(a). The IP-based MD showed high in-plane Na self Fickian diffusivity in a range of 10^{-6} ~ 10^{-5} cm²/s from 900 to 1200 K, with an activation energy of 0.53 ± 0.02 eV. The Na Fickian diffusivity measured from QENS experiment is around 10^{-6} cm²/s in the temperature range of 450 to 700 K, with an activation energy of 0.15 ± 0.004 eV. Two different jump models are found to well describe the Na jump behaviors for IP-based MD and QENS results, the Chudley-Elliott and the Singwi-Sjölander jump model, respectively. For both MD and QENS results, more frequent jumps were found at higher temperatures. However, the two models showed different trends of jump distance with respect to temperatures. The analysis based on the MD trajectory reveals that the Na ions migrate between the adjacent edge-sharing and face-sharing sites, which

is associated with the jump distance of around 1.7Å observed from QENS measurements. The inconsistency between the MD simulation results and the QENS experimental results including the large deviation between activation energy, the different jump mechanism and the different jump distance trend regarding temperature might be due to the limitations of the interatomic potential model as it relies on parametric forces and tends to neglect the underlying electronic origin of the interactions. Although we found this potential model worked well in predicting the structural properties like the lattice parameters and thermal expansion for this material, the performance of it for dynamic properties predictions may not be as good as for static properties.

The ionic conductivity was extracted from the IP-based MD trajectories using the coherent charge-current correlation function in the transverse polarization¹⁹⁸, i.e., with two directions perpendicular to each \mathbf{Q} probed. The transverse coherent charge-current correlation function was calculated based on the NVE trajectory ranged from 200 ps (for 1200 K) to 600 ps (for 900 K) sampling every 0.02 ps, with the following equation:

$$C^T(Q, t) = \frac{e^2}{Vk_B T} \frac{1}{2Q^2} \langle (Q \times J(Q, 0)) \cdot (Q \times J(-Q, t)) \rangle \quad \text{Eq. 39}$$

where V is the volume of the system, k_B the Boltzmann constant, and T the temperature. The charge current $\mathbf{J}(\mathbf{Q}, t)$ is given by $J(Q, t) = \sum_{n=1}^N q_n v_n(t) e^{-jQ \cdot r_n(t)}$, where q_n is the charge carried by the n^{th} atom, and \mathbf{v}_n and \mathbf{r}_n are velocity and position vectors. A Fourier transform in time of $C^T(\mathbf{Q}, t)$ can lead to $S^T(\mathbf{Q}, \omega)$ in the frequency domain as

$$S^T(Q, \omega) = \int_0^\infty C^T(Q, t) \exp(i\omega t) dt \quad \text{Eq. 40}$$

The DC ionic conductivity was approximated using $S^T(\mathbf{Q}, \omega)$ at smallest \mathbf{Q} (Q_{001} , Q_{010} and Q_{100}) and smallest ω (0.12 THz with 50 ps correlation time).

Figure 31 shows the real part of its result in the frequency domain at 1100 K for the small Q values ($Q_{100}=Q_{010}=0.27 \text{ \AA}^{-1}$ and $Q_{001}=0.18 \text{ \AA}^{-1}$), presenting four in-plane and two through-plane ionic conduction. The DC ionic conductivity was calculated by averaging the data points at the smallest frequency (around 0.12 THz as shown in Figure 31(b)). The in-plane ionic conductivity is several magnitudes higher than that of through-plane, as the ionic conduction in $\text{Na}_{2/3}[\text{Ni}_{1/3}\text{Ti}_{2/3}]\text{O}_2$ is mainly within the as the 2D ionic conduction layer formed by the NaO_6 prisms.

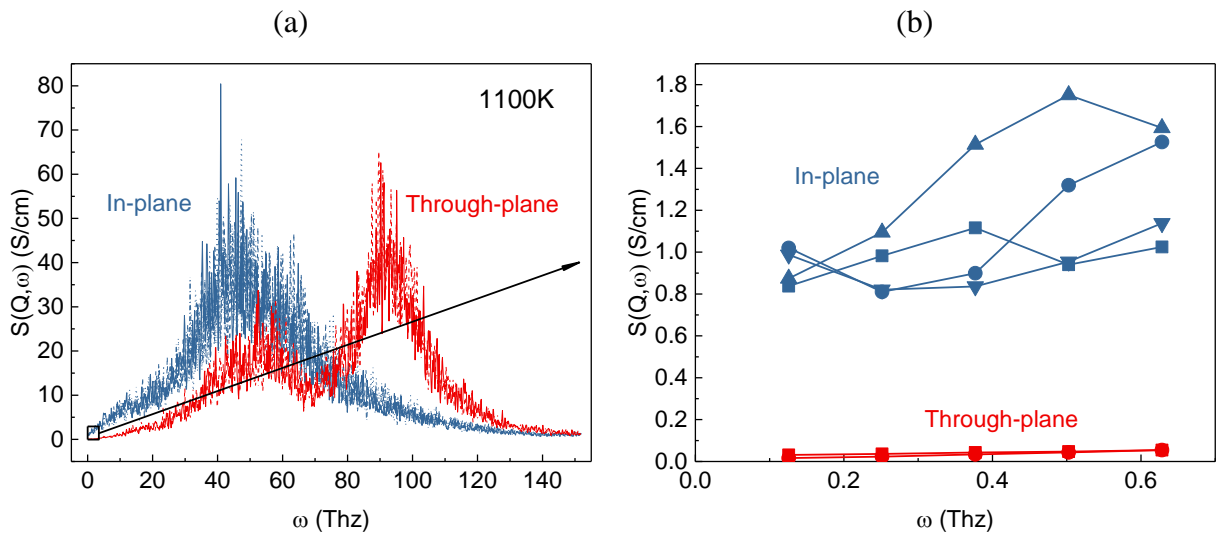


Figure 31: The real part of coherent charge-current correlation at 1100 K in (a) full frequency span. (b) the low-frequency region. The blue and red curves represent the in-plane and through-plan ionic conduction, respectively.

The calculated ionic conductivity at 900, 1000, 1100 and 1200 K are shown in Figure 32 along with experimental results from Shanmugam et al.¹⁰⁴, Shin et al.¹⁰³, and Smirnova et al.²⁰⁰ The calculated in-plane ionic conductivities from the IP-based MD matched well with the experimental results. The calculated activation energy was $0.37 \pm 0.03 \text{ eV}$, slightly higher than the experimental values.

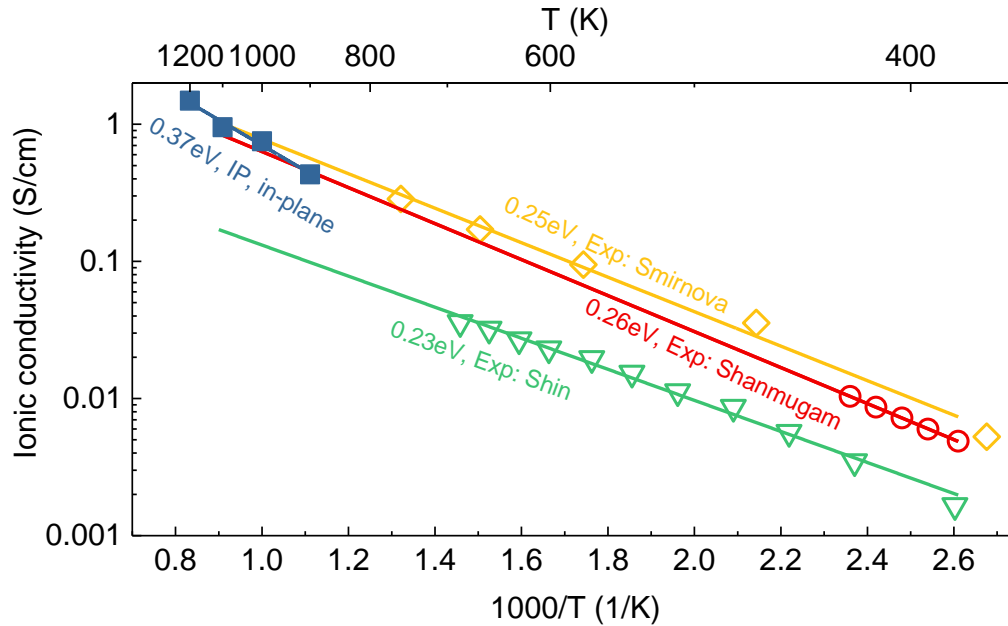


Figure 32: The calculated in-plane ionic conductivity of $\text{Na}_{2/3}[\text{Ni}_{1/3}\text{Ti}_{2/3}]\text{O}_2$ compared with experimental values from Shanmugam et al.¹⁰⁴, Shin et al.¹⁰³, Smirnova et al.²⁰⁰

5.4 First principles MD simulations

The first-principles molecular dynamics (FPMD) simulations based on DFT with the NVT ensemble were performed at 900, 1000, and 1100 K with an equilibrium time of 3 ps and production run time ranging from 20 ps to 100 ps. The parameters for the DFT calculations were the same as in section 4.2. The non-spin-polarized calculations were performed with a plane-wave energy cut-off of 450 eV and a single Γ point. The starting structure for pristine $\text{Na}_{2/3}[\text{Ni}_{1/3}\text{Ti}_{2/3}]\text{O}_2$ was a $3 \times 3 \times 1$ supercell containing 66 atoms. The configurations for $\text{Na}_{7/9}[\text{Ni}_{1/3}\text{Ti}_{2/3}]\text{O}_2$ and $\text{Na}_{5/9}[\text{Ni}_{1/3}\text{Ti}_{2/3}]\text{O}_2$ as the Na-rich and Na-deficient phases were generated by randomly adding and removing Na atoms from the pristine phase while maintaining the same number of Na atoms in each layer. For all compositions, the lattice parameters were determined based on an NPT ensemble run of 3ps. Convergence tests for the trajectory time and correlation time were performed

before extracting the diffusivity to make sure they are long enough. The time step was 1 fs for all temperatures.

The FPMD trajectory recording the positions of all Na ions provided the direct visualization of Na motion. We plotted the Na density maps from the MD trajectories as shown in Figure 33. Na density maps showed traces along the 2D honeycomb diffusion pathway in the Na layer, consistent with the jump length obtained from the QENS measurement.

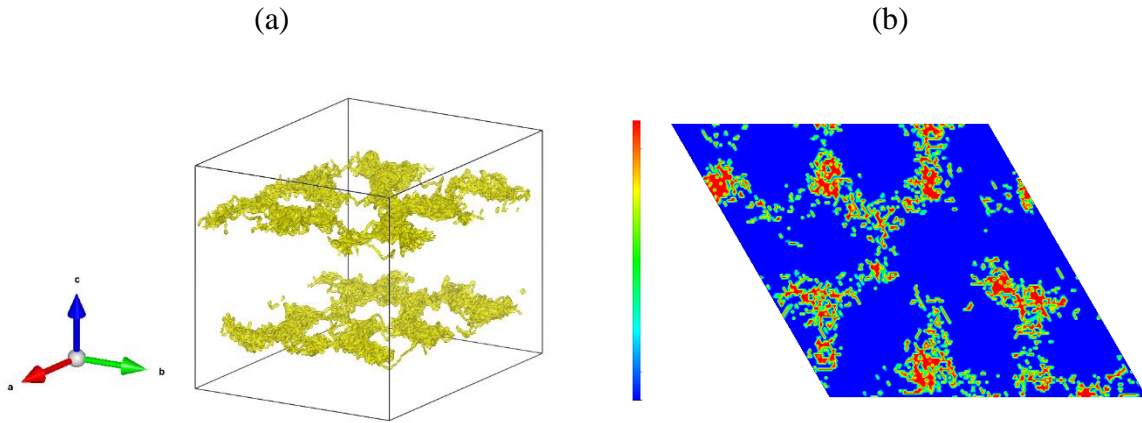


Figure 33: The nuclear density map of Na from 20 ps MD simulation trajectory at 1100 K. (a) 3D view with an isosurface level of 0.2 \AA^{-3} , (b) 2D slice on the (001) lattice plane with an isosurface level of $0\sim 0.5 \text{ \AA}^{-3}$.

From the simulation, the Fickian self-diffusion coefficient along direction X was calculated by the Green-Kubo integration of velocity autocorrelation function:

$$D_{\alpha}^X = \frac{1}{N_{\alpha}} \sum_{i=1}^{N_{\alpha}} \int_0^{\infty} \langle v_i^X(t) \cdot v_i^X(0) \rangle dt \quad \text{Eq. 41}$$

where N_{α} stands for the total number of atom α and v_i^X the X-direction component of velocity for the i^{th} atom. The Green-Kubo integral reached a plateau within a short correlation time. For D_{α}^X along the c axis, the integral plateaued around 0, suggesting no cross-plane diffusion,

consistent with what we observed from the Na density maps. The diffusion coefficients along a and b axis were obtained by averaging over a correlation time period in the plateau region (we selected 2-3 ps in this work).

The Fickian self-diffusivity along a and b axis as well as the averaged value over two directions in the temperature range 900 to 1100 K are plotted in Figure 34. The diffusivity extracted from the MD simulation is about two times higher than those from the QENS experiment when extrapolating to the same temperature. The activation energy obtained from the Arrhenius equation for in-plane Na diffusion from 900 to 1100 K is 0.20 ± 0.02 eV which is slightly higher than QENS results (0.15 eV).

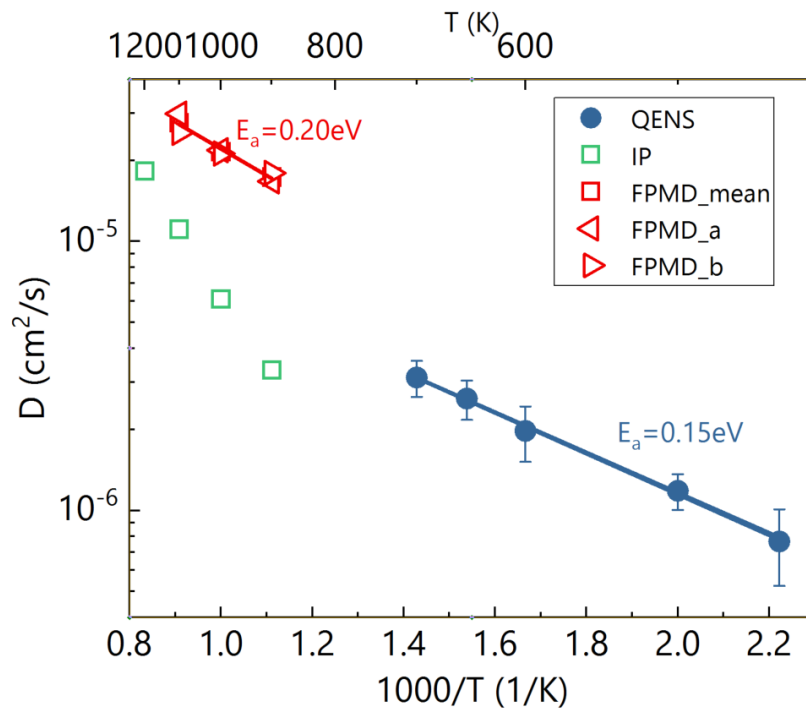


Figure 34: Calculated Fickian diffusivity from FPMD simulation (red) compared to results from IPMD(green) and QENS(blue).

While the FPMD simulation provides comparable results with the QENS experiment for the pristine material of sodium content $x=2/3$, to assess the Na diffusivity change during cycling,

we further calculated the diffusivity with the same approach for the other two compositions of $x=5/9$ and $7/9$. Figure 35 shows the calculated Na in-plane Fickian diffusivity for the three compositions at 900 K. From $x=2/3$ to $x=5/9$, $\text{Na}_{5/9}[\text{Ni}_{1/3}\text{Ti}_{2/3}]\text{O}_2$ shows a comparable diffusivity to $\text{Na}_{2/3}[\text{Ni}_{1/3}\text{Ti}_{2/3}]\text{O}_2$ with only a 3% increase. This trend is consistent with the diffusivity measured in this x range for $\text{Na}_x[\text{Ni}_{1/3}\text{Ti}_{2/3}]\text{O}_2$ ¹⁰⁴ as well as in other P2-type compounds^{184,192,201} using the Potentiostatic Intermittent Titration Technique (PITT) method. From $x=2/3$ to $x=7/9$, the insertion of Na ions into the pristine material leads to a significant drop in diffusivity, which can be attributed to the limited number of vacant sites.

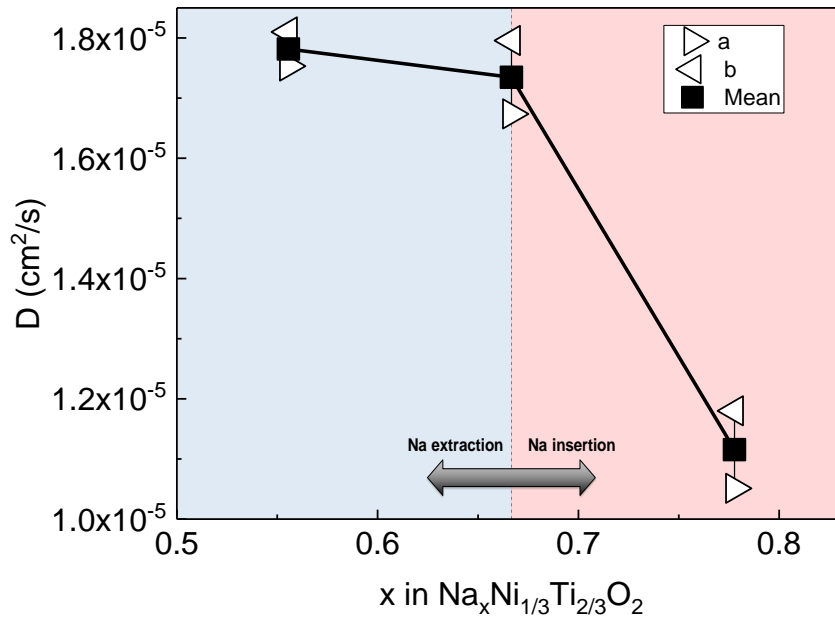


Figure 35: Calculated Fickian diffusivity from FPMD simulation at 900 K for different sodium content.

As the sodium diffusivity predicted by our first-principles MD simulations showed good consistency with the experiments, the ionic conductivity was also assessed using the MD trajectories. The ionic conductivity was calculated based on the Green-Kubo relations:

$$\sigma = \frac{1}{k_B T V} \int_0^{\infty} \langle J^X(t) J^X(0) \rangle dt \quad \text{Eq. 42}$$

where k_B is the Boltzmann constant, V the volume of the system, and T the temperature. The J^X represents the X-direction component of the charge current " $\mathbf{J} = \sum_{i=1}^N q_i \mathbf{v}_i(t)$ ". The charge carried by the i^{th} atom q_i was calculated using Density Derived Electrostatic and Chemical (DDEC6) charge analysis in our previous study²⁰². Similar to diffusion, the integral of charge current correlation along c axis converged to a plateau around zero within 1 ps, suggesting a 2D ionic conduction within the layers. The ionic conductivities along a and b axis were calculated from the mean integral of charge current correlation over a correlation time range from 2 to 3 ps. In-plane ionic conductivity at 900, 1000, and 1100 K were obtained by averaging the results along a and b axis as shown in Figure 36, along with computational results from our previous study based on the interatomic potential (IP) model²⁰² and experimental results from Shanmugam et al.¹⁰⁴, Shin et al.¹⁰³, and Smirnova et al.²⁰⁰ Calculated in-plane ionic conductivities from the FPMD, if extrapolated to lower temperatures, are slightly higher than experimental results. The calculated activation energy was 0.27 ± 0.27 eV, comparable to the experimental values, while our previous work with the IP model had a larger activation energy of 0.37 eV. The large error in the activation energy in the fitting mainly comes from the limited number of data points.

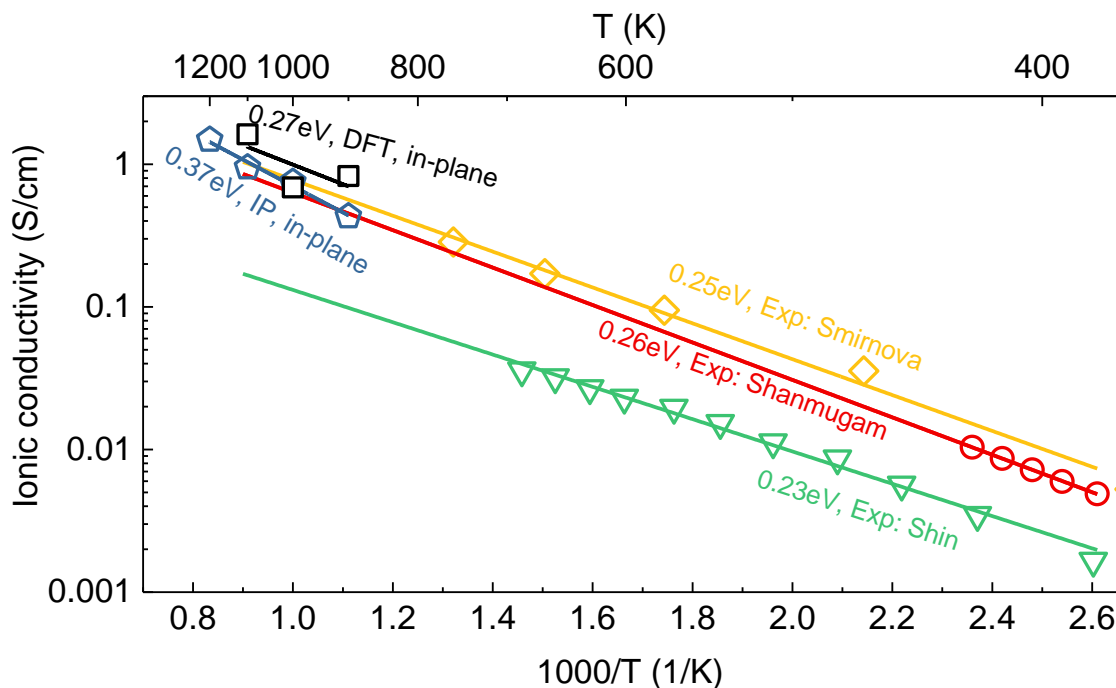


Figure 36: Calculated in-plane ionic conductivity of $\text{Na}_{2/3}\text{Ni}_{1/3}\text{Ti}_{2/3}\text{O}_2$ compared with computational values from Chen et al.²⁰² and experimental data from Shanmugam et al.¹⁰⁴, Shin et al.¹⁰³, and Smirnova et al.²⁰⁰

The Na concentration-dependence of the ionic conductivity was examined by calculating the conductivity values at 900 K for the other two compositions $\text{Na}_{5/9}[\text{Ni}_{1/3}\text{Ti}_{2/3}]\text{O}_2$ and $\text{Na}_{7/9}[\text{Ni}_{1/3}\text{Ti}_{2/3}]\text{O}_2$. As shown in Figure 37, both Na-deficient phase $\text{Na}_{5/9}[\text{Ni}_{1/3}\text{Ti}_{2/3}]\text{O}_2$ and Na-rich phase $\text{Na}_{7/9}[\text{Ni}_{1/3}\text{Ti}_{2/3}]\text{O}_2$ showed higher ionic conductivity compared to the pristine phase. From $x=2/3$ to $x=5/9$, when Na atoms are extracted from the pristine $\text{Na}_{2/3}[\text{Ni}_{1/3}\text{Ti}_{2/3}]\text{O}_2$, the increase of ionic conductivity is likely to be related to increased vacancies. From $x=2/3$ to $x=7/9$, when the Na atoms are inserted to $\text{Na}_{2/3}[\text{Ni}_{1/3}\text{Ti}_{2/3}]\text{O}_2$, higher ionic conductivity can be achieved with more charge carriers.

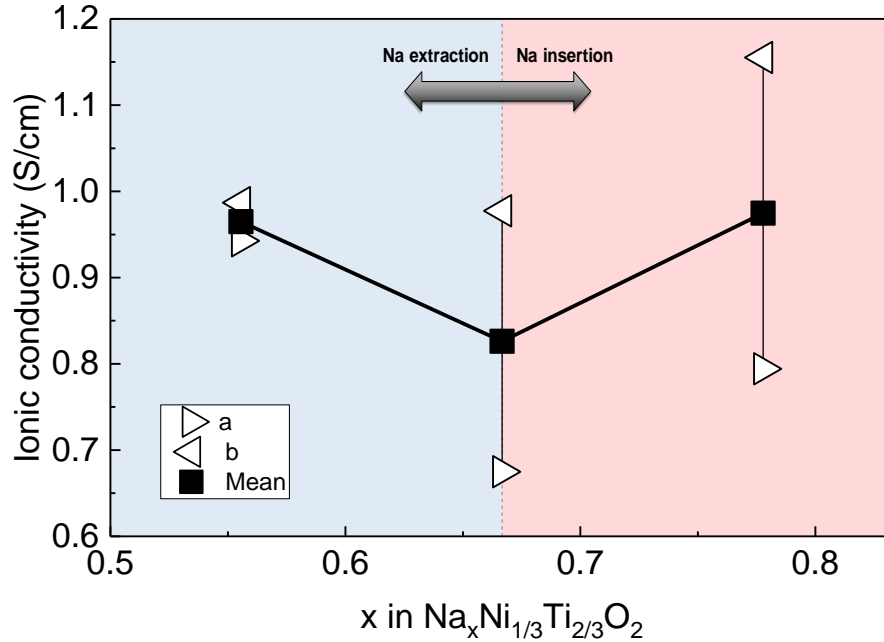


Figure 37: The calculated in-plane ionic conductivity from FPMD simulation at 900 K for different sodium content.

5.5 Conclusions

In this chapter, the P2-type layered material $\text{Na}_x[\text{Ni}_{1/3}\text{Ti}_{2/3}]\text{O}_2$ was investigated with a combination of quasi-elastic neutron scattering and molecular dynamics to study the Na ion diffusion mechanism and ionic conduction. Firstly, based on the Q-dependence of the quasi-elastic broadening in QENS measurement, the localized Na ion diffusion behavior can be described by the Singwi-Sjölander jump model. The extracted average jump lengths are around 1.3~1.8 Å at 450~700 K, corresponding to the distance between the neighboring edge-share and face-share sites. This is also consistent with the diffusion mechanism revealed by the density maps from MD simulations: 2D local jumps occur between the edge-share and face-share Na sites. More frequent and longer jumps were observed at higher temperatures. From the IPMD simulations, the short-range behaviors can be described by the Chudley-Elliott jump model, with more frequent and shorter jumps at higher temperatures. For long-range diffusivity, Fick's model was applied to

compare with the MD simulation results where $Q \rightarrow 0$. The QENS showed a Fickian diffusivity in the order of $\sim 10^{-6}$ cm²/s from 450 to 700 K with $E_a = 0.15 \pm 0.004$ eV. The IPMD simulations showed the Na self Fickian diffusivity in a range of $10^{-6} \sim 10^{-5}$ cm²/s from 900 to 1200 K, with an activation energy of 0.53 ± 0.02 eV. The FPMD simulation gave an in-plane diffusivity of $\sim 10^{-5}$ cm²/s with $E_a = 0.20 \pm 0.02$ eV in the temperature range of 900 to 1100 K. The diffusion coefficients were calculated for different compositions with the Na concentration x in the range of $5/9$ to $7/9$ using FPMD. Faster diffusion was observed for compositions with less sodium, i.e., more vacancies. Secondly, The IPMD simulations showed an in-plane ionic conductivity from 900 to 1200 K ranged in $0.4 \sim 1.4$ S/cm, with an activation energy of 0.37 ± 0.03 eV. The FPMD simulations showed in-plane ionic conductivity values ~ 1 S/cm at 900 to 1100 K with an activation energy of 0.27 eV, which is in better consistency with experimental measurements in previous studies. Both Na-deficient phase $\text{Na}_{5/9}[\text{Ni}_{1/3}\text{Ti}_{2/3}]\text{O}_2$ and Na-rich phase $\text{Na}_{7/9}[\text{Ni}_{1/3}\text{Ti}_{2/3}]\text{O}_2$ showed higher ionic conductivity compared to the pristine phase.

CHAPTER 6 Study on P2/O3 $\text{Na}_{2x}[\text{Ni}_x\text{Ti}_{1-x}]\text{O}_2$ with machine learning based interatomic potential models

6.1 Introduction

Besides P2-type $\text{Na}_{2x}[\text{Ni}_x\text{Ti}_{1-x}]\text{O}_2$, O3- $\text{Na}_{2x}[\text{Ni}_x\text{Ti}_{1-x}]\text{O}_2$ is also an important class in layered sodium transition metal compounds, sharing the same structure with the commercialized electrode material in lithium-ion batteries LiCoO_3 . In O3- $\text{Na}_{2x}[\text{Ni}_x\text{Ti}_{1-x}]\text{O}_2$, Na ions occupy the octahedral sites with 3 TM layers in the unit cell. The O3 type $\text{Na}_x[\text{TM}]\text{O}_2$ can be synthesized at a lower temperature compared to the P2 analogs³¹ and possess more sodium based on stoichiometry. With the electrochemical performance of the O3 type $\text{Na}_x[\text{Ni}_y\text{Ti}_{1-y}]\text{O}_2$ as electrode material discussed in a few experimental studies^{102,182,203}, further investigation is needed to understand the diffusion mechanism in this material, which will help us to better understand the relationship between structure and properties and to develop better electrode materials for sodium-ion batteries.

In previous chapters, MD simulations based on empirical IP models and DFT calculations, as well as QENS experiments, have been employed to study the diffusion in P2-type layered material $\text{Na}_{2/3}[\text{Ni}_{1/3}\text{Ti}_{2/3}]\text{O}_2$. Empirical IP models showed an inconsistency between the MD results and QENS experimental results including the large deviation between activation energies, different jump mechanisms, and different jump distance trends regarding temperature, indicating an insufficient accuracy of the potential model. Higher accuracy can be obtained from first principles MD simulations based on DFT. However, the high computational cost of DFT calculations has limited DFT-based MD to small systems with short time frames, thus only conducted at high temperatures in most studies to ensure sufficient dynamic statistics, while most experiments are conducted at room temperature to measure diffusion and ionic conduction. To bridge the gap

between computational and experimental results, it is essential to develop a potential model with both low computational cost and high accuracy.

Machine learning (ML) based interatomic potential (IP) models have emerged in recent years as a powerful tool to model the potential energy surface with comparable accuracy and higher efficiency than first principles calculations^{204,205}. Among the ML potential models, neural network (NN) potentials¹⁴⁹ are widely used and have been applied to study different materials²⁰⁶⁻²⁰⁸. In this chapter, we constructed NN potentials for both P2 and O3-type $\text{Na}_x[\text{Ni}_y\text{Ti}_{1-y}]\text{O}_2$. We first validated the reliability and accuracy of the NN potential. After that, we performed MD simulations based on the NN potential to investigate the diffusion and ionic conduction in P2-type $\text{Na}_{2/3}[\text{Ni}_{1/3}\text{Ti}_{2/3}]\text{O}_2$ and O3-type $\text{Na}_{0.83}[\text{Ni}_{0.42}\text{Ti}_{0.58}]\text{O}_2$.

6.2 Construction of the neural network potential

The neural network (NN) potentials are trained using the SIMPLE-NN package²⁰⁹. The reference data set for the training is constructed with snapshots from first principles MD simulations based on DFT. All DFT calculations were performed using the Vienna Ab initio Simulation Package (VASP)¹⁷⁹ using the same setup as in section 5.4. The MD simulations were conducted in a temperature span of 300 K to 2000 K for both P2 and O3 $\text{Na}_{2x}[\text{Ni}_x\text{Ti}_{1-x}]\text{O}_2$ with different compositions. The structures included in the training and validation set are listed in Table 6. A total of 10243 structures are included in the training set and 1135 structures in the validation set. Gaussian density function (GDF) weighting²¹⁰ was used to improve the sampling for the training process.

Table 6: Structures used in the training and validation set

| P2/O3 | Composition | Number of atoms |
|--------------|--|------------------------|
| P2 | $\text{Na}_{0.67}[\text{Ni}_{0.33}\text{Ti}_{0.67}]\text{O}_2$ | 66 |

Table 6 (cont'd)

| | | |
|----|---|-----|
| P2 | Na _{0.44} [Ni _{0.33} Ti _{0.67}]O ₂ | 62 |
| P2 | Na _{0.56} [Ni _{0.33} Ti _{0.67}]O ₂ | 64 |
| P2 | Na _{0.61} [Ni _{0.33} Ti _{0.67}]O ₂ | 65 |
| P2 | Na _{0.72} [Ni _{0.33} Ti _{0.67}]O ₂ | 67 |
| P2 | Na _{0.78} [Ni _{0.33} Ti _{0.67}]O ₂ | 68 |
| P2 | Na _{0.89} [Ni _{0.33} Ti _{0.67}]O ₂ | 70 |
| P2 | Na _{0.67} [Ni _{0.33} Ti _{0.67}]O ₂ | 264 |
| O3 | Na _{0.67} [Ni _{0.33} Ti _{0.67}]O ₂ | 99 |
| O3 | Na _{0.78} [Ni _{0.39} Ti _{0.61}]O ₂ | 204 |
| O3 | Na _{0.89} [Ni _{0.44} Ti _{0.56}]O ₂ | 105 |
| O3 | Na _{0.83} [Ni _{0.42} Ti _{0.58}]O ₂ | 184 |

Atom-centered symmetry functions (ACSF)¹⁴⁵ were used as descriptors for the local atomic environment. 8 radial symmetry functions for each pair and 18 angular symmetry functions for each triplet are applied with the parameters same as a previous study on TiO₂²⁰⁸. The parameters are shown in Table 7. Same symmetry functions with a cutoff radius of 6 Å are used for all the atoms. Each atomic NN has two hidden layers with 30 nodes in each layer, leading to a 212-30-30-1 NN architecture. The hyperbolic tangent function is used as the activation function. The sum of mean square errors for energies and forces is minimized with an Adam optimizer²¹¹ during the training process. The root mean squared errors (RMSE) of energy and force for the training set are 15 meV and 0.7 eV/Å, respectively.

Table 7: Parameters of symmetry functions for all atoms

a. Parameters in radial symmetry functions

$$G_i^2 = \sum_j e^{-\eta(R_{ij}-R_s)^2} \cdot f_c(R_{ij})$$

$$R_s = 0$$

| No. | $\eta(\text{Å}^{-2})$ |
|-----|-----------------------|
| 1 | 0.003214 |

Table 7 (cont'd)

| | |
|---|----------|
| 2 | 0.035711 |
| 3 | 0.071421 |
| 4 | 0.124987 |
| 5 | 0.214264 |
| 6 | 0.357106 |
| 7 | 0.714213 |
| 8 | 1.428426 |

b. Parameters in radial symmetry functions

$$G_i^4 = 2^{1-\zeta} \sum_{j,k \neq i}^{\text{all}} (1 + \lambda \cos \theta_{ijk})^\zeta \cdot e^{-\eta(R_{ij}^2 + R_{ik}^2 + R_{jk}^2)} \cdot f_c(R_{ij}) \cdot f_c(R_{ik}) \cdot f_c(R_{jk})$$

| No. | $\eta(\text{\AA}^{-2})$ | ζ | λ |
|-----|-------------------------|---------|-----------|
| 1 | 0.000357 | 1 | -1 |
| 2 | 0.028569 | 1 | -1 |
| 3 | 0.089277 | 1 | -1 |
| 4 | 0.000357 | 2 | -1 |
| 5 | 0.028569 | 2 | -1 |
| 6 | 0.089277 | 2 | -1 |
| 7 | 0.000357 | 4 | -1 |
| 8 | 0.028569 | 4 | -1 |
| 9 | 0.089277 | 4 | -1 |
| 10 | 0.000357 | 1 | 1 |
| 11 | 0.028569 | 1 | 1 |
| 12 | 0.089277 | 1 | 1 |
| 13 | 0.000357 | 2 | 1 |
| 14 | 0.028569 | 2 | 1 |
| 15 | 0.089277 | 2 | 1 |
| 16 | 0.000357 | 4 | 1 |
| 17 | 0.028569 | 4 | 1 |
| 18 | 0.089277 | 4 | 1 |

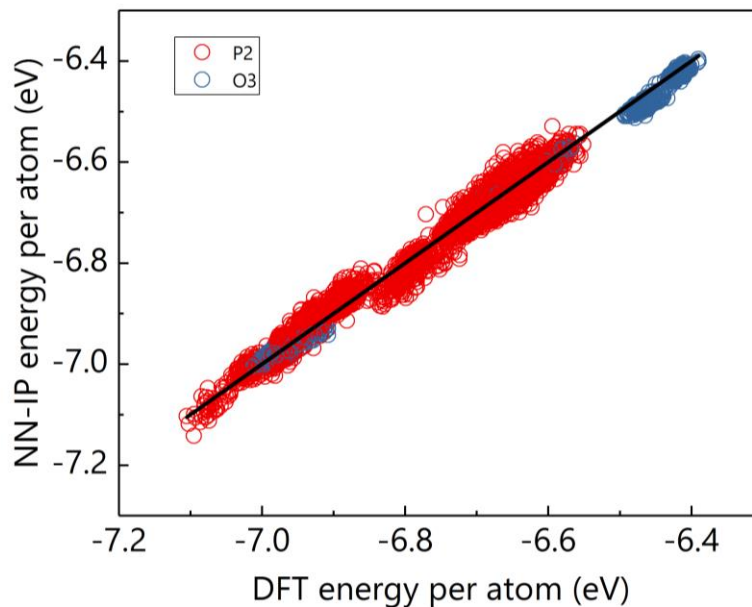


Figure 38: The comparison of NN-IP energies (red circles for P2 structures and blue circles for O3 structures) and DFT energies (black line) for the training set.

6.3 Testing the NN potential

To assess the reliability of the NN potential, we calculated energies and forces for structures not included in either the training or validation set using this potential and compared them to the results from DFT. The overall RMSE of energies for the P2 and O3 test set is 16.9 and 9.47 meV per atom, respectively. Figure 39 shows the comparison of forces calculated from NN-IP potential and DFT for a P2 and an O3 test set for each type of atom. The force RMSE of Na, Ni, Ti, and O for the P2 test set is 0.12, 0.45, 0.34, and 0.48 eV/Å, respectively, with an overall RMSE of 0.36 eV/Å. The force RMSE of Na, Ni, Ti, and O for the O3 test set is 0.13, 0.47, 0.35, and 0.47 eV/Å, respectively, with an overall RMSE of 0.35 eV/Å. The test results demonstrated good transferability and ability of this potential in predicting energy and force for both P2 and O3 systems.

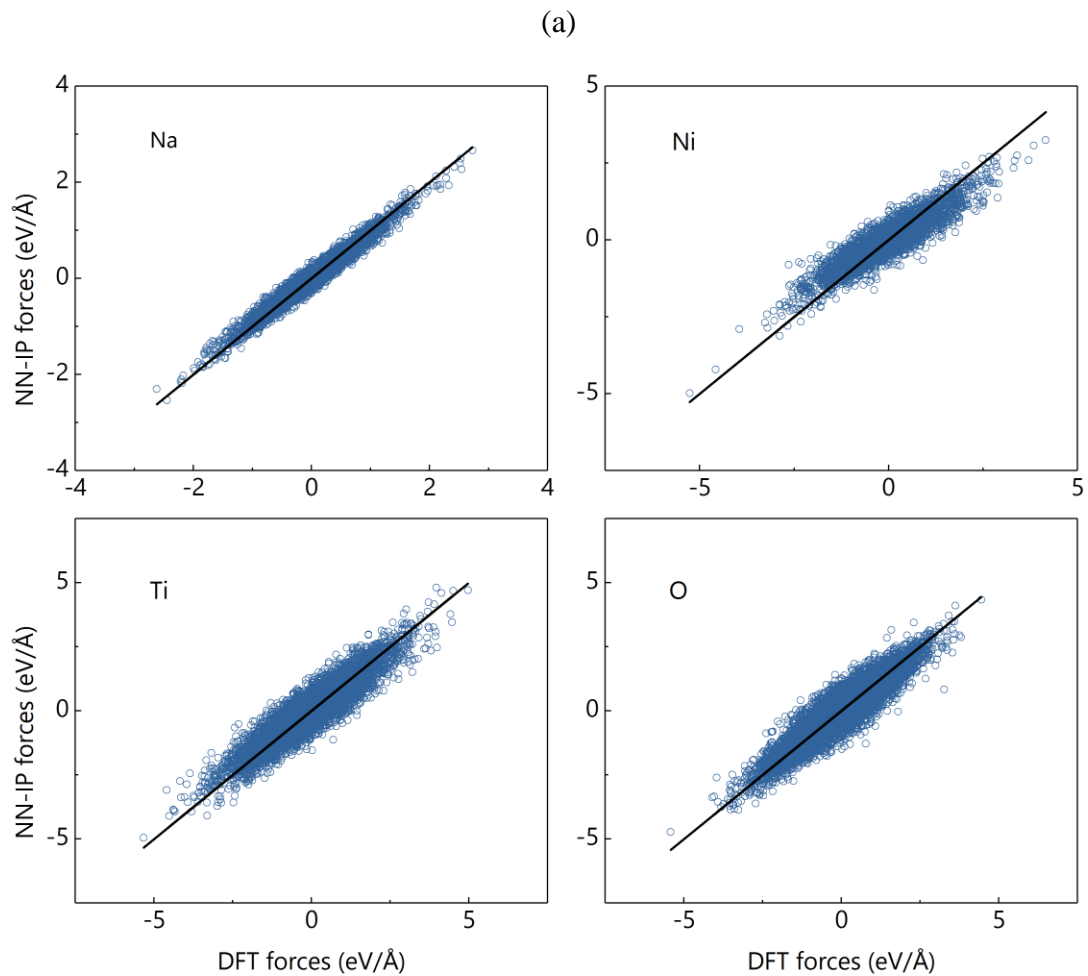
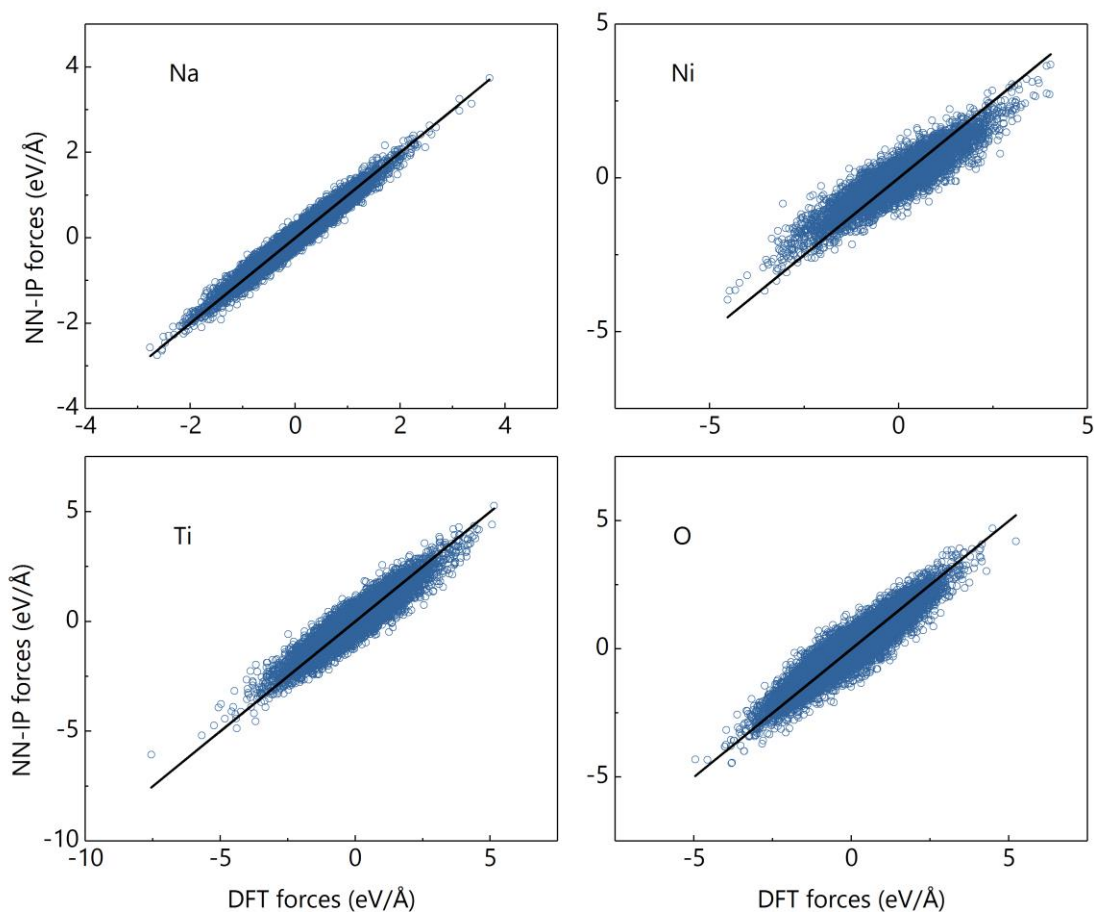


Figure 39: The comparison of NN-IP forces (blue circles) and DFT energies (black line) for the test set for each type of atom in (a) P2 structures and (b) O3 structures.

Figure 39 (cont'd)

(b)



6.4 MD simulations with the NN potential

MD simulations were performed based on the NN potential using LAMMPS²¹² for both P2 type and O3 type $\text{Na}_{2x}[\text{Ni}_x\text{Ti}_{1-x}]\text{O}_2$. MD simulations were conducted for a P2 $\text{Na}_{2/3}[\text{Ni}_{1/3}\text{Ti}_{2/3}]\text{O}_2$ supercell containing 1782 atoms from 300 to 1200 K and an O3 $\text{Na}_{0.83}[\text{Ni}_{0.42}\text{Ti}_{0.58}]\text{O}_2$ supercell containing 3312 atoms from 300 to 900 K. The time step was 1 fs for all MD simulations. An NPT ensemble was performed with a simulation time of 20 ps followed by an NVT ensemble with trajectory length ranging from 100 ps to 1 ns at different temperatures.

6.4.1 Calculation of lattice parameters

The average lattice parameters at different temperatures were calculated for P2 $\text{Na}_{2/3}[\text{Ni}_{1/3}\text{Ti}_{2/3}]\text{O}_2$ and O3 $\text{Na}_{0.83}[\text{Ni}_{0.42}\text{Ti}_{0.58}]\text{O}_2$ using NN-IP based MD simulations with the NPT ensemble. The results for P2 $\text{Na}_{2/3}[\text{Ni}_{1/3}\text{Ti}_{2/3}]\text{O}_2$ from 300 to 1200 K are compared to the experimental results measured from neutron diffraction (ND)¹⁷⁸ and simulation results calculated from MD simulations based on DFT and empirical polarizable IP models in Figure 40. Comparing to the ND results, the lattice parameters for P2- $\text{Na}_{2/3}[\text{Ni}_{1/3}\text{Ti}_{2/3}]\text{O}_2$ at 300K are 1.24% lower along both a and c , with the thermal expansion coefficient slightly larger along a and similar along c .

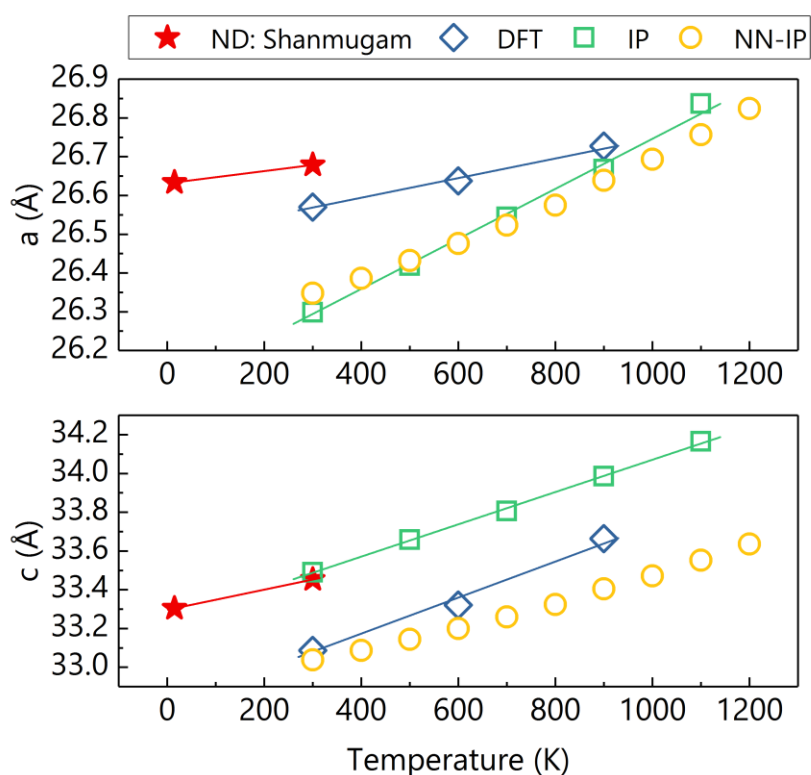


Figure 40: Lattice parameters of P2- $\text{Na}_{2/3}[\text{Ni}_{1/3}\text{Ti}_{2/3}]\text{O}_2$ at different temperatures obtained from NN-IP based MD simulations (yellow circles) compared to results from neutron diffraction by Shanmugam et al¹⁷⁸ (red stars), DFT-based MD (blue diamonds), and IP-based MD (green squares).

Lattice parameters for O3 $\text{Na}_{0.83}[\text{Ni}_{0.42}\text{Ti}_{0.58}]\text{O}_2$ obtained from NN-IP based MD are shown in Figure 41 compared to experimental data. The experimental data for $\text{Na}_{0.83}[\text{Ni}_{0.42}\text{Ti}_{0.58}]\text{O}_2$ are extrapolated based on data for $\text{Na}_{0.8}[\text{Ni}_{0.4}\text{Ti}_{0.6}]\text{O}_2$ and $\text{Na}_{0.85}[\text{Ni}_{0.48}\text{Ti}_{0.52}]\text{O}_2$ at room temperature in an XRD study by Fielden¹⁰⁵ et al. The calculated lattice parameters from NN-IP at 300 K differ from experiment by 0.08% along a and 1.03% along c . The thermal expansion coefficient is $2.53 \times 10^{-5} \text{ K}^{-1}$ along both a and c , which is higher than the thermal expansion coefficient $2.53 \times 10^{-5} \text{ K}^{-1}$ of a similar composition O3-type $\text{Na}_{0.8}[\text{Ni}_{0.4}\text{Ti}_{0.6}]\text{O}_2$ reported in a previous experimental study²⁰⁰. The reliability of the NN potential model is confirmed with an overall good consistency in lattice parameters for both P2 and O3 $\text{Na}_{2x}[\text{Ni}_x\text{Ti}_{1-x}]\text{O}_2$ with other studies.

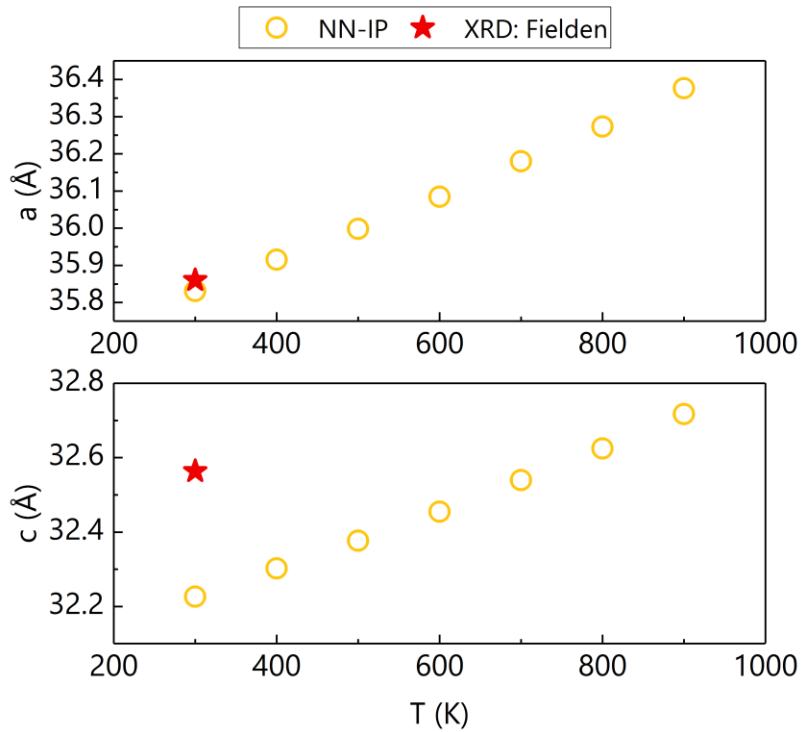


Figure 41: Lattice parameters of O3 $\text{Na}_{0.83}[\text{Ni}_{0.42}\text{Ti}_{0.58}]\text{O}_2$ at different temperatures obtained from NN-IP based MD simulations (yellow circles) compared to results extrapolated from XRD by Fielden et al.¹⁰⁵ (red stars)

6.4.2 Diffusion and ionic conduction

The diffusion coefficient of Na ions in P2- $\text{Na}_{2/3}[\text{Ni}_{1/3}\text{Ti}_{2/3}]\text{O}_2$ and O3- $\text{Na}_{0.83}[\text{Ni}_{0.42}\text{Ti}_{0.58}]\text{O}_2$ are calculated based on the mean square displacement in the MD trajectories according to $D = \frac{1}{2dt} \langle [\mathbf{r}_i(t) - \mathbf{r}_i(0)]^2 \rangle$, where $\mathbf{r}_i(t)$ is the position vector of particle I at time t. d is the dimensionality of the diffusion, which is 2 in this case as the diffusion is only observed within the *ab* plane for both P2 and O3 systems.

The diffusivity of Na from 500 to 1200 K calculated from IP-NN based MD simulations for P2 $\text{Na}_{2/3}[\text{Ni}_{1/3}\text{Ti}_{2/3}]\text{O}_2$ is shown in Figure 42 compared with results from FPMD simulations and QENS experiments. The diffusivity values for P2 $\text{Na}_{2/3}[\text{Ni}_{1/3}\text{Ti}_{2/3}]\text{O}_2$ are 3×10^{-7} to 2×10^{-5} cm^2/s from 500 to 1200K, slightly lower than both FPMD and QENS results. The activation energy obtained from the Arrhenius equation is 0.32 ± 0.01 eV, which is higher than that from FPMD and QENS.

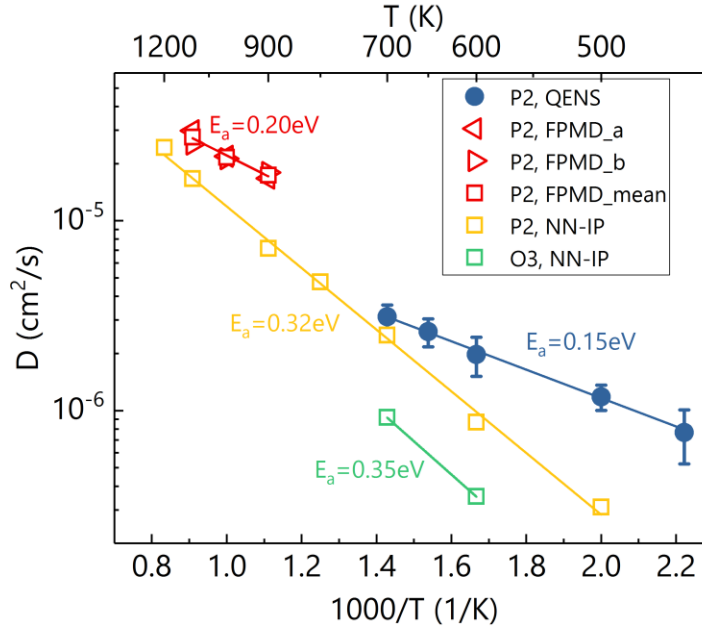


Figure 42: Fickian diffusivity of Na in P2- $\text{Na}_{2/3}[\text{Ni}_{1/3}\text{Ti}_{2/3}]\text{O}_2$ and O3-

$\text{Na}_{0.83}[\text{Ni}_{0.42}\text{Ti}_{0.58}]\text{O}_2$ calculated from IP-NN based MD simulations (yellow squares for P2-

Na_{2/3}[Ni_{1/3}Ti_{2/3}]O₂ and green squares for O3-Na_{0.83}[Ni_{0.42}Ti_{0.58}]O₂) compared to results for P2-Na_{2/3}[Ni_{1/3}Ti_{2/3}]O₂ from FPMD(green squares) and QENS(blue circles).

Figure 42 shows a comparison of Na diffusion coefficients in P2-Na_{2/3}[Ni_{1/3}Ti_{2/3}]O₂ and O3-Na_{0.83}[Ni_{0.42}Ti_{0.58}]O₂. From 600 to 700 K, O3-Na_{0.83}[Ni_{0.42}Ti_{0.58}]O₂ showed a lower Na diffusivity and higher activation energy (0.35 eV) than the P2 system in the same temperature range, consistent with the observations of similar materials such as Na_xCoO₂ from first principles MD simulations³³ and Na_x[Ni_{1/3}Mn_{2/3}]O₂ from GITT measurement¹⁸⁴. Such difference is mainly due to the different Na diffusion mechanisms in different structures. As discussed in previous chapters, Na ions mainly diffuse between the neighboring edge-share and face-share prismatic sites, providing larger space for Na ions to move than in O3 type materials, where Na ions diffuse through narrow triangular faces between octahedrons.

The ionic conductivity was calculated based on the Einstein-Helfand equation as Eq. 43. k_B is the Boltzmann constant, T the temperature, and V the volume. q_i is the charge of atom i at position \mathbf{r}_i , calculated using Density Derived Electrostatic and Chemical (DDEC6) charge analysis.

$$\sigma = \frac{1}{k_B T V} \lim_{t \rightarrow \infty} \frac{1}{2t} \left\langle \left(\sum_{i=1}^N q_i \mathbf{r}_i(t) - \sum_{i=1}^N q_i \mathbf{r}_i(0) \right)^2 \right\rangle \quad \text{Eq. 43}$$

The ionic conductivity of P2-Na_{2/3}[Ni_{1/3}Ti_{2/3}]O₂ and O3-Na_{0.83}[Ni_{0.42}Ti_{0.58}]O₂ are calculated and compared to results from other studies in Figure 43. For P2-Na_{2/3}[Ni_{1/3}Ti_{2/3}]O₂, results from NN-IP showed the in-plane ionic conductivity in the range of 0.1 to 1 S/cm from 500 to 1200 K, with an activation energy of 0.22 ± 0.01 eV. Both conductivity values and activation energy for P2-Na_{2/3}[Ni_{1/3}Ti_{2/3}]O₂ showed a good match with the experimental results. O3-Na_{0.83}[Ni_{0.42}Ti_{0.58}]O₂ showed slightly lower ionic conductivities with P2-Na_{2/3}[Ni_{1/3}Ti_{2/3}]O₂ and

higher activation energy of 0.26 eV, following the same trend as in diffusion. Compared to experimental data from other studies, the NN-IP gives an overestimation of the conductivity value and an underestimation of the activation energy.

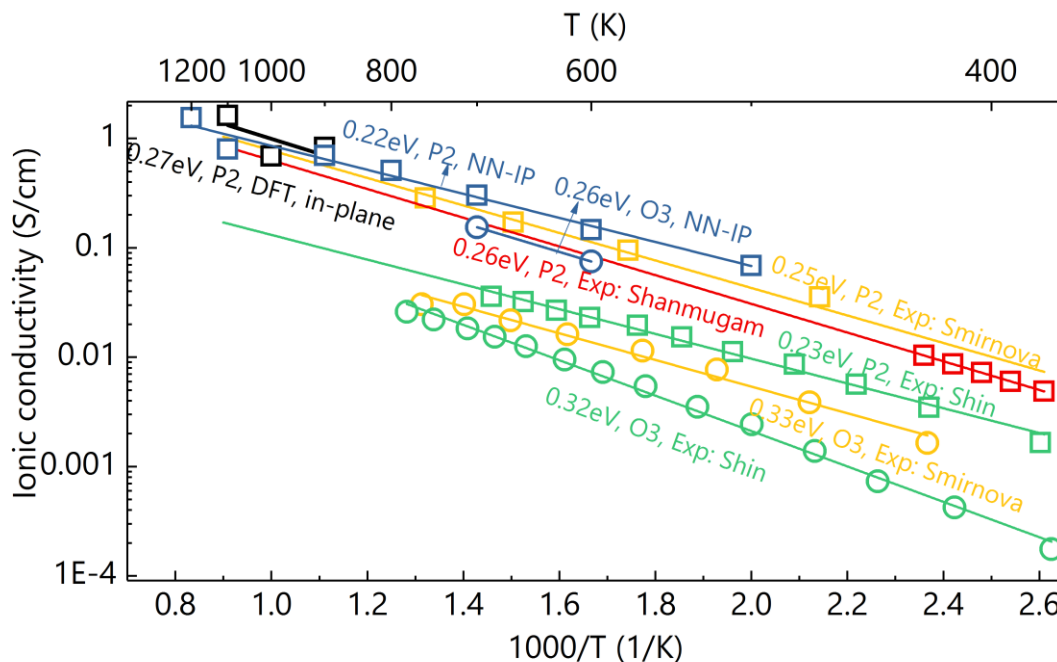


Figure 43: Calculated in-plane ionic conductivity of P2- $\text{Na}_{2/3}[\text{Ni}_{1/3}\text{Ti}_{2/3}]\text{O}_2$ (blue squares) and O3- $\text{Na}_{0.83}[\text{Ni}_{0.42}\text{Ti}_{0.58}]\text{O}_2$ (blue circles) from IP-NN based MD simulations compared with results from DFT-MD (black) and experimental data for P2- $\text{Na}_{2/3}[\text{Ni}_{1/3}\text{Ti}_{2/3}]\text{O}_2$ and O3- $\text{Na}_{0.8}[\text{Ni}_{0.4}\text{Ti}_{0.6}]\text{O}_2$ from Shanmugam et al.¹⁰⁴ (red), Shin et al.¹⁰³ (green), and Smirnova et al.²⁰⁰ (yellow). Results for P2 and O3 structures are represented as squares and circles respectively.

6.5 Conclusions

In this chapter, an NN potential is constructed with energies and forces from DFT calculations for P2 and O3-type $\text{Na}_x[\text{Ni}_y\text{Ti}_{1-y}]\text{O}_2$. The reliability of the NN potential is confirmed with low RMSE of energies and forces as well as a good match in lattice parameters and thermal expansion coefficient with other studies. MD simulations were performed based on the NN potential to investigate the diffusion and ionic conduction in P2-type $\text{Na}_{2/3}[\text{Ni}_{1/3}\text{Ti}_{2/3}]\text{O}_2$ and O3-

type $\text{Na}_{0.83}[\text{Ni}_{0.42}\text{Ti}_{0.58}]\text{O}_2$. The calculated Na diffusivity in P2- $\text{Na}_{2/3}[\text{Ni}_{1/3}\text{Ti}_{2/3}]\text{O}_2$ is in the range of 3×10^{-7} to 2×10^{-5} cm^2/s from 500 to 1200K. A lower Na diffusivity and higher activation energy (0.35 eV) were observed in O3- $\text{Na}_{0.83}[\text{Ni}_{0.42}\text{Ti}_{0.58}]\text{O}_2$ than P2-type $\text{Na}_{2/3}[\text{Ni}_{1/3}\text{Ti}_{2/3}]\text{O}_2$ (0.32eV). P2- $\text{Na}_{2/3}[\text{Ni}_{1/3}\text{Ti}_{2/3}]\text{O}_2$ showed the in-plane ionic conductivity in the range of 0.1 to 1 S/cm from 500 to 1200 K, with an activation energy of 0.22 eV, consistent with other experimental studies. O3- $\text{Na}_{0.83}[\text{Ni}_{0.42}\text{Ti}_{0.58}]\text{O}_2$ showed slightly lower ionic conductivities and higher activation energy of 0.26 eV compared to P2- $\text{Na}_{2/3}[\text{Ni}_{1/3}\text{Ti}_{2/3}]\text{O}_2$, following the same trend as in diffusion.

CHAPTER 7 Conclusions and future work

7.1 Conclusions

In this thesis, we investigated the properties of $\text{Na}_{2x}[\text{Ni}_x\text{Ti}_{1-x}]\text{O}_2$ as bi-functional electrode materials for sodium-ion batteries using a combination of computational and experimental techniques. Firstly, the average and local structural properties and energetics of atomic distribution in $\text{P2-Na}_{2/3}[\text{Ni}_{1/3}\text{Ti}_{2/3}]\text{O}_2$ were investigated using Rietveld refinement on neutron diffraction datasets and atomistic simulations based on the Buckingham and Morse IP models. The calculated average structure showed a good agreement with the experiment results, where the face-sharing sites have lower occupancy compared with edge-sharing sites. In addition, the nuclear density spots of Na showed an elongation within the ab plane, suggesting an anisotropic atomic displacement in sodium motion along the ab plane, possibly caused by the repulsion from the transition metal oxide layer. It was found that it is energy favorable to have an equal distribution of Na and transition metal in each of the two layers in the unit cell, which provides insights on the determination of the representative structures for the simulations.

With in-depth understandings of the structure of $\text{P2-Na}_{2/3}[\text{Ni}_{1/3}\text{Ti}_{2/3}]\text{O}_2$, the atomic and electronic structure changes during cycling were studied based on DFT calculations. Structural evolutions during electrochemical processes were studied using DFT-based MD simulations. It was found that the insertion of sodium would lead to expansion of the ab plane and contraction of the c axis. On the other hand, the extraction of sodium brought in small structural changes. Electronic properties including the electron density distribution, the atomic charge, and density of states were analyzed using DFT, all leading to the same conclusion that Ni and Ti are the major redox-active ion during Na extraction and insertion, respectively, with O also participating in the

redox reaction all the way. A higher in-plane electronic conductivity was observed compared to the through-plane one, with both increasing when either inserting or extracting Na ions.

The diffusion mechanism and ionic conduction in $\text{P2 Na}_{2/3}[\text{Ni}_{1/3}\text{Ti}_{2/3}]\text{O}_2$ using a combination of QENS experiments and MD simulations. Firstly, based on the Q-dependence of the quasi-elastic broadening in QENS measurement, the localized Na ion diffusion behavior can be described by the Singwi-Sjölander jump model. The extracted average jump lengths are around 1.3~1.8 Å at 450~700 K, corresponding to the distance between the neighboring edge-share and face-share sites. This is also consistent with the diffusion mechanism revealed by the density maps from MD simulations: 2D local jumps occur between the edge-share and face-share Na sites. More frequent and longer jumps were observed at higher temperatures. For long-range diffusivity, Fick's model was applied to compare with the MD simulation results where $Q \rightarrow 0$. The QENS showed a Fickian diffusivity in the order of $\sim 10^{-6} \text{ cm}^2/\text{s}$ from 450 to 700 K with $E_a = 0.15 \text{ eV}$.

The MD simulations based on a polarizable interatomic potential model showed an in-plane Na self Fickian diffusivity in a range of $10^{-6} \sim 10^{-5} \text{ cm}^2/\text{s}$ from 900 to 1200 K in $\text{P2 Na}_{2/3}[\text{Ni}_{1/3}\text{Ti}_{2/3}]\text{O}_2$, with an activation energy of $0.53 \pm 0.02 \text{ eV}$. The MD simulations based on DFT calculations gave an in-plane diffusivity of $\sim 10^{-5} \text{ cm}^2/\text{s}$ with $E_a = 0.20 \pm 0.02 \text{ eV}$ in the temperature range of 900 to 1100 K, which showed a better consistency with experimental results. The diffusion coefficients were calculated for different compositions with the Na concentration x in the range of 5/9 to 7/9 based on first-principles MD simulations. Faster diffusion was observed for compositions with less sodium, i.e., more vacancies. The in-plane ionic conductivity calculated using the polarizable IP-based MD for 900 to 1200 K, showed a range of 0.4~1.4 S/cm, with an activation energy of $0.37 \pm 0.03 \text{ eV}$, which is slightly higher than experimental results. The first principles MD simulations showed in-plane ionic conductivity values $\sim 1 \text{ S/cm}$ at 900 to 1100 K

with an activation energy of 0.27 eV, which is in better consistency with experimental measurements in previous studies. Both Na-deficient phase $\text{Na}_{5/9}[\text{Ni}_{1/3}\text{Ti}_{2/3}]\text{O}_2$ and Na-rich phase $\text{Na}_{7/9}[\text{Ni}_{1/3}\text{Ti}_{2/3}]\text{O}_2$ showed higher ionic conductivity compared to the pristine phase.

Machine learning interatomic potentials were constructed for P2 and O3 $\text{Na}_{2x}[\text{Ni}_x\text{Ti}_{1-x}]\text{O}_2$. MD simulations based on neural network interatomic potentials were performed for P2-type $\text{Na}_{2/3}[\text{Ni}_{1/3}\text{Ti}_{2/3}]\text{O}_2$ and O3-type $\text{Na}_{0.83}[\text{Ni}_{0.42}\text{Ti}_{0.58}]\text{O}_2$. The calculated Na diffusivity in P2- $\text{Na}_{2/3}[\text{Ni}_{1/3}\text{Ti}_{2/3}]\text{O}_2$ is in the range of 3×10^{-7} to 2×10^{-5} cm^2/s from 500 to 1200K, with an activation energy of 0.32 eV. A lower Na diffusivity and higher activation energy of 0.35 eV were observed in O3- $\text{Na}_{0.83}[\text{Ni}_{0.42}\text{Ti}_{0.58}]\text{O}_2$. The in-plane ionic conductivity of P2- $\text{Na}_{2/3}[\text{Ni}_{1/3}\text{Ti}_{2/3}]\text{O}_2$ is 0.1 to 1 S/cm from 500 to 1200 K, with an activation energy of 0.22 eV, consistent with other experimental studies. O3- $\text{Na}_{0.83}[\text{Ni}_{0.42}\text{Ti}_{0.58}]\text{O}_2$ showed slightly lower ionic conductivities and higher activation energy of 0.26 eV compared to P2- $\text{Na}_{2/3}[\text{Ni}_{1/3}\text{Ti}_{2/3}]\text{O}_2$, following the same trend as in diffusion.

The above findings not only provided us fundamental understandings of properties and underlying mechanisms in the $\text{Na}_{2x}[\text{Ni}_x\text{Ti}_{1-x}]\text{O}_2$ series, but also can be extended to other systems and shed light on the design and improvement of electrode materials for sodium-ion batteries in the future. The analysis of the active redox pairs upon the insertion and extraction showed that the activation of different redox couples can affect the structural stability and electronic conductivities and essentially the stability and rate performance of the battery. These findings can provide insights on the selection of transition metal redox pairs when designing electrode materials, especially for bi-functional electrode materials when different redox reactions are involved in the charge and discharge process. The comparative study on P2 and O3 type $\text{Na}_{2x}[\text{Ni}_x\text{Ti}_{1-x}]\text{O}_2$ showed higher Na diffusivity and ionic conductivity in the P2 system, suggesting P2 materials are better choices for electrode materials over O3 materials in terms of rate capabilities. However, the

diffusivity in P2 materials would decrease with more sodium ions in the composition. While higher capacities are typically promised by O3 systems or P2 systems with higher sodium content which possess more sodium ions in the structure, a tradeoff between rate performance and capacity needs to be considered when choosing the right electrode material for practical applications.

7.2 Future work

The comprehensive investigation on $\text{Na}_{2x}[\text{Ni}_x\text{Ti}_{1-x}]\text{O}_2$ as bi-functional electrode materials in this thesis has provided us a better understanding of this group of materials and provide atomic-level insights on our future study of similar layered compounds and further exploration and design of the sodium electrode with better performance. In this thesis, we studied the structural properties, electronic properties, and dynamic properties for $\text{Na}_{2x}[\text{Ni}_x\text{Ti}_{1-x}]\text{O}_2$. However, there is still much future work we can do based on the current work to fully realize the potential of not only this materials series but also sodium-ion batteries. For instance, we were not able to identify the O2 phase for $\text{Na}_{2/3}[\text{Ni}_{1/3}\text{Ti}_{2/3}]\text{O}_2$ from the neutron diffraction experiments but observed it in our static energy calculations based on the Morse potential model. While we didn't observe a P2-O2 phase transition in the sodium content range studies in this thesis, it may still occur at lower sodium contents as in other similar compounds like $\text{Na}_{2/3}[\text{Ni}_{1/3}\text{Mn}_{2/3}]\text{O}_2$ ¹⁷⁶ and $\text{Na}_{0.7}\text{Fe}_{0.4}\text{Mn}_{0.4}\text{Co}_{0.2}\text{O}_2$ ¹⁷⁷. This can be verified by experimental techniques like diffraction studies, scanning transmission electron microscopy as well as computational techniques. The redox activities and electronic structures studied in this thesis can be supported by investigations through experiments such as X-ray absorption spectroscopic (XAS) techniques, X-ray photoelectron spectroscopy (XPS), and resonant inelastic X-ray scattering (RIXS). In this thesis, both classical and first principles MD simulations were performed at high temperatures to investigate the dynamic properties with the results compared to experiments conducted at low temperatures. The classical MD simulations

relying on the parametric potential energy surface are less accurate as it tends to neglect the underlying electronic origin of the interactions, while the high cost of first principles simulations have limited their applications for systems with small number of atoms and time scale thus may lead to insufficient diffusion statistics at low temperature. To probe the dynamics at low temperature and bridge the gap between computational and experimental results, besides developing potential models with high accuracy and low cost, efforts can also be made to accelerate the dynamics using methods like enhanced sampling, bias potentials, parallel replica methods, and kinetic Monte Carlo simulations.

Besides the bulk properties of electrodes, the interfaces, such as the grain boundaries and electrode/electrolyte interfaces, especially the ion and electron transport at these interfaces are critical for the performance of the overall battery system. The diffusion pathways, the conduction mechanism, and activation energy can be completely different at the grain boundaries, which needs further examination. It is also important to understand how the electrode materials studied in this thesis interact with the common liquid electrolyte materials like NaClO₄, NaPF₆, NaFSI, NaBF₄, and solid-state electrolytes like Na₃PS₄, Na₃Zr₂Si₂PO₁₂ in practical use. By modeling these solid/liquid or solid/solid interfaces we can gain a better understanding of the complex transport processes and reaction mechanisms at these interfaces and improve the rate performance.

Finally, based on the in-depth understanding of Na_{2x}[Ni_xTi_{1-x}]O₂ obtained in this thesis, the analysis can be extended to other similar layered compounds like this, for example with partial substitution of the elements in this system. The introduction of active elements such as Fe and Mn can bring higher capability while introducing a small amount of inactive elements Li, Mg, Al, Mn into the transition metal layer can improve the overall structural stability^{38,213-215}. Such substitution of other elements may create complex local structural features in the transition metal layers and

affect the ion dynamics, which requires further investigation. With a large amount of different transition metals combinations in this type of layered materials, the promising candidates may be screened with the help of high-throughput simulations combining machine learning techniques with increasing computation powers.

BIBLIOGRAPHY

BIBLIOGRAPHY

- (1) B. Dunn, H. Kamath, and J.-M. Tarascon "Electrical Energy Storage for the Grid: A Battery of Choices," *Science* **2011**, 334, 928-935. <http://dx.doi.org/10.1126/science.1212741>
- (2) D. Larcher and J. M. Tarascon "Towards greener and more sustainable batteries for electrical energy storage," *Nat Chem* **2015**, 7, 19-29. <http://dx.doi.org/10.1038/nchem.2085>
- (3) Y. Nishi "Lithium ion secondary batteries; Past 10 years and the future," *J Power Sources* **2001**, 100, 101-106. [http://dx.doi.org/10.1016/S0378-7753\(01\)00887-4](http://dx.doi.org/10.1016/S0378-7753(01)00887-4)
- (4) J.-M. Tarascon "Is lithium the new gold?," *Nature Chemistry* **2010**, 2, 510-510. <http://dx.doi.org/10.1038/nchem.680>
- (5) W. Tahil "the Trouble with Lithium: Implications of future PHEV production on lithium demand," *Meridian International Research* **2007**.
- (6) T. C. Wanger "The Lithium future-resources, recycling, and the environment," *Conservation Letters* **2011**, 4, 202-206. <http://dx.doi.org/10.1111/j.1755-263X.2011.00166.x>
- (7) P. W. Gruber, P. A. Medina, G. A. Keoleian, S. E. Kesler, M. P. Everson, and T. J. Wallington "Global Lithium Availability," *Journal of Industrial Ecology* **2011**, 15, 760-775. <http://dx.doi.org/10.1111/j.1530-9290.2011.00359.x>
- (8) J. Coetzer "A new high energy density battery system," *J Power Sources* **1986**, 18, 377-380. [http://dx.doi.org/10.1016/0378-7753\(86\)80093-3](http://dx.doi.org/10.1016/0378-7753(86)80093-3)
- (9) G. H. Newman and L. P. Klemann "Ambient Temperature Cycling of an Na - TiS₂ Cell," *Journal of The Electrochemical Society* **1980**, 127, 2097-2097. <http://dx.doi.org/10.1149/1.2129353>
- (10) A. S. Nagelberg and W. L. Worrell "A thermodynamic study of sodium-intercalated TaS₂ and TiS₂," *J Solid State Chem* **1979**, 29, 345-354. [http://dx.doi.org/10.1016/0022-4596\(79\)90191-9](http://dx.doi.org/10.1016/0022-4596(79)90191-9)
- (11) J. M. Tarascon and M. Armand "Issues and challenges facing rechargeable lithium batteries," *Nature* **2001**, 414, 359-367. <http://dx.doi.org/10.1038/35104644>
- (12) C. Vaalma, D. Buchholz, M. Weil, and S. Passerini "A cost and resource analysis of sodium-ion batteries," *Nat Rev Mater* **2018**, 3. <http://dx.doi.org/10.1038/natrevmats.2018.13>
- (13) T. Liu, Y. Zhang, Z. Jiang, X. Zeng, J. Ji, Z. Li, X. Gao, M. Sun, Z. Lin, M. Ling, J. Zheng, and C. Liang "Exploring competitive features of stationary sodium ion batteries for electrochemical energy storage," *Energy & Environmental Science* **2019**, 12, 1512-1533. <http://dx.doi.org/10.1039/C8EE03727B>

- (14) B. L. Ellis and L. F. Nazar "Sodium and sodium-ion energy storage batteries," *Current Opinion in Solid State and Materials Science* **2012**, *16*, 168-177. <http://dx.doi.org/10.1016/j.cossms.2012.04.002>
- (15) M. D. Slater, D. Kim, E. Lee, and C. S. Johnson "Sodium-Ion Batteries," *Advanced Functional Materials* **2013**, *23*, 947-958. <http://dx.doi.org/10.1002/adfm.201200691>
- (16) V. Palomares, P. Serras, I. Villaluenga, K. B. Hueso, J. Carretero-González, and T. Rojo "Na-ion batteries, recent advances and present challenges to become low cost energy storage systems," *Energy & Environmental Science* **2012**, *5*, 5884. <http://dx.doi.org/10.1039/c2ee02781j>
- (17) H. Pan, Y.-S. Hu, and L. Chen "Room-temperature stationary sodium-ion batteries for large-scale electric energy storage," *Energy & Environmental Science* **2013**, *6*, 2338-2338. <http://dx.doi.org/10.1039/c3ee40847g>
- (18) C. Grosjean, P. H. Miranda, M. Perrin, and P. Poggi "Assessment of world lithium resources and consequences of their geographic distribution on the expected development of the electric vehicle industry," *Renewable and Sustainable Energy Reviews* **2012**, *16*, 1735-1744. <http://dx.doi.org/10.1016/j.rser.2011.11.023>
- (19) *Mineral commodity summaries 2020*, 2020.
- (20) S. P. Ong, V. L. Chevrier, G. Hautier, A. Jain, C. Moore, S. Kim, X. Ma, and G. Ceder "Voltage, stability and diffusion barrier differences between sodium-ion and lithium-ion intercalation materials," *Energy & Environmental Science* **2011**, *4*, 3680. <http://dx.doi.org/10.1039/c1ee01782a>
- (21) E. J. Wu, P. D. Tepesch, and G. Ceder "Size and charge effects on the structural stability of LiMO₂ (M = transition metal) compounds," *Philosophical Magazine B* **1998**, *77*, 1039-1047. <http://dx.doi.org/10.1080/13642819808206403>
- (22) R. J. Clément, P. G. Bruce, and C. P. Grey "Review-Manganese-Based P2-Type Transition Metal Oxides as Sodium-Ion Battery Cathode Materials," *Journal of the Electrochemical Society* **2015**, *162*, A2589-A2604. <http://dx.doi.org/10.1149/2.0201514jes>
- (23) M. H. Han, E. Gonzalo, G. Singh, and T. Rojo "A comprehensive review of sodium layered oxides: powerful cathodes for Na-ion batteries," *Energy & Environmental Science* **2015**, *8*, 81-102. <http://dx.doi.org/10.1039/c4ee03192j>
- (24) K. Zhang, D. Kim, Z. Hu, M. Park, G. Noh, Y. Yang, J. Zhang, V. W.-h. Lau, S.-L. Chou, M. Cho, S.-Y. Choi, and Y.-M. Kang "Manganese based layered oxides with modulated electronic and thermodynamic properties for sodium ion batteries," *Nat Commun* **2019**, *10*. <http://dx.doi.org/10.1038/s41467-018-07646-4>
- (25) S.-W. Kim, D.-H. Seo, X. Ma, G. Ceder, and K. Kang "Electrode Materials for Rechargeable Sodium-Ion Batteries: Potential Alternatives to Current Lithium-Ion Batteries," *Advanced Energy Materials* **2012**, *2*, 710-721. <http://dx.doi.org/10.1002/aenm.201200026>

- (26) S. Kim, X. Ma, S. P. Ong, and G. Ceder "A comparison of destabilization mechanisms of the layered Na_xMO_2 and Li_xMO_2 compounds upon alkali de-intercalation," *Physical Chemistry Chemical Physics* **2012**, *14*, 15571. <http://dx.doi.org/10.1039/c2cp43377j>
- (27) C. Delmas, C. Fouassier, and P. Hagenmuller "Structural Classification and Properties of the Layered Oxides," *Physica B & C* **1980**, *99*, 81-85. [http://dx.doi.org/10.1016/0378-4363\(80\)90214-4](http://dx.doi.org/10.1016/0378-4363(80)90214-4)
- (28) C. Delmas, J. Braconnier, C. Fouassier, and P. Hagenmuller "Electrochemical Intercalation of Sodium in Na_xCoO_2 Bronzes," *Solid State Ionics* **1981**, *3-4*, 165-169. [http://dx.doi.org/10.1016/0167-2738\(81\)90076-X](http://dx.doi.org/10.1016/0167-2738(81)90076-X)
- (29) E. Lee, D. E. Brown, E. E. Alp, Y. Ren, J. Lu, J. J. Woo, and C. S. Johnson "New Insights into the Performance Degradation of Fe-Based Layered Oxides in Sodium-Ion Batteries: Instability of $\text{Fe}^{3+}/\text{Fe}^{4+}$ Redox in $\alpha\text{-NaFeO}_2$," *Chemistry of Materials* **2015**, *27*, 6755-6764. <http://dx.doi.org/10.1021/acs.chemmater.5b02918>
- (30) S. Guo, P. Liu, H. Yu, Y. Zhu, M. Chen, M. Ishida, and H. Zhou "A Layered P2- and O3-Type Composite as a High-Energy Cathode for Rechargeable Sodium-Ion Batteries," *Angew Chem-Ger Edit* **2015**, *127*, 5992-5997. <http://dx.doi.org/10.1002/ange.201411788>
- (31) Y. C. Lei, X. Li, L. Liu, and G. Ceder "Synthesis and Stoichiometry of Different Layered Sodium Cobalt Oxides," *Chemistry of Materials* **2014**, *26*, 5288-5296. <http://dx.doi.org/10.1021/cm5021788>
- (32) S. Guo, Y. Sun, J. Yi, K. Zhu, P. Liu, Y. Zhu, G.-z. Zhu, M. Chen, M. Ishida, and H. Zhou "Understanding sodium-ion diffusion in layered P2 and P3 oxides via experiments and first-principles calculations: a bridge between crystal structure and electrochemical performance," *NPG Asia Materials* **2016**, *8*, e266-e266. <http://dx.doi.org/10.1038/am.2016.53>
- (33) Y. F. Mo, S. P. Ong, and G. Ceder "Insights into Diffusion Mechanisms in P2 Layered Oxide Materials by First-Principles Calculations," *Chemistry of Materials* **2014**, *26*, 5208-5214. <http://dx.doi.org/10.1021/cm501563f>
- (34) L. W. Shacklette, T. R. Jow, and L. Townsend "Rechargeable Electrodes from Sodium Cobalt Bronzes," *Journal of The Electrochemical Society* **1988**, *135*, 2669-2674. <http://dx.doi.org/10.1149/1.2095407>
- (35) R. Berthelot, D. Carlier, and C. Delmas "Electrochemical investigation of the P2– Na_xCoO_2 phase diagram," *Nat Mater* **2010**, *10*, 74-80. <http://dx.doi.org/10.1038/nmat2920>
- (36) X. Ma, H. Chen, and G. Ceder "Electrochemical Properties of Monoclinic NaMnO_2 ," *Journal of The Electrochemical Society* **2011**, *158*, A1307. <http://dx.doi.org/10.1149/2.035112jes>
- (37) A. Caballero, L. Hernán, J. Morales, L. Sánchez, J. Santos Peña, and M. A. G. Aranda "Synthesis and characterization of high-temperature hexagonal P2- $\text{Na}_{0.6}\text{MnO}_2$ and its

electrochemical behaviour as cathode in sodium cells," *Journal of Materials Chemistry* **2002**, *12*, 1142-1147. <http://dx.doi.org/10.1039/b108830k>

(38) J. Billaud, G. Singh, A. R. Armstrong, E. Gonzalo, V. Roddatis, M. Armand, T. Rojob, and P. G. Bruce "Na_{0.67}Mn_{1-x}Mg_xO₂ (0 ≤ x ≤ 0.2): a high capacity cathode for sodium-ion batteries," *Energy & Environmental Science* **2014**, *7*, 1387-1391. <http://dx.doi.org/10.1039/c4ee00465e>

(39) C. Zheng, B. Radhakrishnan, I. H. Chu, Z. B. Wang, and S. P. Ong "Effects of Transition-Metal Mixing on Na Ordering and Kinetics in Layered P2 Oxides," *Phys Rev Appl* **2017**, *7*. <http://dx.doi.org/10.1103/PhysRevApplied.7.064003>

(40) X. Li, Y. Wang, D. Wu, L. Liu, S.-H. Bo, and G. Ceder "Jahn–Teller Assisted Na Diffusion for High Performance Na Ion Batteries," *Chemistry of Materials* **2016**, *28*, 6575-6583. <http://dx.doi.org/10.1021/acs.chemmater.6b02440>

(41) N. Yabuuchi, M. Kajiyama, J. Iwatate, H. Nishikawa, S. Hitomi, R. Okuyama, R. Usui, Y. Yamada, and S. Komaba "P2-type Na-x[Fe_{1/2}Mn_{1/2}]O₂ made from earth-abundant elements for rechargeable Na batteries," *Nat Mater* **2012**, *11*, 512-517. <http://dx.doi.org/10.1038/NMAT3309>

(42) W. M. Dose, N. Sharma, J. C. Pramudita, H. E. A. Brand, E. Gonzalo, and T. Rojo "Structure–Electrochemical Evolution of a Mn-Rich P2 Na_{2/3}Fe_{0.2}Mn_{0.8}O₂ Na-Ion Battery Cathode," *Chemistry of Materials* **2017**, *29*, 7416-7423. <http://dx.doi.org/10.1021/acs.chemmater.7b02397>

(43) N. A. Katcho, J. Carrasco, D. Saurel, E. Gonzalo, M. Han, F. Aguesse, and T. Rojo "Origins of Bistability and Na Ion Mobility Difference in P2- and O3-Na_{2/3}Fe_{2/3}Mn_{1/3}O₂ Cathode Polymorphs," *Advanced Energy Materials* **2017**, *7*, 1601477. <http://dx.doi.org/10.1002/aenm.201601477>

(44) B. Mortemard de Boisse, D. Carlier, M. Guignard, E. Guerin, M. Duttine, A. Wattiaux, and C. Delmas "Influence of Mn/Fe Ratio on Electrochemical and Structural Properties of P2-Na_xMn_{1-y}Fe_yO₂ Phases as Positive Electrode Material for Na-Ion Batteries," *Chemistry of Materials* **2018**, *30*, 7672-7681. <http://dx.doi.org/10.1021/acs.chemmater.8b02953>

(45) U. Maitra, R. A. House, J. W. Somerville, N. Tapia-Ruiz, J. G. Lozano, N. Guerrini, R. Hao, K. Luo, L. Jin, M. A. Pérez-Osorio, F. Massel, D. M. Pickup, S. Ramos, X. Lu, D. E. McNally, A. V. Chadwick, F. Giustino, T. Schmitt, L. C. Duda, M. R. Roberts, and P. G. Bruce "Oxygen redox chemistry without excess alkali-metal ions in Na_{2/3}[Mg_{0.28}Mn_{0.72}]O₂," *Nature Chemistry* **2018**, *10*, 288-295. <http://dx.doi.org/10.1038/nchem.2923>

(46) B. Song, E. Hu, J. Liu, Y. Zhang, X.-Q. Yang, J. Nanda, A. Huq, and K. Page "A novel P3-type Na_{2/3}Mg_{1/3}Mn_{2/3}O₂ as high capacity sodium-ion cathode using reversible oxygen redox," *J Mater Chem A* **2019**, *7*, 1491-1498. <http://dx.doi.org/10.1039/c8ta09422e>

- (47) S. Komaba, N. Yabuuchi, T. Nakayama, A. Ogata, T. Ishikawa, and I. Nakai "Study on the Reversible Electrode Reaction of $\text{Na}_{1-x}\text{Ni}_{0.5}\text{Mn}_{0.5}\text{O}_2$ for a Rechargeable Sodium-Ion Battery," *Inorganic Chemistry* **2012**, *51*, 6211-6220. <http://dx.doi.org/10.1021/ic300357d>
- (48) S. Kumakura, Y. Tahara, S. Sato, K. Kubota, and S. Komaba "P' 2- $\text{Na}_{2/3}\text{Mn}_{0.9}\text{Me}_{0.1}\text{O}_2$ (Me = Mg, Ti, Co, Ni, Cu, and Zn): Correlation between Orthorhombic Distortion and Electrochemical Property," *Chemistry of Materials* **2017**, *29*, 8958-8962. <http://dx.doi.org/10.1021/acs.chemmater.7b02772>
- (49) C. Ma, J. Alvarado, J. Xu, R. J. Clément, M. Kodur, W. Tong, C. P. Grey, and Y. S. Meng "Exploring Oxygen Activity in the High Energy P2-Type $\text{Na}_{0.78}\text{Ni}_{0.23}\text{Mn}_{0.69}\text{O}_2$ Cathode Material for Na-Ion Batteries," *J Am Chem Soc* **2017**, *139*, 4835-4845. <http://dx.doi.org/10.1021/jacs.7b00164>
- (50) M. Sathiya, K. Hemalatha, K. Ramesha, J. M. Tarascon, and A. S. Prakash "Synthesis, Structure, and Electrochemical Properties of the Layered Sodium Insertion Cathode Material: $\text{NaNi}_{1/3}\text{Mn}_{1/3}\text{Co}_{1/3}\text{O}_2$," *Chemistry of Materials* **2012**, *24*, 1846-1853. <http://dx.doi.org/10.1021/cm300466b>
- (51) H. Yoshida, N. Yabuuchi, K. Kubota, I. Ikeuchi, A. Garsuch, M. Schulz-Dobrick, and S. Komaba "P2-type $\text{Na}_{2/3}\text{Ni}_{1/3}\text{Mn}_{2/3-x}\text{Ti}_x\text{O}_2$ as a new positive electrode for higher energy Na-ion batteries," *Chemical Communications* **2014**, *50*, 3677-3680. <http://dx.doi.org/10.1039/c3cc49856e>
- (52) H. Guo, Y. Wang, W. Han, Z. Yu, X. Qi, K. Sun, Y.-S. Hu, Y. Liu, D. Chen, and L. Chen "Na-deficient O3-type cathode material $\text{Na}_{0.8}[\text{Ni}_{0.3}\text{Co}_{0.2}\text{Ti}_{0.5}]\text{O}_2$ for room-temperature sodium-ion batteries," *Electrochimica Acta* **2015**, *158*, 258-263. <http://dx.doi.org/10.1016/j.electacta.2015.01.118>
- (53) G. Singh, F. Aguesse, L. Otaegui, E. Goikolea, E. Gonzalo, J. Segalini, and T. Rojo "Electrochemical performance of $\text{NaFe}(\text{Ni}_{0.5}\text{Ti}_{0.5})_{1-x}\text{O}_2$ ($x = 0.2$ and $x = 0.4$) cathode for sodium-ion battery," *J Power Sources* **2015**, *273*, 333-339. <http://dx.doi.org/10.1016/j.jpowsour.2014.09.050>
- (54) G. Venkatesh, B. Kishore, R. Viswanatha, D. Aurbach, and N. Munichandraiah "P2-Type $\text{Na}_{0.67}\text{Mn}_{0.65}\text{Fe}_{0.20}\text{Ni}_{0.15}\text{O}_2$ Microspheres as a Positive Electrode Material with a Promising Electrochemical Performance for Na-Ion Batteries," *Journal of The Electrochemical Society* **2017**, *164*, A2176-A2182. <http://dx.doi.org/10.1149/2.1661709jes>
- (55) C. Masquelier and L. Croguennec "Polyanionic (Phosphates, Silicates, Sulfates) Frameworks as Electrode Materials for Rechargeable Li (or Na) Batteries," *Chem Rev* **2013**, *113*, 6552-6591. <http://dx.doi.org/10.1021/cr3001862>
- (56) A. K. Padhi, K. S. Nanjundaswamy, and J. B. Goodenough "Phospho-olivines as Positive - Electrode Materials for Rechargeable Lithium Batteries," *Journal of The Electrochemical Society* **2019**, *144*, 1188-1194. <http://dx.doi.org/10.1149/1.1837571>

- (57) P. Moreau, D. Guyomard, J. Gaubicher, and F. Boucher "Structure and Stability of Sodium Intercalated Phases in Olivine FePO₄," *Chemistry of Materials* **2010**, *22*, 4126-4128. <http://dx.doi.org/10.1021/cm101377h>
- (58) G. Ali, J.-H. Lee, D. Susanto, S.-W. Choi, B. W. Cho, K.-W. Nam, and K. Y. Chung "Polythiophene-Wrapped Olivine NaFePO₄ as a Cathode for Na-Ion Batteries," *Acs Appl Mater Inter* **2016**, *8*, 15422-15429. <http://dx.doi.org/10.1021/acsami.6b04014>
- (59) Z. Jian, W. Han, X. Lu, H. Yang, Y.-S. Hu, J. Zhou, Z. Zhou, J. Li, W. Chen, D. Chen, and L. Chen "Superior Electrochemical Performance and Storage Mechanism of Na₃V₂(PO₄)₃Cathode for Room-Temperature Sodium-Ion Batteries," *Advanced Energy Materials* **2013**, *3*, 156-160. <http://dx.doi.org/10.1002/aenm.201200558>
- (60) Y. Fang, L. Xiao, X. Ai, Y. Cao, and H. Yang "Hierarchical Carbon Framework Wrapped Na₃V₂(PO₄)₃as a Superior High-Rate and Extended Lifespan Cathode for Sodium-Ion Batteries," *Advanced Materials* **2015**, *27*, 5895-5900. <http://dx.doi.org/10.1002/adma.201502018>
- (61) X. Rui, W. Sun, C. Wu, Y. Yu, and Q. Yan "An Advanced Sodium-Ion Battery Composed of Carbon Coated Na₃V₂(PO₄)₃in a Porous Graphene Network," *Advanced Materials* **2015**, *27*, 6670-6676. <http://dx.doi.org/10.1002/adma.201502864>
- (62) B. L. Ellis, W. R. M. Makahnouk, Y. Makimura, K. Toghill, and L. F. Nazar "A multifunctional 3.5 V iron-based phosphate cathode for rechargeable batteries," *Nat Mater* **2007**, *6*, 749-753. <http://dx.doi.org/10.1038/nmat2007>
- (63) I. D. Gocheva, M. Nishijima, T. Doi, S. Okada, J.-i. Yamaki, and T. Nishida "Mechanochemical synthesis of NaMF₃ (M=Fe, Mn, Ni) and their electrochemical properties as positive electrode materials for sodium batteries," *J Power Sources* **2009**, *187*, 247-252. <http://dx.doi.org/10.1016/j.jpowsour.2008.10.110>
- (64) A. Kitajou, H. Komatsu, K. Chihara, I. D. Gocheva, S. Okada, and J.-i. Yamaki "Novel synthesis and electrochemical properties of perovskite-type NaFeF₃ for a sodium-ion battery," *J Power Sources* **2012**, *198*, 389-392. <http://dx.doi.org/10.1016/j.jpowsour.2011.09.064>
- (65) M. Nishijima, I. D. Gocheva, S. Okada, T. Doi, J.-i. Yamaki, and T. Nishida "Cathode properties of metal trifluorides in Li and Na secondary batteries," *J Power Sources* **2009**, *190*, 558-562. <http://dx.doi.org/10.1016/j.jpowsour.2009.01.051>
- (66) Y. Shen, X. Wang, H. Hu, M. Jiang, X. Yang, and H. Shu "A graphene loading heterogeneous hydrated forms iron based fluoride nanocomposite as novel and high-capacity cathode material for lithium/sodium ion batteries," *J Power Sources* **2015**, *283*, 204-210. <http://dx.doi.org/10.1016/j.jpowsour.2015.02.097>
- (67) Y. You, X.-L. Wu, Y.-X. Yin, and Y.-G. Guo "High-quality Prussian blue crystals as superior cathode materials for room-temperature sodium-ion batteries," *Energy Environ. Sci.* **2014**, *7*, 1643-1647. <http://dx.doi.org/10.1039/c3ee44004d>

- (68) H.-W. Lee, R. Y. Wang, M. Pasta, S. Woo Lee, N. Liu, and Y. Cui "Manganese hexacyanomanganate open framework as a high-capacity positive electrode material for sodium-ion batteries," *Nat Commun* **2014**, *5*. <http://dx.doi.org/10.1038/ncomms6280>
- (69) H. Lee, Y.-I. Kim, J.-K. Park, and J. W. Choi "Sodium zinc hexacyanoferrate with a well-defined open framework as a positive electrode for sodium ion batteries," *Chemical Communications* **2012**, *48*, 8416. <http://dx.doi.org/10.1039/c2cc33771a>
- (70) J. Song, L. Wang, Y. Lu, J. Liu, B. Guo, P. Xiao, J.-J. Lee, X.-Q. Yang, G. Henkelman, and J. B. Goodenough "Removal of Interstitial H₂O in Hexacyanometallates for a Superior Cathode of a Sodium-Ion Battery," *J Am Chem Soc* **2015**, *137*, 2658-2664. <http://dx.doi.org/10.1021/ja512383b>
- (71) M. Lee, J. Hong, J. Lopez, Y. Sun, D. Feng, K. Lim, W. C. Chueh, M. F. Toney, Y. Cui, and Z. Bao "High-performance sodium–organic battery by realizing four-sodium storage in disodium rhodizonate," *Nature Energy* **2017**, *2*, 861-868. <http://dx.doi.org/10.1038/s41560-017-0014-y>
- (72) C. Wang, Y. Xu, Y. Fang, M. Zhou, L. Liang, S. Singh, H. Zhao, A. Schober, and Y. Lei "Extended π -Conjugated System for Fast-Charge and -Discharge Sodium-Ion Batteries," *J Am Chem Soc* **2015**, *137*, 3124-3130. <http://dx.doi.org/10.1021/jacs.5b00336>
- (73) D. A. Stevens and J. R. Dahn "The Mechanisms of Lithium and Sodium Insertion in Carbon Materials," *Journal of The Electrochemical Society* **2001**, *148*, A803. <http://dx.doi.org/10.1149/1.1379565>
- (74) D. A. Stevens and J. R. Dahn "High Capacity Anode Materials for Rechargeable Sodium-Ion Batteries," *Journal of The Electrochemical Society* **2000**, *147*, 1271. <http://dx.doi.org/10.1149/1.1393348>
- (75) S. Komaba, W. Murata, T. Ishikawa, N. Yabuuchi, T. Ozeki, T. Nakayama, A. Ogata, K. Gotoh, and K. Fujiwara "Electrochemical Na Insertion and Solid Electrolyte Interphase for Hard-Carbon Electrodes and Application to Na-Ion Batteries," *Advanced Functional Materials* **2011**, *21*, 3859-3867. <http://dx.doi.org/10.1002/adfm.201100854>
- (76) A. Kamiyama, K. Kubota, D. Igarashi, Y. Youn, Y. Tateyama, H. Ando, K. Gotoh, and S. Komaba "MgO-Template Synthesis of Extremely High Capacity Hard Carbon for Na-Ion Battery," *Angewandte Chemie International Edition* **2021**. <http://dx.doi.org/10.1002/anie.202013951>
- (77) J. Ding, H. Wang, Z. Li, A. Kohandehghan, K. Cui, Z. Xu, B. Zahiri, X. Tan, E. M. Lotfabad, B. C. Olsen, and D. Mitlin "Carbon Nanosheet Frameworks Derived from Peat Moss as High Performance Sodium Ion Battery Anodes," *ACS Nano* **2013**, *7*, 11004-11015. <http://dx.doi.org/10.1021/nn404640c>
- (78) Y. Zhu, X. Han, Y. Xu, Y. Liu, S. Zheng, K. Xu, L. Hu, and C. Wang "Electrospun Sb/C Fibers for a Stable and Fast Sodium-Ion Battery Anode," *ACS Nano* **2013**, *7*, 6378-6386. <http://dx.doi.org/10.1021/nn4025674>

- (79) Y. Jiang, M. Hu, D. Zhang, T. Yuan, W. Sun, B. Xu, and M. Yan "Transition metal oxides for high performance sodium ion battery anodes," *Nano Energy* **2014**, *5*, 60-66. <http://dx.doi.org/10.1016/j.nanoen.2014.02.002>
- (80) Y. Xu, E. Memarzadeh Lotfabad, H. Wang, B. Farbod, Z. Xu, A. Kohandehghan, and D. Mitlin "Nanocrystalline anatase TiO₂: a new anode material for rechargeable sodium ion batteries," *Chemical Communications* **2013**, *49*, 8973. <http://dx.doi.org/10.1039/c3cc45254a>
- (81) P. Senguttuvan, G. Rouse, V. Seznec, J.-M. Tarascon, and M. R. Palacín "Na₂Ti₃O₇: Lowest Voltage Ever Reported Oxide Insertion Electrode for Sodium Ion Batteries," *Chemistry of Materials* **2011**, *23*, 4109-4111. <http://dx.doi.org/10.1021/cm202076g>
- (82) A. Rudola, K. Saravanan, C. W. Mason, and P. Balaya "Na₂Ti₃O₇: an intercalation based anode for sodium-ion battery applications," *J Mater Chem A* **2013**, *1*, 2653-2662. <http://dx.doi.org/10.1039/c2ta01057g>
- (83) D. Wu, X. Li, B. Xu, N. Twu, L. Liu, and G. Ceder "NaTiO₂: a layered anode material for sodium-ion batteries," *Energy & Environmental Science* **2015**, *8*, 195-202. <http://dx.doi.org/10.1039/c4ee03045a>
- (84) Y. Wang, X. Yu, S. Xu, J. Bai, R. Xiao, Y.-S. Hu, H. Li, X.-Q. Yang, L. Chen, and X. Huang "A zero-strain layered metal oxide as the negative electrode for long-life sodium-ion batteries," *Nat Commun* **2013**, *4*. <http://dx.doi.org/10.1038/ncomms3365>
- (85) C. Zhao, M. Avdeev, L. Chen, and Y.-S. Hu "An O₃-type Oxide with Low Sodium Content as the Phase-Transition-Free Anode for Sodium-Ion Batteries," *Angewandte Chemie International Edition* **2018**, *57*, 7056-7060. <http://dx.doi.org/10.1002/anie.201801923>
- (86) S. I. Park, I. Gocheva, S. Okada, and J.-i. Yamaki "Electrochemical Properties of NaTi₂(PO₄)₃ Anode for Rechargeable Aqueous Sodium-Ion Batteries," *Journal of The Electrochemical Society* **2011**, *158*, A1067. <http://dx.doi.org/10.1149/1.3611434>
- (87) C. Kim, K.-Y. Lee, I. Kim, J. Park, G. Cho, K.-W. Kim, J.-H. Ahn, and H.-J. Ahn "Long-term cycling stability of porous Sn anode for sodium-ion batteries," *J Power Sources* **2016**, *317*, 153-158. <http://dx.doi.org/10.1016/j.jpowsour.2016.03.060>
- (88) Y. Xu, E. Swaans, S. Basak, H. W. Zandbergen, D. M. Borsa, and F. M. Mulder "Reversible Na-Ion Uptake in Si Nanoparticles," *Advanced Energy Materials* **2016**, *6*, 1501436. <http://dx.doi.org/10.1002/aenm.201501436>
- (89) Y. Kim, Y. Park, A. Choi, N.-S. Choi, J. Kim, J. Lee, J. H. Ryu, S. M. Oh, and K. T. Lee "An Amorphous Red Phosphorus/Carbon Composite as a Promising Anode Material for Sodium Ion Batteries," *Advanced Materials* **2013**, *25*, 3045-3049. <http://dx.doi.org/10.1002/adma.201204877>
- (90) A. Darwiche, C. Marino, M. T. Sougrati, B. Fraise, L. Stievano, and L. Monconduit "Better Cycling Performances of Bulk Sb in Na-Ion Batteries Compared to Li-Ion

Systems: An Unexpected Electrochemical Mechanism," *J Am Chem Soc* **2012**, *134*, 20805-20811. <http://dx.doi.org/10.1021/ja310347x>

(91) L. Baggetto, J. K. Keum, J. F. Browning, and G. M. Veith "Germanium as negative electrode material for sodium-ion batteries," *Electrochemistry Communications* **2013**, *34*, 41-44. <http://dx.doi.org/10.1016/j.elecom.2013.05.025>

(92) Y. S. Wang, R. J. Xiao, Y. S. Hu, M. Avdeev, and L. Q. Chen "P2-Na-0.6[Cr_{0.6}Ti_{0.4}]O₂ cation-disordered electrode for high-rate symmetric rechargeable sodium-ion batteries," *Nat Commun* **2015**, *6*. <http://dx.doi.org/10.1038/Ncomms7954>

(93) S. Guo, P. Liu, Y. Sun, K. Zhu, J. Yi, M. Chen, M. Ishida, and H. Zhou "A High-Voltage and Ultralong-Life Sodium Full Cell for Stationary Energy Storage," *Angewandte Chemie International Edition* **2015**, *54*, 11701-11705. <http://dx.doi.org/10.1002/anie.201505215>

(94) M. Palanisamy, H. W. Kim, S. Heo, E. Lee, and Y. Kim "Insights into the Dual-Electrode Characteristics of Layered Na_{0.5}Ni_{0.25}Mn_{0.75}O₂ Materials for Sodium-Ion Batteries," *Acs Appl Mater Inter* **2017**, *9*, 10618-10625. <http://dx.doi.org/10.1021/acsami.6b15355>

(95) L. S. Plashnitsa, E. Kobayashi, Y. Noguchi, S. Okada, and J.-i. Yamaki "Performance of NASICON Symmetric Cell with Ionic Liquid Electrolyte," *Journal of The Electrochemical Society* **2010**, *157*, A536. <http://dx.doi.org/10.1149/1.3298903>

(96) S. Li, Y. Dong, L. Xu, X. Xu, L. He, and L. Mai "Effect of Carbon Matrix Dimensions on the Electrochemical Properties of Na₃V₂(PO₄)₃Nanograins for High-Performance Symmetric Sodium-Ion Batteries," *Advanced Materials* **2014**, *26*, 3545-3553. <http://dx.doi.org/10.1002/adma.201305522>

(97) S. Wang, L. Wang, Z. Zhu, Z. Hu, Q. Zhao, and J. Chen "All Organic Sodium-Ion Batteries with Na₄C₈H₂O₆," *Angewandte Chemie International Edition* **2014**, *53*, 5892-5896. <http://dx.doi.org/10.1002/anie.201400032>

(98) R. Shanmugam and W. Lai "Na_{2/3}Ni_{1/3}Ti_{2/3}O₂: "Bi-Functional" Electrode Materials for Na-Ion Batteries," *ECS Electrochemistry Letters* **2014**, *3*, A23-A25. <http://dx.doi.org/10.1149/2.007404eel>

(99) S. H. Guo, H. J. Yu, P. Liu, Y. Ren, T. Zhang, M. W. Chen, M. Ishida, and H. S. Zhou "High-performance symmetric sodium-ion batteries using a new, bipolar O₃-type material, Na_{0.8}Ni_{0.4}Ti_{0.6}O₂," *Energy & Environmental Science* **2015**, *8*, 1237-1244. <http://dx.doi.org/10.1039/c4ee03361b>

(100) Y. Shin "Preparation and structural properties of layer-type oxides Na_xNi_{x/2}Ti_{1-x/2}O₂ (0.60 ≤ x ≤ 1.0)," *Solid State Ionics* **2000**, *132*, 131-141. [http://dx.doi.org/10.1016/S0167-2738\(00\)00691-3](http://dx.doi.org/10.1016/S0167-2738(00)00691-3)

(101) K. Kang, D. Carlier, J. Reed, E. M. Arroyo, G. Ceder, L. Croguennec, and C. Delmas "Synthesis and Electrochemical Properties of Layered Li_{0.9}Ni_{0.45}Ti_{0.55}O₂," *Chemistry of Materials* **2003**, *15*, 4503-4507. <http://dx.doi.org/10.1021/cm034455+>

- (102) H. Yu, S. Guo, Y. Zhu, M. Ishida, and H. Zhou "Novel titanium-based O3-type NaTi_{0.5}Ni_{0.5}O₂ as a cathode material for sodium ion batteries," *Chemical Communications* **2014**, 50, 457-459. <http://dx.doi.org/10.1039/C3CC47351A>
- (103) Y. J. Shin, M. H. Park, J. H. Kwak, H. Namgoong, and O. H. Han "Ionic conduction properties of layer-type oxides (Na_xM_x/2Ti_{1-x}/2O₂)-Ti-II-O-IV (M=Ni, Co; 0.60 ≤ x ≤ 1.0)," *Solid State Ionics* **2002**, 150, 363-372. [http://dx.doi.org/10.1016/S0167-2738\(02\)00451-4](http://dx.doi.org/10.1016/S0167-2738(02)00451-4)
- (104) R. Shanmugam and W. Lai "Study of Transport Properties and Interfacial Kinetics of Na_{2/3} [Ni_{1/3}Mn_xTi_{2/3-x}] O₂ (x= 0, 1/3) as Electrodes for Na-Ion Batteries," *Journal of The Electrochemical Society* **2015**, 162, A8-A14. <http://dx.doi.org/10.1149/2.0201501jes>
- (105) R. Fielden and M. N. Obrovac "Low Voltage Sodium Intercalation in Na_xNi_x/2Ti_{1-x}/2O₂ (0.5 ≤ x ≤ 1.0)," *Journal of The Electrochemical Society* **2014**, 161, A1158-A1163. <http://dx.doi.org/10.1149/2.118406jes>
- (106) S. Maletti, A. Sarapulova, A. Schökel, and D. Mikhailova "Operando Studies on the NaNi_{0.5}Ti_{0.5}O₂ Cathode for Na-Ion Batteries: Elucidating Titanium as a Structure Stabilizer," *Acs Appl Mater Inter* **2019**, 11, 33923-33930. <http://dx.doi.org/10.1021/acsami.9b10352>
- (107) P. Hohenberg and W. Kohn "Inhomogeneous Electron Gas," *Physical Review* **1964**, 136, B864-B871. <http://dx.doi.org/10.1103/PhysRev.136.B864>
- (108) A. Saracibar, J. Carrasco, D. Saurel, M. Galceran, B. Acebedo, H. Anne, M. Lepoitevin, T. Rojo, and M. C. Cabanas "Investigation of sodium insertion-extraction in olivine Na_xFePO₄ (0 ≤ x ≤ 1) using first-principles calculations," *Physical Chemistry Chemical Physics* **2016**, 18, 13045-13051. <http://dx.doi.org/10.1039/c6cp00762g>
- (109) S. M. Wood, C. Eames, E. Kendrick, and M. S. Islam "Sodium Ion Diffusion and Voltage Trends in Phosphates Na₄M₃(PO₄)₂P₂O₇ (M = Fe, Mn, Co, Ni) for Possible High-Rate Cathodes," *The Journal of Physical Chemistry C* **2015**, 119, 15935-15941. <http://dx.doi.org/10.1021/acs.jpcc.5b04648>
- (110) Y. Liao, K.-S. S. Park, P. Xiao, G. Henkelman, W. Li, and J. B. Goodenough "Sodium Intercalation Behavior of Layered Na_xNbS₂ (0 ≤ x ≤ 1)," *Chemistry of Materials* **2013**, 25, 1699-1705. <http://dx.doi.org/10.1021/cm400150u>
- (111) W. Kohn and L. J. Sham "Self-Consistent Equations Including Exchange and Correlation Effects," *Physical Review* **1965**, 140, A1133-A1138. <http://dx.doi.org/10.1103/PhysRev.140.A1133>
- (112) J. P. Perdew, K. Burke, and M. Ernzerhof "Generalized Gradient Approximation Made Simple," *Phys Rev Lett* **1996**, 77, 3865-3868. <http://dx.doi.org/10.1103/PhysRevLett.77.3865>
- (113) J. P. Perdew and Y. Wang "Accurate and simple analytic representation of the electron-gas correlation energy," *Physical Review B* **1992**, 45, 13244-13249. <http://dx.doi.org/10.1103/PhysRevB.45.13244>

- (114) A. D. Becke "Density-functional exchange-energy approximation with correct asymptotic behavior," *Phys Rev A* **1988**, 38, 3098-3100. <http://dx.doi.org/10.1103/PhysRevA.38.3098>
- (115) C. Lee, W. Yang, and R. G. Parr "Development of the Colle-Salvetti correlation-energy formula into a functional of the electron density," *Physical Review B* **1988**, 37, 785-789. <http://dx.doi.org/10.1103/PhysRevB.37.785>
- (116) J. P. Perdew, A. Ruzsinszky, G. I. Csonka, O. A. Vydrov, G. E. Scuseria, L. A. Constantin, X. Zhou, and K. Burke "Restoring the Density-Gradient Expansion for Exchange in Solids and Surfaces," *Phys Rev Lett* **2008**, 100. <http://dx.doi.org/10.1103/PhysRevLett.100.136406>
- (117) L. Wang, T. Maxisch, and G. Ceder "Oxidation energies of transition metal oxides within the GGA+U framework," *Physical Review B* **2006**, 73. <http://dx.doi.org/10.1103/PhysRevB.73.195107>
- (118) V. I. Anisimov, J. Zaanen, and O. K. Andersen "Band theory and Mott insulators: Hubbard U instead of Stoner I," *Physical Review B* **1991**, 44, 943-954. <http://dx.doi.org/10.1103/PhysRevB.44.943>
- (119) S. Grimme, S. Ehrlich, and L. Goerigk "Effect of the Damping Function in Dispersion Corrected Density Functional Theory," *J Comput Chem* **2011**, 32, 1456-1465. <http://dx.doi.org/10.1002/jcc.21759>
- (120) S. Grimme, J. Antony, S. Ehrlich, and H. Krieg "A consistent and accurate ab initio parametrization of density functional dispersion correction (DFT-D) for the 94 elements H-Pu," *J Chem Phys* **2010**, 132, 154104. <http://dx.doi.org/10.1063/1.3382344>
- (121) T. A. Manz and N. G. Limas "Introducing DDEC6 atomic population analysis: part 1. Charge partitioning theory and methodology," *Rsc Adv* **2016**, 6, 47771-47801. <http://dx.doi.org/10.1039/c6ra04656h>
- (122) G. Henkelman, A. Arnaldsson, and H. Jonsson "A fast and robust algorithm for Bader decomposition of charge density," *Comp Mater Sci* **2006**, 36, 354-360. <http://dx.doi.org/10.1016/j.commatsci.2005.04.010>
- (123) F. L. Hirshfeld "Bonded-Atom Fragments for Describing Molecular Charge-Densities," *Theor Chim Acta* **1977**, 44, 129-138. <http://dx.doi.org/10.1007/Bf00549096>
- (124) R. S. Mulliken "Electronic Population Analysis on Lcao-Mo Molecular Wave Functions .1.," *J Chem Phys* **1955**, 23, 1833-1840. <http://dx.doi.org/10.1063/1.1740588>
- (125) P. Bultinck, C. Van Alsenoy, P. W. Ayers, and R. Carbo-Dorca "Critical analysis and extension of the Hirshfeld atoms in molecules," *J Chem Phys* **2007**, 126. <http://dx.doi.org/10.1063/1.2715563>

- (126) E. R. Davidson and S. Chakravorty "A Test of the Hirshfeld Definition of Atomic Charges and Moments," *Theor Chim Acta* **1992**, 83, 319-330. <http://dx.doi.org/10.1007/BF01113058>
- (127) A. E. Reed, R. B. Weinstock, and F. Weinhold "Natural-Population Analysis," *J Chem Phys* **1985**, 83, 735-746. <http://dx.doi.org/10.1063/1.449486>
- (128) J. A. Montgomery, M. J. Frisch, J. W. Ochterski, and G. A. Petersson "A complete basis set model chemistry. VII. Use of the minimum population localization method," *J Chem Phys* **2000**, 112, 6532-6542. <http://dx.doi.org/10.1063/1.481224>
- (129) S. Tazi, J. J. Molina, B. Rotenberg, P. Turq, R. Vuilleumier, and M. Salanne "A transferable ab initio based force field for aqueous ions," *J Chem Phys* **2012**, 136. <http://dx.doi.org/10.1063/1.3692965>
- (130) C. L. Olson, J. Nelson, M. Saiful Islam, and M. S. Islam "Defect chemistry, surface structures, and lithium insertion in anatase TiO₂," *The Journal of Physical Chemistry B* **2006**, 110, 9995-10001. <http://dx.doi.org/10.1021/jp0572611>
- (131) A. Pedone, G. Malavasi, M. C. Menziani, A. N. Cormack, and U. Segre "A new self-consistent empirical interatomic potential model for oxides, silicates, and silica-based glasses," *The Journal of Physical Chemistry B* **2006**, 110, 11780-11795. <http://dx.doi.org/10.1021/jp0611018>
- (132) J. E. Jones "On the determination of molecular fields.—I. From the variation of the viscosity of a gas with temperature," *Proceedings of the Royal Society of London. Series A, Containing Papers of a Mathematical and Physical Character* **1997**, 106, 441-462. <http://dx.doi.org/10.1098/rspa.1924.0081>
- (133) M. S. Daw and M. I. Baskes "Embedded-atom method: Derivation and application to impurities, surfaces, and other defects in metals," *Physical Review B* **1984**, 29, 6443-6453. <http://dx.doi.org/10.1103/PhysRevB.29.6443>
- (134) H. Rafii-Tabar and A. P. Sulton "Long-range Finnis-Sinclair potentials for f.c.c. metallic alloys," *Philosophical Magazine Letters* **2006**, 63, 217-224. <http://dx.doi.org/10.1080/09500839108205994>
- (135) J. Tersoff "New empirical approach for the structure and energy of covalent systems," *Physical Review B* **1988**, 37, 6991-7000. <http://dx.doi.org/10.1103/PhysRevB.37.6991>
- (136) F. H. Stillinger and T. A. Weber "Computer simulation of local order in condensed phases of silicon," *Physical Review B* **1985**, 31, 5262-5271. <http://dx.doi.org/10.1103/PhysRevB.31.5262>
- (137) A. C. T. van Duin, S. Dasgupta, F. Lorant, and W. A. Goddard "ReaxFF: A Reactive Force Field for Hydrocarbons," *The Journal of Physical Chemistry A* **2001**, 105, 9396-9409. <http://dx.doi.org/10.1021/jp004368u>

- (138) T.-R. Shan, B. D. Devine, J. M. Hawkins, A. Asthagiri, S. R. Phillpot, and S. B. Sinnott "Second-generation charge-optimized many-body potential for Si/SiO₂ and amorphous silica," *Physical Review B* **2010**, 82. <http://dx.doi.org/10.1103/PhysRevB.82.235302>
- (139) G. Lamoureux, A. D. MacKerell, and B. t. Roux "A simple polarizable model of water based on classical Drude oscillators," *The Journal of Chemical Physics* **2003**, 119, 5185-5197. <http://dx.doi.org/10.1063/1.1598191>
- (140) Y.-P. Liu, K. Kim, B. J. Berne, R. A. Friesner, and S. W. Rick "Constructing ab initio force fields for molecular dynamics simulations," *The Journal of Chemical Physics* **1998**, 108, 4739-4755. <http://dx.doi.org/10.1063/1.475886>
- (141) S. W. Rick, S. J. Stuart, and B. J. Berne "Dynamical fluctuating charge force fields: Application to liquid water," *The Journal of Chemical Physics* **1994**, 101, 6141-6156. <http://dx.doi.org/10.1063/1.468398>
- (142) J. Dai, Q. Chen, T. Glossmann, and W. Lai "Comparison of interatomic potential models on the molecular dynamics simulation of fast-ion conductors: A case study of a Li garnet oxide Li₇La₃Zr₂O₁₂," *Comp Mater Sci* **2019**, 162, 333-339. <http://dx.doi.org/10.1016/j.commatsci.2019.02.044>
- (143) R. A. Buckingham "The classical equation of state of gaseous helium, neon and argon," *Proc R Soc Lon Ser-A* **1938**, 168, 264-283. <http://dx.doi.org/10.1098/rspa.1938.0173>
- (144) P. M. Morse "Diatomic molecules according to the wave mechanics. II. Vibrational levels," *Physical Review* **1929**, 34, 57-64. <http://dx.doi.org/10.1103/Physrev.34.57>
- (145) J. Behler "Atom-centered symmetry functions for constructing high-dimensional neural network potentials," *The Journal of Chemical Physics* **2011**, 134, 074106. <http://dx.doi.org/10.1063/1.3553717>
- (146) A. P. Bartók, R. Kondor, and G. Csányi "On representing chemical environments," *Physical Review B* **2013**, 87. <http://dx.doi.org/10.1103/PhysRevB.87.184115>
- (147) M. Rupp, A. Tkatchenko, K.-R. Müller, and O. A. von Lilienfeld "Fast and Accurate Modeling of Molecular Atomization Energies with Machine Learning," *Phys Rev Lett* **2012**, 108. <http://dx.doi.org/10.1103/PhysRevLett.108.058301>
- (148) A. P. Bartók, M. C. Payne, R. Kondor, and G. Csányi "Gaussian Approximation Potentials: The Accuracy of Quantum Mechanics, without the Electrons," *Phys Rev Lett* **2010**, 104. <http://dx.doi.org/10.1103/PhysRevLett.104.136403>
- (149) J. Behler and M. Parrinello "Generalized Neural-Network Representation of High-Dimensional Potential-Energy Surfaces," *Phys Rev Lett* **2007**, 98. <http://dx.doi.org/10.1103/PhysRevLett.98.146401>
- (150) A. P. Thompson, L. P. Swiler, C. R. Trott, S. M. Foiles, and G. J. Tucker "Spectral neighbor analysis method for automated generation of quantum-accurate interatomic potentials,"

Journal of Computational Physics **2015**, 285, 316-330.
<http://dx.doi.org/10.1016/j.jcp.2014.12.018>

(151) A. V. Shapeev "Moment Tensor Potentials: A Class of Systematically Improvable Interatomic Potentials," *Multiscale Modeling & Simulation* **2016**, 14, 1153-1173.
<http://dx.doi.org/10.1137/15m1054183>

(152) H. J. C. Berendsen, J. P. M. Postma, W. F. van Gunsteren, A. DiNola, and J. R. Haak "Molecular dynamics with coupling to an external bath," *The Journal of Chemical Physics* **1984**, 81, 3684-3690. <http://dx.doi.org/10.1063/1.448118>

(153) H. C. Andersen "Molecular dynamics simulations at constant pressure and/or temperature," *The Journal of Chemical Physics* **1980**, 72, 2384-2393.
<http://dx.doi.org/10.1063/1.439486>

(154) S. Nosé "A unified formulation of the constant temperature molecular dynamics methods," *The Journal of Chemical Physics* **1984**, 81, 511-519.
<http://dx.doi.org/10.1063/1.447334>

(155) W. G. Hoover, A. J. C. Ladd, and B. Moran "High-Strain-Rate Plastic Flow Studied via Nonequilibrium Molecular Dynamics," *Phys Rev Lett* **1982**, 48, 1818-1820.
<http://dx.doi.org/10.1103/PhysRevLett.48.1818>

(156) M. Parrinello and A. Rahman "Polymorphic transitions in single crystals: A new molecular dynamics method," *J Appl Phys* **1981**, 52, 7182-7190.
<http://dx.doi.org/10.1063/1.328693>

(157) Y. Shin "Preparation and structural properties of layer-type oxides $\text{Na}_x\text{Ni}_{1-x}/2\text{Ti}_{1-x}/2\text{O}_2$ ($0.60 \leq x \leq 1.0$)," *Solid State Ionics* **2000**, 132, 131-141.
[http://dx.doi.org/10.1016/S0167-2738\(00\)00691-3](http://dx.doi.org/10.1016/S0167-2738(00)00691-3)

(158) H. M. Rietveld "A profile refinement method for nuclear and magnetic structures," *Journal of Applied Crystallography* **1969**, 2, 65-71.
<http://dx.doi.org/10.1107/s0021889869006558>

(159) R. Hempelmann *Quasielastic neutron scattering and solid state diffusion*; Oxford University Press: Oxford, 2000.

(160) M. J. Klenk, S. E. Boeberitz, J. Dai, N. H. Jalarvo, V. K. Peterson, and W. Lai "Lithium self-diffusion in a model lithium garnet oxide $\text{Li}_5\text{La}_3\text{Ta}_2\text{O}_{12}$: A combined quasi-elastic neutron scattering and molecular dynamics study," *Solid State Ionics* **2017**, 312, 1-7.
<http://dx.doi.org/10.1016/j.ssi.2017.09.022>

(161) J. R. Peet, C. A. Fuller, B. Frick, M. Zbiri, A. Piovano, M. R. Johnson, and I. R. Evans "Direct Observation of Oxide Ion Dynamics in $\text{La}_2\text{Mo}_2\text{O}_9$ on the Nanosecond Timescale," *Chemistry of Materials* **2017**, 29, 3020-3028. <http://dx.doi.org/10.1021/acs.chemmater.6b05507>

(162) C. T. Chudley and R. J. Elliott "Neutron Scattering from a Liquid on a Jump Diffusion Model," *P Phys Soc Lond* **1961**, 77, 353-&. <http://dx.doi.org/10.1088/0370-1328/77/2/319>

(163) K. S. Singwi and A. Sjölander "Diffusive Motions in Water and Cold Neutron Scattering," *Physical Review* **1960**, 119, 863-871. <http://dx.doi.org/10.1103/PhysRev.119.863>

(164) M. S. Islam "Ionic transport in ABO₃ perovskite oxides: a computer modelling tour," *Journal of Materials chemistry* **2000**, 10, 1027-1038. <http://dx.doi.org/10.1039/a908425h>

(165) M. S. Islam, D. J. Driscoll, C. A. J. Fisher, and P. R. Slater "Atomic-Scale Investigation of Defects, Dopants, and Lithium Transport in the LiFePO₄ Olivine-Type Battery Material," *Chemistry of Materials* **2005**, 17, 5085-5092. <http://dx.doi.org/10.1021/cm050999v>

(166) M. S. Islam and C. A. J. Fisher "Lithium and sodium battery cathode materials: computational insights into voltage, diffusion and nanostructural properties," *Chem. Soc. Rev.* **2014**, 43, 185-204. <http://dx.doi.org/10.1039/C3CS60199D>

(167) A. Chartier, C. Meis, W. J. Weber, and L. R. Corrales "Theoretical study of disorder in Ti-substituted La₂Zr₂O₇," *Physical Review B* **2002**, 65, 134116-134116. <http://dx.doi.org/10.1103/PhysRevB.65.134116>

(168) S. Lee and S. S. Park "Atomistic Simulation Study of Mixed-Metal Oxide (LiNi_{1/3}Co_{1/3}Mn_{1/3}O₂) Cathode Material for Lithium Ion Battery," *The Journal of Physical Chemistry C* **2012**, 116, 6484-6489. <http://dx.doi.org/10.1021/jp2122467>

(169) Y. Wang, A. Huq, and W. Lai "Insight into lithium distribution in lithium-stuffed garnet oxides through neutron diffraction and atomistic simulation: Li_{7-x}La₃Zr_{2-x}Ta_xO₁₂ (x=0–2) series," *Solid State Ionics* **2014**, 255, 39-49. <http://dx.doi.org/10.1016/j.ssi.2013.11.017>

(170) V. Petříček, M. Dušek, and L. Palatinus In *Zeitschrift für Kristallographie - Crystalline Materials* 2014; Vol. 229, p 345.

(171) T. Shimono, D. Tanabe, W. Kobayashi, and Y. Moritomo "Structural response of P2-Type Na_xMnO₂ against Na⁺ intercalation," *Journal of the Physical Society of Japan* **2013**, 82, 083601-083601. <http://dx.doi.org/10.7566/JPSJ.82.083601>

(172) D. Tanabe, T. Shimono, W. Kobayashi, and Y. Moritomo "Temperature dependence of anisotropic displacement parameters in O₃-type NaMO₂ (M = Cr and Fe): Comparison with isostructural LiCoO₂," *Physica Status Solidi - Rapid Research Letters* **2014**, 8, 287-290. <http://dx.doi.org/10.1002/pssr.201308295>

(173) J. D. Gale and A. L. Rohl "The general utility lattice program (GULP)," *Molecular Simulation* **2003**, 29, 291-341. <http://dx.doi.org/10.1080/0892702031000104887>

(174) B. G. Dick Jr, A. W. Overhauser, B. G. Dick, and A. W. Overhauser "Theory of the dielectric constants of alkali halide crystals," *Physical Review* **1958**, 112, 90-90. <http://dx.doi.org/10.1103/PhysRev.112.90>

(175) K. Momma and F. Izumi "VESTA 3 for three-dimensional visualization of crystal, volumetric and morphology data," *Journal of Applied Crystallography* **2011**, *44*, 1272-1276. <http://dx.doi.org/10.1107/S0021889811038970>

(176) Z. Lu and J. R. Dahn "In situ X-ray diffraction study of P2-Na-2/3[Ni1/3Mn2/3]O-2," *Journal of the Electrochemical Society* **2001**, *148*, A1225-A1229. <http://dx.doi.org/10.1149/1.1407247>

(177) Y. H. Jung, A. S. Christiansen, R. E. Johnsen, P. Norby, and D. K. Kim "In Situ X-Ray Diffraction Studies on Structural Changes of a P2 Layered Material during Electrochemical Desodiation/Sodiation," *Advanced Functional Materials* **2015**, *25*, 3227-3237. <http://dx.doi.org/10.1002/adfm.201500469>

(178) R. Shanmugam, Q. Chen, and W. Lai "Structural study of Na-2/3[Ni1/3Ti2/3]O-2 using neutron diffraction and atomistic simulations," *Solid State Ionics* **2018**, *314*, 17-24. <http://dx.doi.org/10.1016/j.ssi.2017.11.007>

(179) G. Kresse and J. Furthmuller "Efficient iterative schemes for ab initio total-energy calculations using a plane-wave basis set," *Physical Review B* **1996**, *54*, 11169-11186. <http://dx.doi.org/10.1103/PhysRevB.54.11169>

(180) P. E. Blochl "Projector Augmented-Wave Method," *Physical Review B* **1994**, *50*, 17953-17979. <http://dx.doi.org/10.1103/PhysRevB.50.17953>

(181) S. L. Dudarev, G. A. Botton, S. Y. Savrasov, C. J. Humphreys, and A. P. Sutton "Electron-energy-loss spectra and the structural stability of nickel oxide: An LSDA+U study," *Physical Review B* **1998**, *57*, 1505-1509. <http://dx.doi.org/10.1103/PhysRevB.57.1505>

(182) R. Fielden and M. N. Obrovac "Low Voltage Sodium Intercalation in $\text{Na}_x\text{Ni}_x/2\text{Ti}_{1-x}/2\text{O}_2$ ($0.5 \leq x \leq 1.0$)," *Journal of The Electrochemical Society* **2014**, *161*, A1158-A1163. <http://dx.doi.org/10.1149/2.118406jes>

(183) I. Nakai, K. Takahashi, Y. Shiraishi, T. Nakagome, and F. Nishikawa "Study of the Jahn-Teller distortion in LiNiO₂, a cathode material in a rechargeable lithium battery, by in situ X-ray absorption fine structure analysis," *J Solid State Chem* **1998**, *140*, 145-148. <http://dx.doi.org/10.1006/jssc.1998.7943>

(184) D. H. Lee, J. Xu, and Y. S. Meng "An advanced cathode for Na-ion batteries with high rate and excellent structural stability," *Physical Chemistry Chemical Physics* **2013**, *15*, 3304-3312. <http://dx.doi.org/10.1039/C2CP44467D>

(185) J. H. Cheng, C. J. Pan, J. F. Lee, J. M. Chen, M. Guignard, C. Delmas, D. Carlier, and B. J. Hwang "Simultaneous Reduction of Co³⁺ and Mn⁴⁺ in P2-Na_{2/3}Co_{2/3}Mn_{1/3}O₂ As Evidenced by X-ray Absorption Spectroscopy during Electrochemical Sodium Intercalation," *Chemistry of Materials* **2014**, *26*, 1219-1225. <http://dx.doi.org/10.1021/cm403597h>

(186) D. A. Greenwood "The Boltzmann Equation in the Theory of Electrical Conduction in Metals," *Proceedings of the Physical Society* **1958**, *71*, 585-596. <http://dx.doi.org/10.1088/0370-1328/71/4/306>

(187) R. Kubo "Statistical-Mechanical Theory of Irreversible Processes .1. General Theory and Simple Applications to Magnetic and Conduction Problems," *Journal of the Physical Society of Japan* **1957**, *12*, 570-586. <http://dx.doi.org/10.1143/Jpsj.12.570>

(188) E. Mamontov and K. W. Herwig "A time-of-flight backscattering spectrometer at the Spallation Neutron Source, BASIS," *Rev Sci Instrum* **2011**, *82*. <http://dx.doi.org/10.1063/1.3626214>

(189) O. Arnold, J. C. Bilheux, J. M. Borreguero, A. Buts, S. I. Campbell, L. Chapon, M. Doucet, N. Draper, R. Ferraz Leal, M. A. Gigg, V. E. Lynch, A. Markvardsen, D. J. Mikkelson, R. L. Mikkelson, R. Miller, K. Palmen, P. Parker, G. Passos, T. G. Perring, P. F. Peterson, S. Ren, M. A. Reuter, A. T. Savici, J. W. Taylor, R. J. Taylor, R. Tolchenov, W. Zhou, and J. Zikovsky "Mantid-Data analysis and visualization package for neutron scattering and mu SR experiments," *Nucl Instrum Meth A* **2014**, *764*, 156-166. <http://dx.doi.org/10.1016/j.nima.2014.07.029>

(190) R. T. Azuah, L. R. Kneller, Y. M. Qiu, P. L. W. Tregenna-Piggott, C. M. Brown, J. R. D. Copley, and R. M. Dimeo "DAVE: A Comprehensive Software Suite for the Reduction, Visualization, and Analysis of Low Energy Neutron Spectroscopic Data," *J Res Natl Inst Stand Technol* **2009**, *114*, 341-358. <http://dx.doi.org/10.6028/jres.114.025>

(191) T. J. Willis, D. G. Porter, D. J. Voneshen, S. Uthayakumar, F. Demmel, M. J. Gutmann, M. Roger, K. Refson, and J. P. Goff "Diffusion mechanism in the sodium-ion battery material sodium cobaltate," *Sci Rep* **2018**, *8*, 3210. <http://dx.doi.org/10.1038/s41598-018-21354-5>

(192) P. F. Wang, H. R. Yao, X. Y. Liu, Y. X. Yin, J. N. Zhang, Y. R. Wen, X. Q. Yu, L. Gu, and Y. G. Guo "Na⁺/vacancy disordering promises high-rate Na-ion batteries," *Sci Adv* **2018**, *4*. <http://dx.doi.org/10.1126/sciadv.aar6018>

(193) C. Zhao, Z. Yao, Q. Wang, H. Li, J. Wang, M. Liu, S. Ganapathy, Y. Lu, J. Cabana, B. Li, X. Bai, A. Aspuru-Guzik, M. Wagemaker, L. Chen, and Y.-S. Hu "Revealing High Na-Content P2-Type Layered Oxides as Advanced Sodium-Ion Cathodes," *J Am Chem Soc* **2020**, *142*, 5742-5750. <http://dx.doi.org/10.1021/jacs.9b13572>

(194) M. Salanne and P. A. Madden "Polarization effects in ionic solids and melts," *Mol Phys* **2011**, *109*, 2299-2315. <http://dx.doi.org/10.1080/00268976.2011.617523>

(195) T. A. Manz and D. S. Sholl "Improved Atoms-in-Molecule Charge Partitioning Functional for Simultaneously Reproducing the Electrostatic Potential and Chemical States in Periodic and Nonperiodic Materials," *J Chem Theory Comput* **2012**, *8*, 2844-2867. <http://dx.doi.org/10.1021/ct3002199>

- (196) K. T. Tang and J. P. Toennies "An improved simple model for the van der Waals potential based on universal damping functions for the dispersion coefficients," *The Journal of Chemical Physics* **1984**, *80*, 3726-3741. <http://dx.doi.org/10.1063/1.447150>
- (197) J. Hutter, M. Iannuzzi, F. Schiffmann, and J. VandeVondele "CP2K: atomistic simulations of condensed matter systems," *Wires Comput Mol Sci* **2014**, *4*, 15-25. <http://dx.doi.org/10.1002/wcms.1159>
- (198) J.-P. Hansen and I. R. McDonald *Theory of simple liquids: with applications to soft matter*; Academic Press, 2013.
- (199) G. Williams and D. C. Watts "Non-Symmetrical Dielectric Relaxation Behaviour Arising from a Simple Empirical Decay Function," *T Faraday Soc* **1970**, *66*, 80-+. <http://dx.doi.org/10.1039/TF9706600080>
- (200) O. A. Smirnova, R. O. Fuentes, F. Figueiredo, V. V. Kharton, and F. M. B. Marques "Stability and thermal expansion of Na⁺-conducting ceramics," *J Electroceram* **2003**, *11*, 179-189. <http://dx.doi.org/10.1023/B:Jecr.0000026373.56703.B0>
- (201) N. Bucher, S. Hartung, J. B. Franklin, A. M. Wise, L. Y. Lim, H.-Y. Chen, J. N. Weker, M. F. Toney, and M. Srinivasan "P₂-Na_xCoyMn_{1-y}O₂ (y = 0, 0.1) as Cathode Materials in Sodium-Ion Batteries—Effects of Doping and Morphology To Enhance Cycling Stability," *Chemistry of Materials* **2016**, *28*, 2041-2051. <http://dx.doi.org/10.1021/acs.chemmater.5b04557>
- (202) Q. Chen and W. Lai "A Computational Study on P₂-Type Na_x[Ni_{1/3}Ti_{2/3}]O₂ as Bi-Functional Electrode Material for Na-Ion Batteries," *Journal of The Electrochemical Society* **2018**, *165*, A3586-A3594. <http://dx.doi.org/10.1149/2.1281814jes>
- (203) S. Guo, H. Yu, P. Liu, Y. Ren, T. Zhang, M. Chen, M. Ishida, and H. Zhou "High-performance symmetric sodium-ion batteries using a new, bipolar O₃-type material, Na_{0.8}Ni_{0.4}Ti_{0.6}O₂," *Energy Environ. Sci.* **2015**, *8*, 1237-1244. <http://dx.doi.org/10.1039/C4EE03361B>
- (204) J. Behler "Perspective: Machine learning potentials for atomistic simulations," *The Journal of Chemical Physics* **2016**, *145*, 170901. <http://dx.doi.org/10.1063/1.4966192>
- (205) V. L. Deringer, M. A. Caro, and G. Csányi "Machine Learning Interatomic Potentials as Emerging Tools for Materials Science," *Advanced Materials* **2019**, *31*, 1902765. <http://dx.doi.org/10.1002/adma.201902765>
- (206) S. Manzhos, X. Wang, R. Dawes, and T. Carrington "A Nested Molecule-Independent Neural Network Approach for High-Quality Potential Fits[†]," *The Journal of Physical Chemistry A* **2006**, *110*, 5295-5304. <http://dx.doi.org/10.1021/jp055253z>
- (207) W. Li, Y. Ando, E. Minamitani, and S. Watanabe "Study of Li atom diffusion in amorphous Li₃PO₄ with neural network potential," *The Journal of Chemical Physics* **2017**, *147*, 214106. <http://dx.doi.org/10.1063/1.4997242>

- (208) N. Artrith and A. Urban "An implementation of artificial neural-network potentials for atomistic materials simulations: Performance for TiO₂," *Comp Mater Sci* **2016**, *114*, 135-150. <http://dx.doi.org/10.1016/j.commatsci.2015.11.047>
- (209) K. Lee, D. Yoo, W. Jeong, and S. Han "SIMPLE-NN: An efficient package for training and executing neural-network interatomic potentials," *Comput Phys Commun* **2019**, *242*, 95-103. <http://dx.doi.org/10.1016/j.cpc.2019.04.014>
- (210) W. Jeong, K. Lee, D. Yoo, D. Lee, and S. Han "Toward Reliable and Transferable Machine Learning Potentials: Uniform Training by Overcoming Sampling Bias," *The Journal of Physical Chemistry C* **2018**, *122*, 22790-22795. <http://dx.doi.org/10.1021/acs.jpcc.8b08063>
- (211) D. P. Kingma and J. Ba "Adam: A method for stochastic optimization," *arXiv preprint arXiv:1412.6980* **2014**.
- (212) S. Plimpton "Fast Parallel Algorithms for Short-Range Molecular Dynamics," *Journal of Computational Physics* **1995**, *117*, 1-19. <http://dx.doi.org/10.1006/jcph.1995.1039>
- (213) S.-M. Oh, S.-T. Myung, J.-Y. Hwang, B. Scrosati, K. Amine, and Y.-K. Sun "High Capacity O₃-Type Na[Li_{0.05}(Ni_{0.25}Fe_{0.25}Mn_{0.5})_{0.95}]O₂ Cathode for Sodium Ion Batteries," *Chemistry of Materials* **2014**, *26*, 6165-6171. <http://dx.doi.org/10.1021/cm502481b>
- (214) K. Kubota, Y. Yoda, and S. Komaba "Origin of Enhanced Capacity Retention of P2-Type Na_{2/3}Ni_{1/3-x}Mn_{2/3}Cu_xO₂ for Na-Ion Batteries," *Journal of The Electrochemical Society* **2017**, *164*, A2368-A2373. <http://dx.doi.org/10.1149/2.0311712jes>
- (215) L. Dahéron, R. Dedryvère, H. Martinez, D. Flahaut, M. Ménétrier, C. Delmas, and D. Gonbeau "Possible Explanation for the Efficiency of Al-Based Coatings on LiCoO₂: Surface Properties of LiCo_{1-x}Al_xO₂ Solid Solution," *Chemistry of Materials* **2009**, *21*, 5607-5616. <http://dx.doi.org/10.1021/cm901972e>